

UNIVERSITÀ DEGLI STUDI DI PADOVA

SCUOLA DI SCIENZE

Dipartimento di Geoscienze

TESI DI LAUREA MAGISTRALE IN

GEOLOGIA AMBIENTALE E DINAMICA DELLA TERRA

CURRICULUM EARTH DYNAMICS

**SEISMIC CYCLE AND DEFORMATION
PROCESSES IN QUARTZ GOUGES UNDER
HYDROTHERMAL CONDITIONS**

Relatore: Prof. Telemaco Tesei

Correlatore: Prof. Giulio Di Toro

Laureando: Giovanni Guglielmi

ANNO ACCADEMICO 2022/2023

ABSTRACT

Frictional experiments play a key role in understanding earthquakes geology, the mechanics of faulting and more in general rocks physics. The heterogeneous, non-periodic, large-scale and unpredictable nature of the seismic cycle makes its faithful reproduction in the laboratory complicated, although scientific and technological developments over the years have increasingly brought its experimental simulation closer to its observation in nature, from a phenomenological point of view.

In the brittle domain of the Earth's Upper Crust, earthquakes tend to occur between 5 and 15 km depth and at temperatures ranging from ambient to approximately 400 °C. The quartz, one of the main constituents of the Continental Crust, is a material whose mechanical and chemical properties have been widely investigated over time. Despite that, by reviewing the literature it is noticeable a lack of systematic frictional experiments under hydrothermal conditions, i.e. in the presence of hot and pressurized water (a likely condition for seismogenic faults).

The present thesis is aiming to investigate the mechanical behavior of a quartz gouge under hydrothermal conditions during the seismic cycle, analyzing the different trends of friction (shear strength) and compaction under different pressure and temperature conditions. In particular, a considerable attention has been reserved to the *healing*: the mechanism by which a fault gains shear strength during stationary (or quasi-stationary) contact, i.e. the interseismic period. The healing is directly connected to the recurrence of earthquakes in nature, because it controls the elastic strain energy that faults store during quiescence periods, subsequently released during the seismic event.

The low -to high- velocity friction apparatus "RoSA" (Rotary-Shear Apparatus), equipped with the pressure vessel "HYDROS", installed in the Rock Mechanics Laboratory of the Department of Geosciences in the University of Padova, was used to investigate some fundamental properties of the seismic cycle of quartz, and the deformation processes related. I performed 10 frictional experiments under hydrothermal conditions, varying temperature (from 23 °C to 400 °C), effective normal stress (10 MPa and 20 MPa), pore fluid pressure (6 MPa and 36 MPa), and grain size (angular quartz, < 110 μm; microquartz, < 5 μm). During the experiments I performed "Slide-Hold-Slide" (SHS) tests. In SHS tests, sliding phases (slide) are alternated with increasing stationary contact periods (hold). The hold times for each experiment vary from 10 to 10000-50000 s. This procedure is used to simulate the seismic cycle with slip and interseismic periods. Upon reshear, I measured the restrengthening (healing) that the fault experienced during the previous hold.

The analysis of experimental data shows that:

- The dynamic friction measured during the steady state (μ_{ss}) does not show remarkably relationships with the temperature. On the other hand, it seems to increase as the grain size decreases, pointing out a greater difficulty in grinding and comminuting the grains by the experimental fault.

- Both the magnitude ($\Delta\mu$) and the rate (β) of healing increase as the temperature increases. In particular, the healing rate at 400 °C exhibits a quadratic dependence on the logarithm of hold time, while the data suggest a linear dependence between the two parameters below this temperature threshold. The same behavior is observed for the friction drop ($\Delta\mu_{drop}$) that is recorded after a hold-slide event. These phenomena, after being compared with compaction trends and similar experiments carried out by several researchers, are attributed to the pressure solution mechanism.
- Different grain sizes do not seem to systematically affect healing measurements.
- In experiments where two SHS tests were performed, the healing of fault gouges is much lower at high strains, compared to lower strains.
- The analysis of the SHS events, compared to those of several papers, suggests that the healing of quartz observed is increasingly "*non-Dieterich-type*", particularly at high temperature (400°C). This validates the hypothesis that deformation of quartz, when assisted by hot and pressurized water, is affected by different deformation mechanisms compared to those relating to a "*dry*" deformation.

RIASSUNTO

Gli esperimenti di attrito hanno un ruolo chiave nella comprensione della geologia dei terremoti, della meccanica delle faglie ed in generale della fisica delle rocce. La natura eterogenea, non periodica, a larga scala e poco prevedibile del ciclo sismico rende complicata la sua fedele riproduzione in laboratorio, sebbene gli sviluppi scientifici e tecnologici nel corso degli anni abbiano sempre più avvicinato la sua simulazione sperimentale alla sua osservazione in natura, dal punto di vista fenomenologico.

Nel regime fragile della Crosta Superiore della Terra, i terremoti di solito avvengono tra 5 e 15 km di profondità ed a temperature che vanno da quelle ambientali a circa 400 °C. Il quarzo, uno dei principali costituenti della Crosta Continentale, è un materiale le cui proprietà meccaniche e chimiche sono state ampiamente indagate. Nonostante ciò, revisionando la letteratura si nota una mancanza di esperimenti sistematici in condizioni idrotermali, ossia in presenza di acqua calda e pressurizzata (comune condizione in cui si trovano le faglie sismogeniche).

L'obiettivo principale di questa tesi è quello di studiare il comportamento meccanico di un gouge di quarzo in condizioni idrotermali durante il ciclo sismico, analizzando i diversi trend di attrito e compattazione, al variare delle condizioni di pressione, temperatura e granulometria. In particolare, un dettaglio a cui ho dedicato notevole attenzione è l'*healing*, il meccanismo per cui una faglia guadagna resistenza durante i periodi di contatto stazionario (o quasi-stazionario). L'*healing* è il processo che controlla l'accumulo di energia di deformazione elastica lungo le faglie durante i periodi di quiescenza, poi successivamente rilasciata con l'evento sismico.

L'apparato sperimentale "RoSA" (Rotary-Shear Apparatus), equipaggiato con il pressure vessel "HYDROS", installato nel Laboratorio di Meccanica delle Rocce del Dipartimento di Geoscienze dell'Università di Padova, mi ha permesso di indagare alcune caratteristiche fondamentali dell'attrito idrotermale nel quarzo e dei processi deformativi ad esso associati. Ho condotto 10 esperimenti di attrito in condizioni idrotermali, variando la temperatura (da 23 °C a 400 °C), lo stress normale effettivo (da 10 MPa a 20 MPa), la pressione dei fluidi (da 6 MPa a 36 MPa) e la granulometria (quarzo angolare, < 110 µm; microquarzo, < 5 µm). Gli esperimenti sono stati condotti secondo una particolare tecnica sperimentale, chiamata Slide-Hold-Slide (SHS), fondamentale per la simulazione del ciclo sismico e valutare le caratteristiche dell'*healing*. In questa procedura, le fasi di scivolamento relativo delle due superfici di faglia (slide) sono alternate a crescenti periodi di contatto stazionario (hold). I tempi di hold, per ogni esperimento, variano da 10 a 10000-50000 s.

L'analisi dei dati sperimentali mostra che:

- L'attrito dinamico misurato durante lo stato stazionario (μ_{ss}) non evidenzia particolari relazioni con la temperatura. Al contrario, sembra aumentare al diminuire della granulometria, indice di una maggiore difficoltà nella macinazione dei grani da parte della faglia sperimentale.

- Sia la magnitudo ($\Delta\mu$) che la velocità (β) dell'healing aumentano all'aumentare della temperatura. In particolare, la velocità dell'healing a 400 °C esibisce una dipendenza quadratica dal logaritmo del tempo di hold, mentre al di sotto di questa soglia i dati suggeriscono una dipendenza lineare ("*Dieterich-type*"). Lo stesso comportamento si osserva per il drop di attrito ($\Delta\mu_{drop}$) che si registra dopo un evento hold-slide. Questi fenomeni, dopo esser stati comparati con esperimenti analoghi effettuati da diversi ricercatori, sono stati attribuiti al meccanismo di presso-soluzione (pressure solution).
- La differente granulometria non sembra interessare in modo sistematico le misure di healing.
- Negli esperimenti in cui sono stati eseguiti due test SHS, l'healing del gouge di faglia è sensibilmente minori ad alti strain, rispetto a quello misurato a bassi strain.
- L'analisi degli eventi SHS, comparata a quella di altri studi, ha permesso di stabilire che l'healing osservato diventa progressivamente "*non-Dieterich-type*", in particolare ad alte temperature. Questo valida l'ipotesi che la deformazione del quarzo, quando assistita da acqua calda e pressurizzata, è interessata da meccanismi deformativi differenti rispetto a quelli relativi ad una deformazione in assenza di fluidi.

INDEX OF CONTENTS

1 Introduction	9
1.1 Brittle failure.....	11
1.2 The seismic cycle.....	15
2 Methods	23
2.1 Description of the experimental apparatus	23
2.2 Experimental strategy and procedure.....	27
2.3 Data cleaning and analysis.....	32
3 Results	35
3.1 Mechanical data	35
3.2 Description of mechanical data.....	46
3.3 Mechanical comparison between experiments	51
3.3.1 The effect of temperature	51
3.3.2 The effect of grain size.....	56
3.3.3 The effect of shear strain on healing	64
4 Discussion.....	70
4.1 The role of fluid	71
4.1.1 Solubility of quartz.....	71
4.1.2 Mechanical role of fluid	73
4.1.3 Pressure solution mechanism	73
4.2 Slip hardening and friction	74
4.3 The role of temperature.....	76
4.3.1 Temperature effect during first stages of slip.....	76
4.3.2 Temperature effect on healing.....	78
4.4 The role of grain size	85
4.5 The role of shear strain on healing.....	88
4.6 Comparison with previous studies	90
4.7 SHS anatomy	94
4.8 Implications for crustal faults	98

Conclusions	101
References	104

Chapter 1

Introduction

The investigation of mechanical properties of rocks has always been a relevant research field in geology. The reason is that it represents a necessary key to understand the processes of rock deformation, including natural -and human induced- earthquakes. Other applications deal with engineering, architecture, mining, oil and gas industry and CO₂ storage.

Experimental laboratory rock mechanics studies started in the nineteenth century, with tensile and compressive tests on various types of rocks and evolved until now through technological developments of experimental apparatuses and techniques (*Paterson & Wong, 2005*). Nowadays, one of the most challenging applications of this topic regards earthquake and fault mechanics: several types of machineries and experimental strategies have been developed over the years, contributing to broaden the data acquisition on mechanic/elastic properties of rocks and to understand the physical laws governing processes occurring during the seismic cycle. The possibility of investigating rock deformation at the micro-nano -scale leads to the comprehension of processes at the meter -kilometer- scale, i.e., from laboratory controlled to natural destructive earthquakes. The upscaling problem has always been one of the hardest to overcome, since the quite simple laboratory systems are not completely representative of the huge heterogeneity of natural systems in the Earth's Crust (by a chemical, physical, mineralogical and geological perspective).

Deformation of rocks can be roughly distinguished into two types: brittle and ductile. The main difference between the two is the mode by which the system accommodates stresses. In a brittle environment fractures (micro -to macro- cracks) dominate, localizing and concentrating deformation and stresses within few millimeters - often micrometers- thick slip zones (Lockner *et al.*, 1992; Sibson, 2003). In a ductile environment, materials use to flow within a wider shear zone, generally at lower strain rates (Sibson, 1977; Fagereng & Sibson, 2010). Brittleness and ductility are not material properties, the same rock can behave in both ways depending on the pressure and temperature (P-T), strain rate and fluid pressure/chemistry conditions under which it deforms.

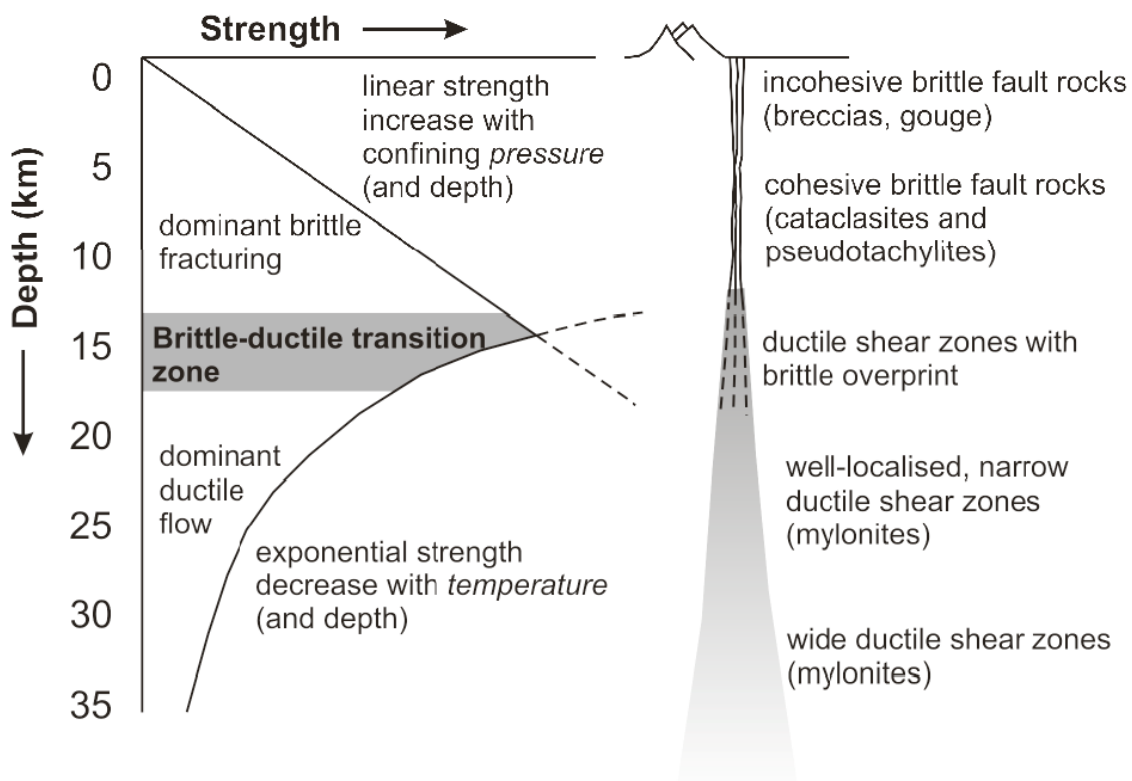


Figure 1.1. Brittle and ductile domains, with brittle-ductile transition highlighted. On the right, geological framework exhibits different fault zones. The schematic model of crustal-scale fault zones was originally proposed by Sibson (1977), while the subdivision of brittle and ductile regimes as function of depth was introduced by Scholz (1988). Diagram from Grigull (2011).

The brittle-ductile transition in the Continental Crust usually assumed to occur at depth between 10-20 km (Sibson, 1977) (Figure 1.1). At these conditions elasto-frictional and visco-plastic behaviors are energetically roughly equivalent, and different deformation processes activate (e.g. diffusion creep, diffusive mass transfer, dislocation creep, crystal plasticity) (Scholz, 1988). Temperatures between 300 °C and 600 °C (for a typical

geothermal gradient of 25-30 °C/km) likely induce plastic deformation of quartz and feldspar, the main constituents of the Continental Crust (*Brace and Kohlstedt, 1980*).

In the present thesis I investigated the deformation of quartz at temperatures ranging from the purely brittle domain to the brittle-ductile transition (i.e., up to 400 °C). Quartz is a key constituent of the upper and seismogenic part of the Crust, and I studied its role in controlling fault strength and strength recovery during the seismic cycle by performing frictional experiments. In the following, I summarize the main concepts of brittle deformation phenomenology and deformation processes that will be used in the rest of this thesis to interpret the results of the experiments.

1.1 Brittle failure

Brittle failure is defined as the pressure-dependent failure of rocks; it produces fractures that may be described as localized and discrete discontinuities within the uppermost part of the Crust (*Fagereng & Sibson, 2010*). When a rock is stressed, it stores elastic strain energy, deforming elastically until the achievement of a critical stress level (yield point, C in Figure 1.2). In the elastic regime, the linear dependence between stress and strain is described by the Young's modulus (E in Figure 1.2). Below the yield point, the rock can return to its original shape, recovering the elastic deformation that occurred. Beyond the yield point, the material starts to deform plastically (stress and strain are no more in direct proportionality), and deformation becomes permanent, until the final failure of the rock.

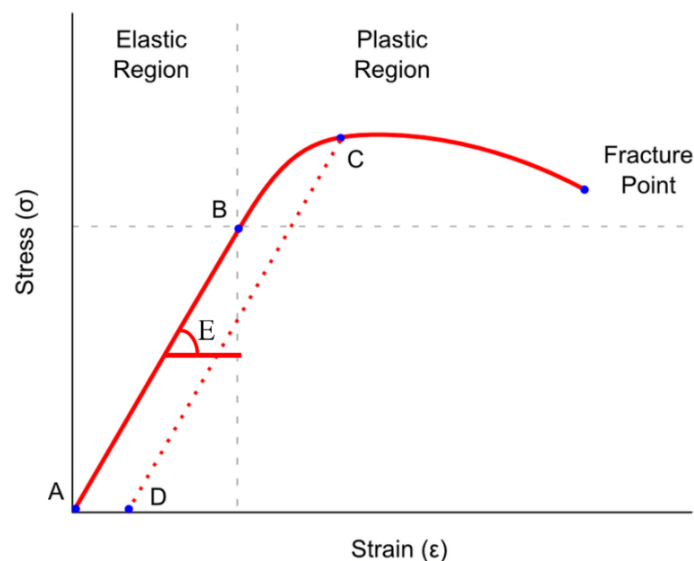


Figure 1.2. Brittle and plastic regimes.

In a rock-fluid system, it is possible to compute the effective stress acting on a surface, using the *Terzaghi's principle (1922,1925)*:

$$\sigma' = \sigma - P_p \quad (1.1)$$

Where σ' (Pa) is the effective stress, σ (Pa) is the total stress and P_p (Pa) is the pore fluid pressure.

Amontons law (1699) defines the shear stress acting on the apparent contact area between two stressed surfaces is defined as:

$$\tau = \mu \cdot \sigma_n \quad (1.2)$$

Where τ (Pa) is the shear stress, μ is the static friction coefficient and σ_n (Pa) is the applied normal stress. From this, it is possible to describe the shear strength of a rock under compression with a failure envelope (*Mohr-Coulomb* criterium) in the Mohr space:

$$\tau = C_0 + \mu \cdot (\sigma_n - P_p) = C_0 + \mu \cdot \sigma_n' \quad (1.3)$$

Where τ (Pa) is the shear stress, C_0 (Pa) is the internal cohesion of the material, μ is the static friction coefficient, σ_n (Pa) is the normal stress, P_p (Pa) is the pore fluid pressure and σ_n' is the effective normal stress (Pa).

Subsequently, *Murrel-Griffith* parabolic criterium was added to the failure envelope, to describe how a material behaves while undergoing tensile stresses. *Murrel-Griffith* parabolic criterium is defined as:

$$\tau^2 - 4T_0 \cdot \sigma_n - 4T_0^2 = 0 \quad (1.4)$$

Where τ (Pa) is the shear stress, T_0 (Pa) represents the tensile strength of the material and σ_n (Pa) is the applied normal stress. The relationship between T_0 and C_0 is defined as:

$$C_0 = 2T_0 \quad (1.5)$$

In addition, describing the stresses that produced a fracture with a certain angle in the Mohr space, it is possible to get the orientation and the magnitude of principal stresses (Figure 1.3). However, Amontons law and Mohr-Coulomb criterium describe only the large-scale strength of rocks (and more in general materials).

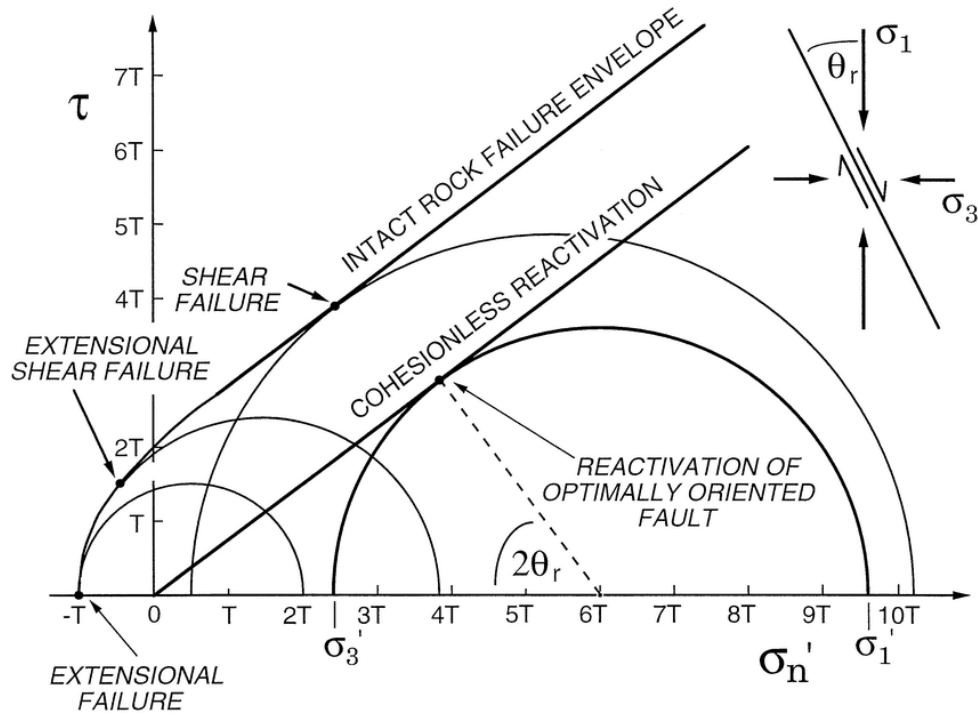


Figure 1.3. Mohr-Coulomb and Murrell-Griffith criteria describe the failure envelope in the Mohr space. Angle 2θ on the Mohr space corresponds to angle θ in the real space. From Sibson & Scott (1998).

Byerlee (1978) collected the shear strength of a multitude of different rocks under crustal normal stress conditions (Figure 1.4), finding out that for $\sigma_n < 200$ MPa the shear stress increased approximately linearly with the normal stress (consistently with the Amontons law and Coulomb's criterion) and is relatively independent on the rock type and on the roughness of the surfaces:

$$\tau = 0.85 \cdot \sigma_n \tag{1.6}$$

While over $\sigma_n > 200$ MPa, the law changed as:

$$\tau = 0.5 + 0.6 \cdot \sigma_n \tag{1.7}$$

These data are consistent with the increase of stress with depth measured in deep drilling experiments of the Crust, as reported by Townend and Zoback (2000, and references therein). Also it is consistent with typical Andersonian normal faults, which dip around 30° from σ_1 orientation, implying a τ/σ_n ratio of 0.6-0.85.

MAXIMUM FRICTION

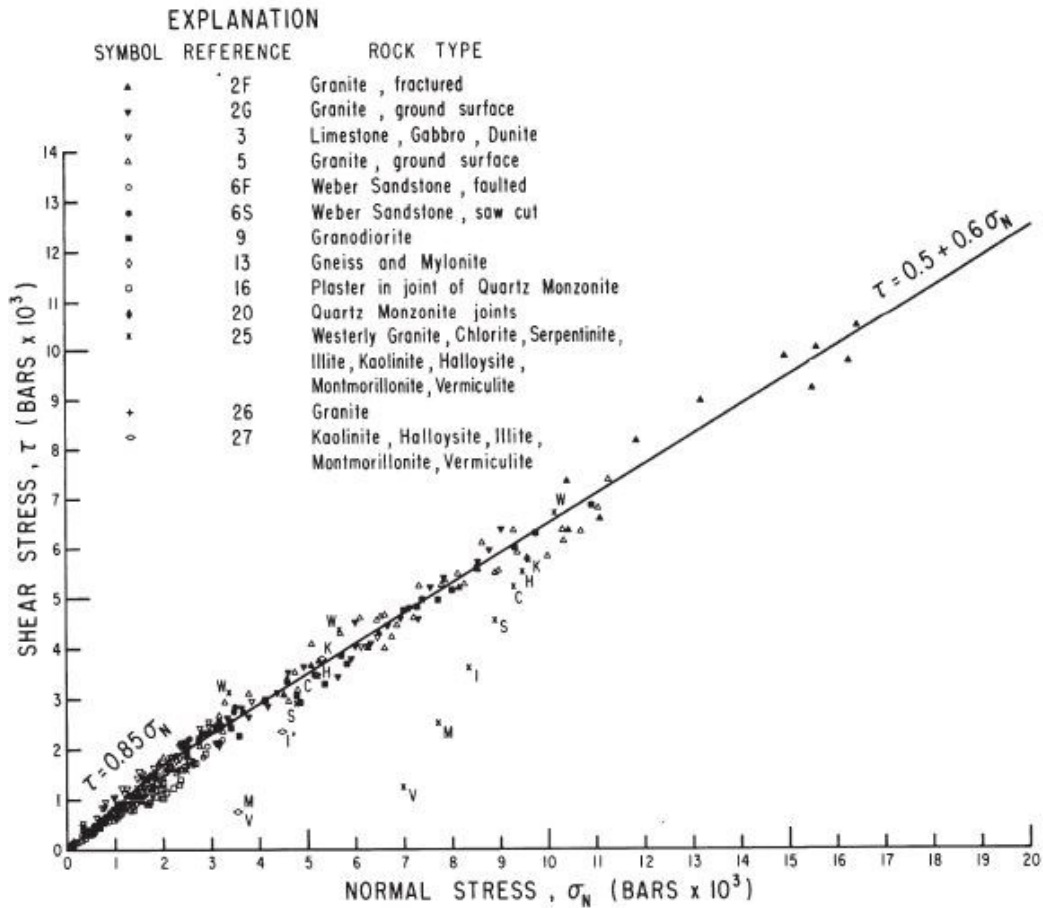


Figure 1.4. The average internal friction (expressed as the slope of the best fit line) is $\mu \sim 0.6-0.85$ for many rock types over crustal stress conditions. From Byerlee (1978).

Although Byerlee's laws remain an important reference for rock friction and behavior, there are relevant exceptions to that. The most prominent one deals with clays and clay-rich rocks: a content in phyllosilicates higher than 25-30% shows very low shear strength, ranging from $\mu = \sim 0.15$ to $\mu = \sim 0.5$ (Moore & Lockner, 2004; Ikari et al., 2009, Tesei et al., 2012). This indicates that shear strength of rocks is dependent on mineralogical assemblage, that is relevant in many major faults in which fluid-rock alteration driven by deformation can be intense (Collettini et al., 2019).

Also, even though bulk friction is relatively constant at the first order of magnitude, the stability of fault slip (i.e. creep or seismic behavior) may depend on minor variations of friction and/or on a multitude of geological factors (see below).

1.2 The seismic cycle

Tectonic faults in the upper Crust are sub-planar heterogeneous surfaces where deformation spanning from the kilometer down to the nanoscale accumulates throughout the entire fault history (*Tesei et al., 2014*). Earthquakes occur along tectonic faults by stick-slip motion (*Brace & Byerlee, 1966*), because friction of faults is often unstable, and slip occurs rapidly as a rupture dynamically propagates over the fault surface (*Scholz, 2019*). Crustal earthquakes concentrate at plate boundaries and sporadically within continental intraplate regions, which may possess several structures inherited from former tectonic episodes (*Sibson, 2002*). *Reid (1910)* introduced the *elastic rebound theory* of the earthquake cycle. Tectonic plates are in relative motion at slip rates ranging from millimeters to few centimeters per year, while slip is locked by friction in few fault patches, which store elastic strain energy in the surrounding rocks. The earthquake is the result of a sudden relaxation of elastic strains through rupture along a fault. After this energy release, the fault locks again, resuming the elastic strain energy storing, and the cycle repeats.

This loading cycle can be divided into four stages: *preseismic*, *coseismic*, *postseismic* and *interseismic*. *Interseismic* features of the seismic cycle will be investigated in this thesis, focusing on the strength recovery of rocks during stationary contact periods (*quiescence*).

In nature, earthquakes quiescence periods range from weeks/months to tens/hundreds or thousands of years. These quiescence periods are stationary contact periods, over which the wallrocks of a locked fault accumulate elastic strain energy coming from tectonic forces. Assuming that a fault is storing elastic strain energy at a constant rate, and that at time $t = t_0$ the body is at position $u = 0$ and with acceleration $\ddot{u} = 0$, the system could be described kinematically by harmonic oscillator equations:

$$\ddot{u}(t) = (\Delta\sigma_k / m) - (k / m) \cdot u(t) \quad (1.8)$$

Where $u(t)$ (m) is the position as function of time t , $\ddot{u}(t)$ (m/s^2) is the second derivative of the position as function of time t , $\Delta\sigma_k$ (Pa) is the dynamic stress drop (i.e. the maximum difference between stress peak and kinematic stress when the oscillator moves), m (kg) is the mass of the oscillator and k (N/m) is the stiffness representing the elastic properties of the body.

The seismic cycle can be simplified as a spring-slider model (Figure 1.5). Consider a rigid block attached to a linear spring. The block moves with velocity V when a constant velocity V_0 is imposed at the other end of the spring (equivalent to the load point velocity used in the experiments), with a certain shear strength τ (Pa) at the contact surface. As long as the block holds, the spring stretches, storing more and more elastic strain energy (*stress buildup*). When the elastic strain energy (converted in elastic force) overcomes the frictional force, the block slides toward a new position u , and the cycle restarts. This simple model explains what happens at kilometers depth, in large volumes of the Crust, when a fault is stressed and is storing energy to then release it through seismic waves (radiated energy) and slip (dissipated energy).

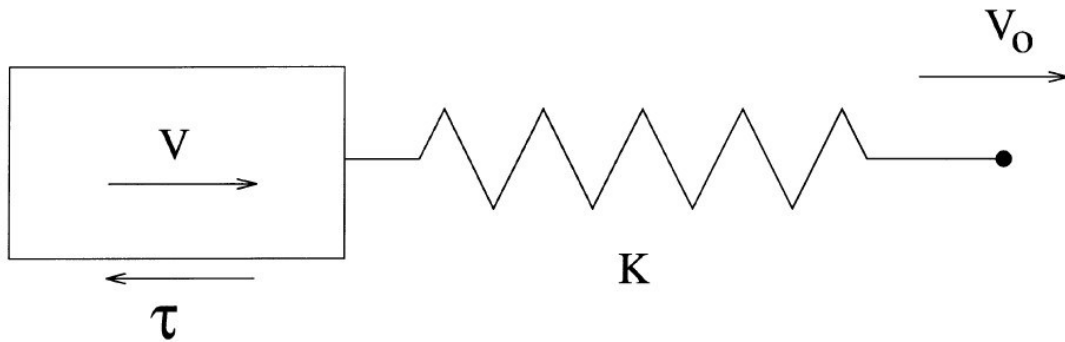


Figure 1.5. Spring-slider model (single degree of freedom) to describe the seismic cycle. From Ranjith & Rice (1999).

This particular motion, alternating loading under quasi-static conditions and sudden, high-velocity slip is known as *stick-slip* behavior, and is considered phenomenologically equivalent to the seismic cycle and earthquake slip along faults (e.g. Brace & Byerlee, 1966). The unstable, fast slip during the “slip” phase of the stick-slip motion occurs if the following condition (Ruina, 1983; Marone, 1998) is satisfied:

$$k < k_c = \sigma_n' (b - a) / D_c \quad (1.9)$$

Where k (N/m) is the stiffness of the loading system, k_c (N/m) is the critical stiffness boundary (between stable and unstable sliding), σ_n' (Pa) is the effective normal stress, $b - a$ is the friction rate parameter and D_c (m) is the critical slip distance (Scholz, 1988) (Figure 1.6). If the above condition is satisfied, frictional instabilities (unstable sliding) occur because the fault weakening rate, k_c , exceeds the rate of elastic unloading k , leading to a force imbalance (Figure 1.7). If the condition is not satisfied, it means that all the energy provided to the system is used to produce slip in equilibrium condition (stable sliding), and frictional steady state is reached (Figure 1.8).

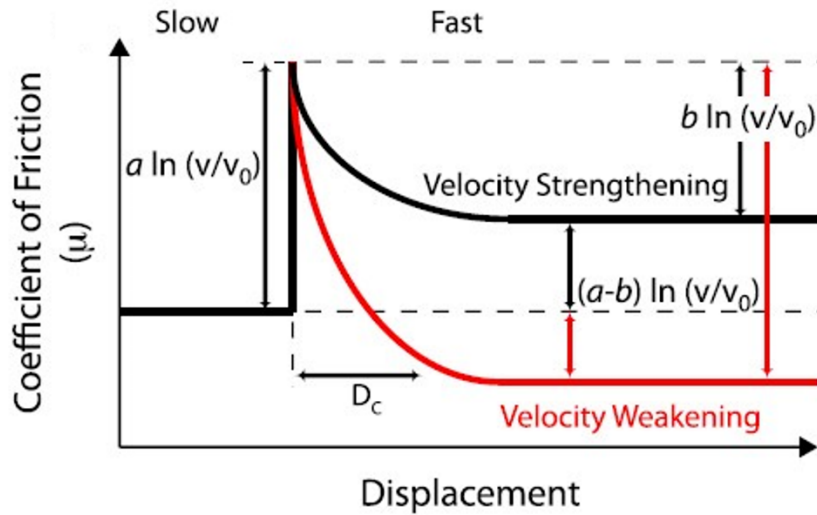


Figure 1.6. The parameter 'a' describes the direct effect on the friction coefficient as the load point velocity increases from 'slow' to 'fast', while 'b' describes the evolution effect as shear strength stabilizes after a critical slip distance D_c . From Scuderi et al., 2017.

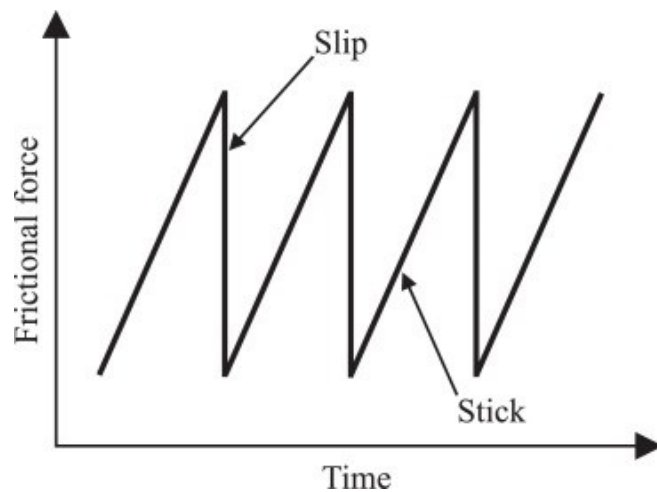


Figure 1.7. Ideal stick-slip motion. Loading/unloading cycles are frequently repeated if frictional instability occurs. From Naito et al. (2016).

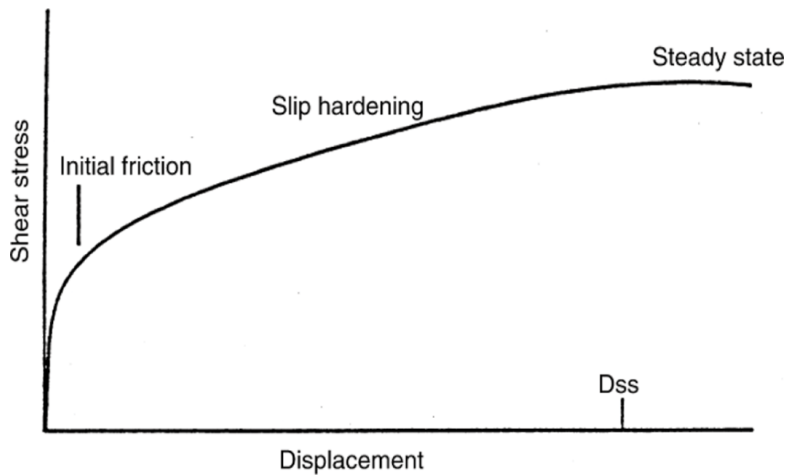


Figure 1.8. Stable sliding and steady state. From Scholz (2019).

During stationary contact periods, there can be physical-chemical processes that operate at the interface between the two stressed surfaces, altering the strength of the rock. It is widely accepted that the macroscopic quantification of the fault surface (apparent contact area) does not correspond to the microscopic real contact area within a fault. In fact, asperities (adhesive junctions, *Bowden & Tabor, 1950*) exist on all surfaces, and the real contact area is less than the apparent one (Figure 1.9). By this point of view, friction can be described as the failure of contact asperities that constitute the real contact area.

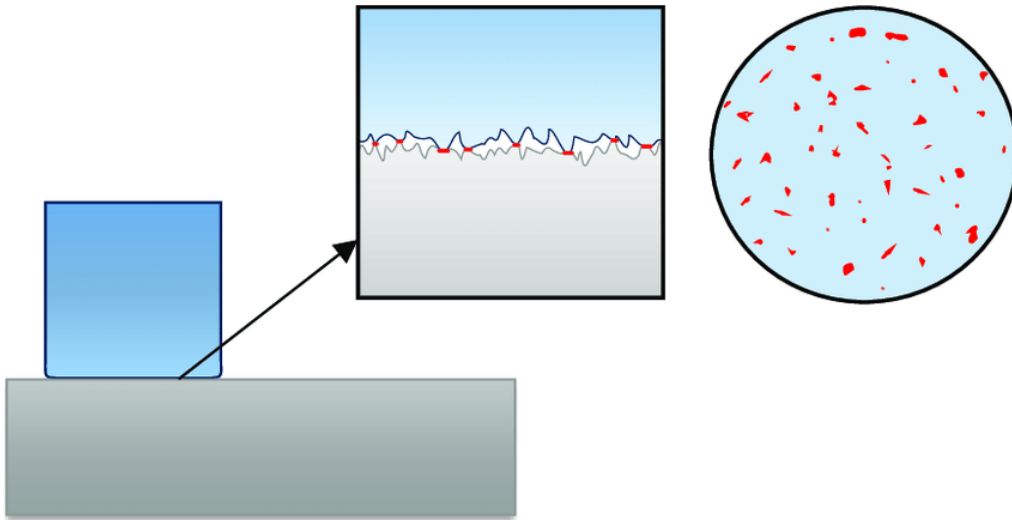


Figure 1.9. Apparent contact area vs. real contact area. From Rudnytskyj (2018).

The relevance of fault healing, the main focus of this thesis, is connected to the recurrence of earthquakes in nature and to the elastic strain energy released by earthquakes. If during stationary contact periods healing processes occur along the fault surface, the seismic cycle is altered. In fact, the seismic rupture of a fault almost invariably implies a drop in fault strength due to mechanical damage and thermal weakening mechanisms (*e.g. Di Toro et al., 2011 and references therein*). The healing of fault rocks is therefore instrumental both to allow the rock to regain strength and to store new elastic strain energy that will be used for subsequent seismic ruptures. Also, if grain-to-grain bonds increase their strength with fault healing, the fault rocks can store more elastic strain energy than before and (assuming a constant energy source due to tectonic forcing) so resulting in longer quiescence periods and larger seismic events. *Dieterich (1972)* investigated how and how much an experimental fault regained shear strength during stationary contact periods, confirming the time dependence of fault strength (Figure 1.10).

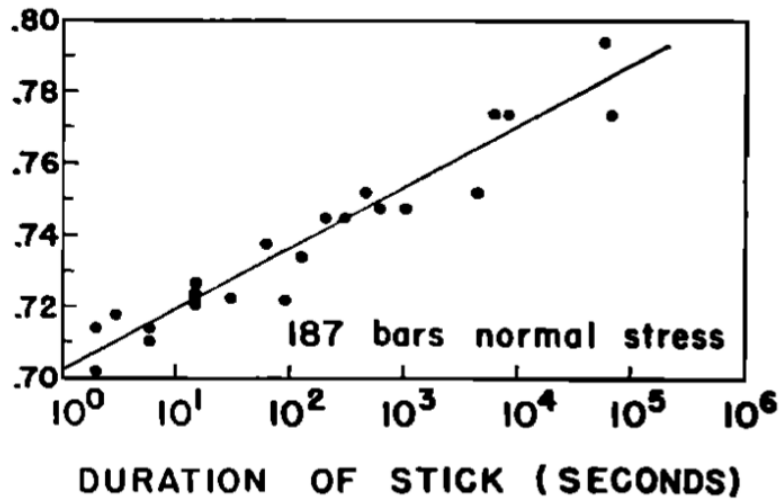


Figure 1.10. Time-dependence of frictional healing measured by Dieterich (1972). Friction coefficient increases linearly with increasing logarithm of hold time. From Dieterich (1972).

Frictional healing ($\Delta\mu$) is therefore defined as the shear strength recovery of a fault during quiescence periods. It is measured as the difference between peak, “static” friction and the dynamic friction measured during steady-state shearing until reshear.

$$\Delta\mu = \mu_{peak} - \mu_{ss} \tag{1.10}$$

Where μ_{peak} is the friction peak measured at reshear after a stationary contact period, and μ_{ss} is the steady state friction coefficient before the quiescence (Figure 1.11).

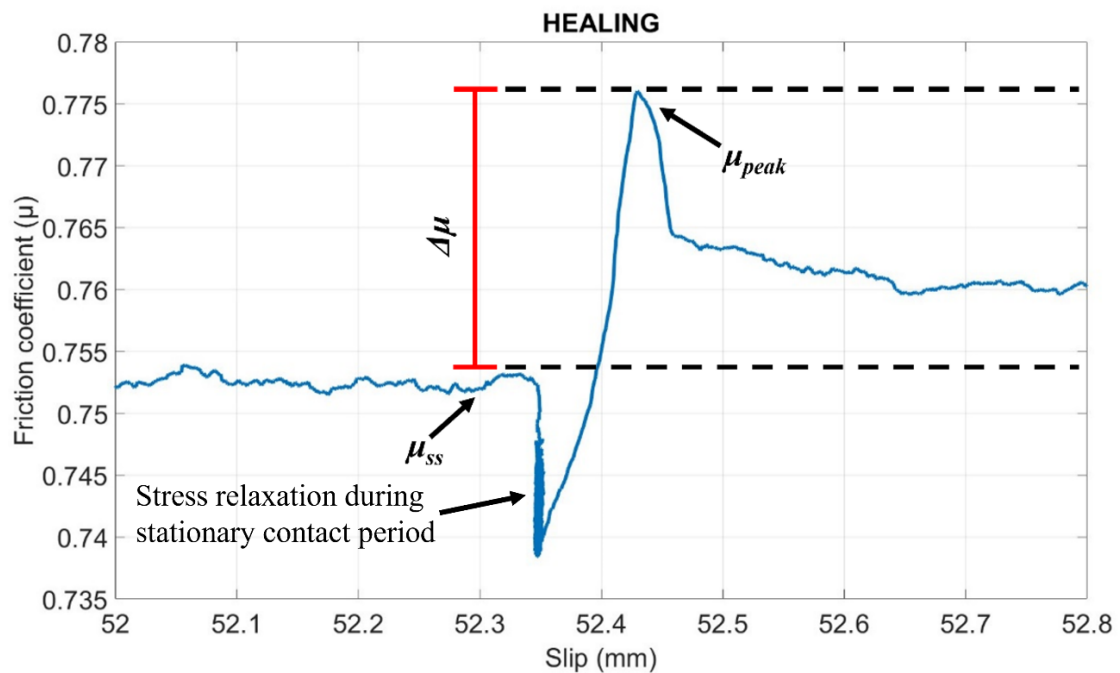


Figure 1.11. The experimental fault, having been locked for a certain stationary contact time, regains shear strength when it is slipped again.

This type of strength recovery, that follows a linear increase vs. Log(stationary contact time) has been known as “*Dieterich-type*” healing. During stationary contact periods, it has been demonstrated how real contact area increases with increasing time and effective normal stress (*Dieterich and Kilgore, 1994*), probably related to time-dependent plastic flow in the area of the contact points, which increases the area of the junctions (*Bowden & Tabor, 1964*). Beside the plastic increase of frictional contact area, other healing mechanisms exist: *Bos & Spiers (2002)* summarized and explained the features of all possible fault healing phenomena observable at grain-to-grain contacts (Figure 1.12).

Name	Driving force	Characteristics
1. "Dieterich"-healing	??	- $D_c = 10-100 \mu\text{m}$ - Strength increases linearly with $\log(t)$
2. Pressure solution	Effective normal stress at contact	- t-dependent - T-dependent - Compaction - Stress relaxation during hold
3. Fluid-assisted neck growth	Interfacial energy reduction	- t-dependent - T-dependent - No compaction, no stress relaxation
4. Precipitation/cementation	Solute supersaturation in advecting pore fluid	- can occur at $\sigma_n = 0$

Figure 1.12. Different healing mechanisms can operate at grain-to-grain contacts. Each mechanism has mechanical-microstructural characteristic features. From Bos & Spiers (2002).

In particular, many authors (*Nakatani & Scholz, 2004; Karner et al., 1997; Chen et al., 2015*) observed a healing mechanism different from the classical “*Dieterich-type*” one. In fact, this “*non-Dieterich-type*” healing, appeared to be activated only in the presence of liquid water, and enhanced by temperature (Figure 1.13). *Nakatani & Scholz (2004)* reported the mechanical features of the “*non-Dieterich-type*” healing they were investigating, finding out its dependence on temperature, on the presence of water and on its state. In particular, they focused on the study of pressure solution, a deformation mechanism whose kinetics was described by *Rutter (1976)*.

Pressure solution is a deformation mechanism based on solution-transfer in which dissolution of a mineral phase occurs at stressed grain-to-grain contacts into an aqueous pore fluid, followed by diffusion and reprecipitation in relatively low-stressed regions.

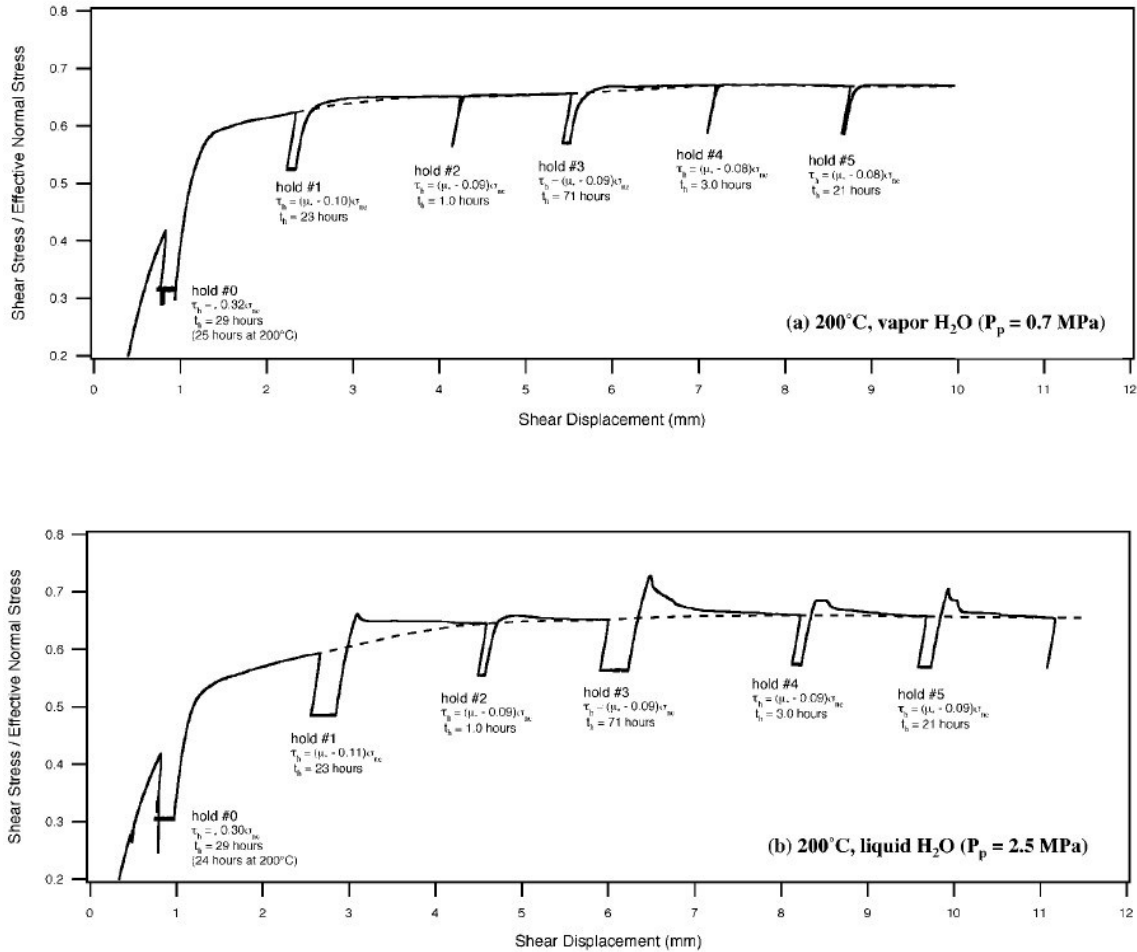


Figure 1.13. Different healing behavior in the presence of different water phases, suggestive of different operating healing mechanism. From Nakatani & Scholz (2004).

This diffusive mass transfer process is thought to be responsible for further bonding of grains at the stressed interface, by two means:

1. Indentation and interlocking of grains accompanied by porosity reduction.
2. Cementation of the neck of contact asperities with the material dissolved from high stress regions.

Both processes have the potential to contribute to a substantial increase of fault shear strength during stationary contact times.

Given the tremendous importance of the laboratory experimental approach (and its relevance for the interpretation of natural data) to the study of rock mechanics, this thesis focuses on performing a systematic series of laboratory frictional experiments, to

study in detail the process of fault healing with a standard material: quartz gouges. I studied the deformation of quartz gouges under hydrothermal conditions, simulating the behavior of this important crustal mineral in faults across the brittle-ductile transition. The main goal of my experiments was to understand how the mechanical behavior of a simulated fault gouge is affected by variations in temperature (from 23 °C to 400 °C), effective normal stress (from 10 MPa to 20 MPa), pore fluid pressure (from 6 MPa to 36 MPa) and grain size (F110 heterometric angular quartz and microquartz). Two different series of experiments were performed: the first, on F110 heterometric quartz gouges (<110 μm), changing temperature and stresses, and second, on microquartz (<5 μm). For the second experimental series, I repeated the same experiments of the first series, just with this thinner grain size. During each experiment, I performed one or two Slide-Hold-Slide tests (SHS), an experimental procedure designed to investigate the healing mechanism that operates under the different P-T conditions.

Chapter 2

Methods

2.1 Description of the experimental apparatus

The frictional experiments in this thesis were performed exploiting the Low to High-Velocity Rotary Shear Apparatus “RoSA” (Figure 2.1), installed in the Rock Mechanics Laboratory of the Department of Geosciences in the University of Padova (UNIPD), equipped with the hydrothermal pressure vessel (HYDROS). RoSA-HYDROS has been designed by Prof. Shimamoto (Beijing, Institute of Geology, China Earthquake Administration).

RoSA-HYDROS can perform frictional tests in rotary/torsion configuration under different P-T conditions. An axial load, used

to apply normal stress to experimental fault surfaces, up to 12 kN. Fluid pressure within the vessel, used to apply confinement and fluid saturation to the samples, up to 70 MPa. Slip velocity, applied to the laboratory faults can range from 10 mm/year (slow slip / fault creep velocity) to 1.5 m/s (coseismic velocity) and especially in the presence of pressurized fluids.

The apparatus consists of a load frame containing a 20 kN Bellofram cylinder (air



Figure 2.1. Photo of RoSA-HYDROS apparatus installed at UNIPD. Front view.

actuator) that applies the axial (vertical) load. The top of the frame contains 11 kW servomotor with a torque capability of 70 Nm, that applies torsion to the samples via a gear-belt system. Within the frame there is an axial column that transmits axial load and torque to the sample and to the loading frame. The axial column is attached to a cantilever type torque gauge, an axial force gauge and an axial displacement transducer (used to measure axial shortening of the column and correlates with the vertical compaction of the sample). The specimen chamber is located along the axial column above the Bellofram cylinder and set in the main press. A ball bearing ring is placed between the axial piston and the axial force gauge so a torque can be supported only by the torque gauge. The sample and sample holders are inserted along the axial column in a cylindrical configuration (see below for further details).

HYDROS is a hydrothermal pressure vessel made of that is mounted to envelop the central part of the axial column, around the sample to apply a water fluid pressure in and around the sample. Fluids can be heated up with an external furnace. HYDROS consists of pressure vessel (5 in the Figure 2.2), upper and lower glands to seal pressure, upper and lower nuts to hold the glands into the pressure vessel, the upper rotary piston, and the lower stationary piston. The pressure vessel, the two glands, and the two nuts are made of Inconel 625 (temperature resistant high-strength alloy). The pore fluid pressure is controlled by an ISCO syringe pump (on the right in Figure 2.1) which is connected to the top part the upper gland. The top and bottom parts of the upper and lower pistons have hexagonal shapes. Those are inserted into hexagonal holes in a rotary piston and in the lower header block to prevent rotations of the pistons. Water pressure in the vessel acts as pore pressure when no jacket is used for specimens, as in most rotary shear low to high-velocity friction experiments. The lower stationary piston is connected to the lower header block which has ports to a pressure transducer, to an external pore-pressure generating system and to four thermocouples. The pressure vessel is equipped with an external split furnace with coiled Kanthal AF, with a ceramic casing made of cordierite to set up the heating wire in grooves, covered with powdery insulator (MICROTHERM) with a thermal conductivity as low as that of air. This insulator keeps the temperature at the outside the furnace below 50-60 °C without cooling the pressure vessel when the specimen temperature is around 500 °C. On the other hand, O-rings are made of rubber and must be protected from high temperatures, and glands with O-rings are cooled by circulating cooling water coming from a chiller (on the left in Figure 2.1) providing a cooling temperature of 15-16 °C and so preventing the jamming of the machine.

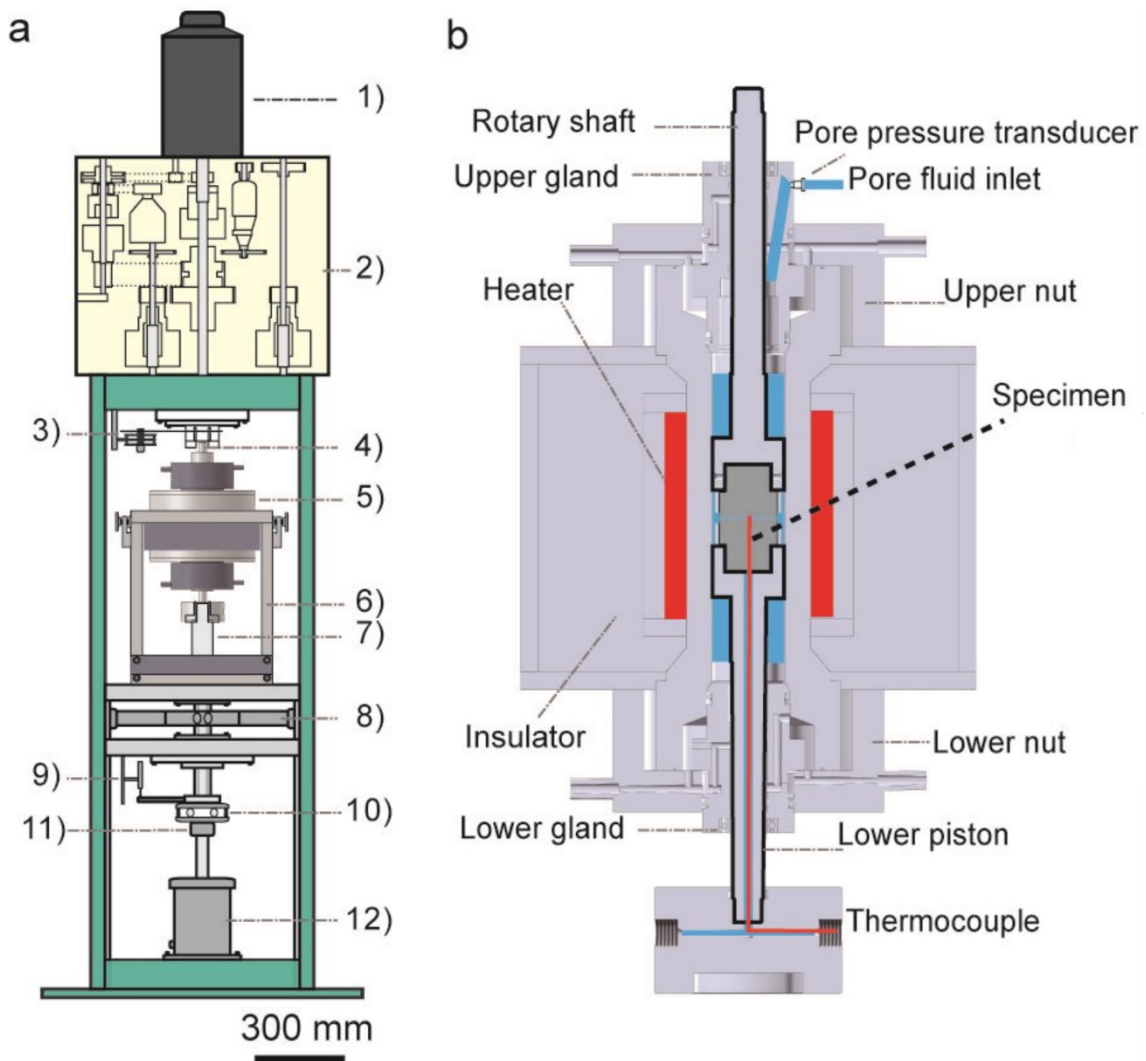


Figure 2.2. The Low to High-velocity rotary shear apparatus, equipped with a dedicated hydrothermal vessel (modified from Ma et al., 2014). a) 1) servomotor, 2) gear and belt system, 3) rotary encoder and potentiometer, 4) rotary shaft, 5) hydrothermal pressure vessel, 6) metal frame, 7) axial loading column, 8) cantilever-type torque gauge, 9) liner variable differential transducer, 10) thrust bearing, 11) axial force gauge, 12) air actuator. b) The sketch of the hydrothermal vessel “HYDROS” with the main parts indicated in the diagram.

The pore fluid can reach a pressure up to 70 MPa and a temperature of approximately 500 °C (from subcritical to supercritical conditions).

The RoSA apparatus and the HYDROS vessel are both controlled and monitored via the Main Control Unit and control PC (Figure 2.3). The main control unit allows the stop and the restart of the rotation of the torque motor and shows the live measurements of vertical load, shear torque, angle of rotation, tachometer (number of rotations per minute), vertical

displacement and pulse counter.

The custom software “EDX-100A” (Kyowa Electronic Instruments Ltd. https://www.kyowaei.com/eng/support/download/software_program/license/edx100a_soft_01.00_02_eng.html), was used to monitor and control the machine (Figure 2.3).

All the experiments were conducted on quartz gouges. For all the experiments, the samples were put into a cylindrical stainless steel sample holder of 28 mm outer diameter and 10 mm internal diameter (for a shearing surface of $0.537 \cdot 10^{-3} \text{ m}^2$) and jacketed with Nickel-and Aluminum-made rings, to avoid failure problems during the tests. Grooved sample holder was used to avoid localization of slip in the quartz-SS interface.



Figure 2.3. Custom Software “EDX-100A” while monitoring a frictional experiment.



Figure 2.4. Disassembled pressure vessel.

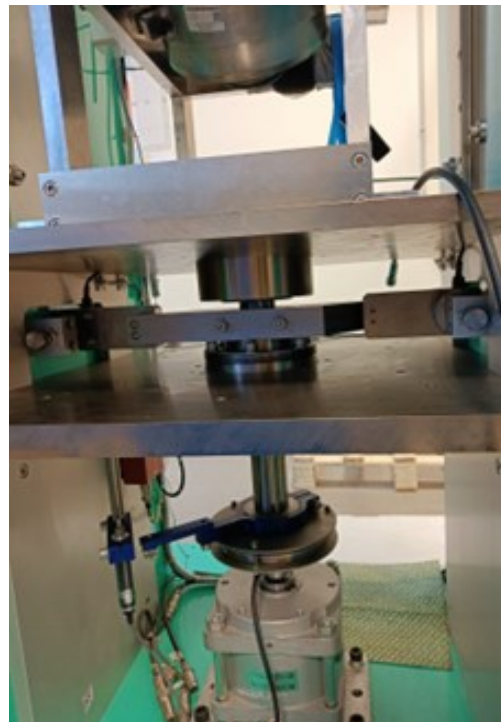


Figure 2.5. Focus on the lower part of RoSA. Front view.

2.2 Experimental strategy and procedure

I performed 10 frictional experiments to study the frictional healing of quartz gouges at different temperatures and with increasing fault cumulative slip/shear strain. The experiments are subdivided into two distinct series.

The first series comprises 6 tests conducted on F110 heterometric angular quartz ($<110\ \mu\text{m}$), while second series comprises 4 tests conducted on microquartz ($<5\ \mu\text{m}$), to investigate the effect of the grain size on the mechanical behavior of the quartz gouges.

During each experiment, I performed Slide-Hold-Slide (SHS hereinafter) tests, in which stationary contact periods (Hold) alternate with sliding periods (Slide), to understand how and how much a laboratory fault regain shear strength during stationary contact periods (healing).

The purpose of this thesis was to investigate the mechanical properties of a simulated fault gouge under hydrothermal conditions. The selected values of effective normal stress and temperature for each experiment were calculated in order to maintain water in liquid conditions, except for two “end member” tests, performed in the presence of water under supercritical conditions (Figure 2.6).

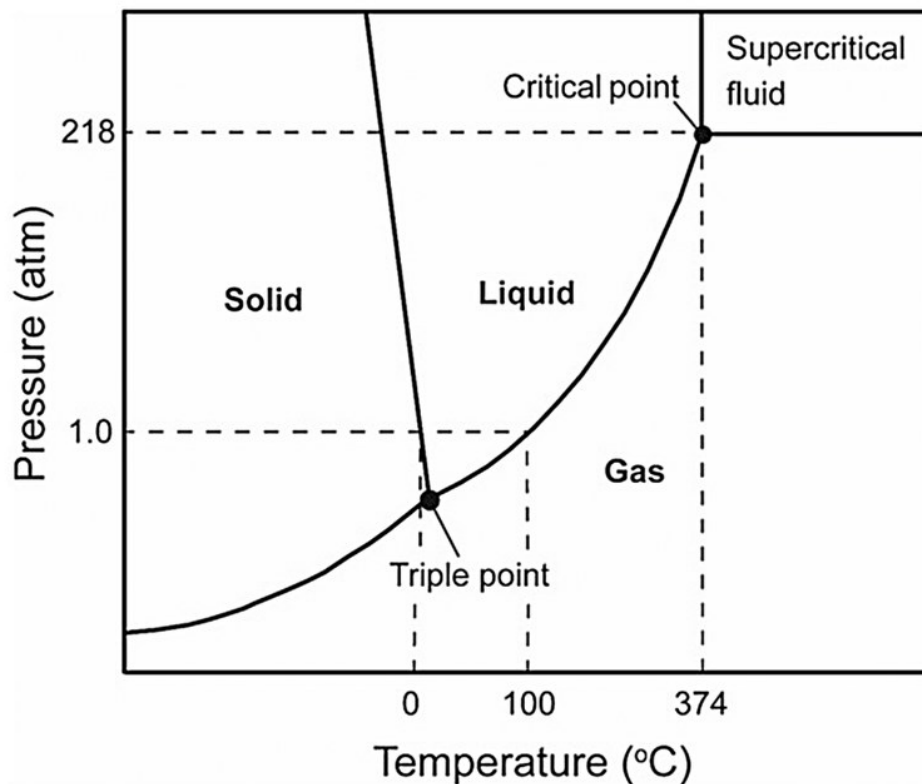


Figure 2.6. Phase diagram of water.

Table 1 summarizes the experimental series showing the main experimental conditions.

	Sample type	Sample weight (g)	Sample thickness (mm)	Temperature (°C)	Fluid Pressure (MPa)	Effective normal stress (MPa)	Sliding velocity (µm/s)
R 356	F110 heterometric angular quartz	3.4	3.5	200	36	10	10
R 359	F110 heterometric angular quartz	1.2	1.3	200	6	20	10
R 361	F110 heterometric angular quartz	1.2	1.2	100	6	20	10
R 364	F110 heterometric angular quartz	1.2	1.1	400	36	10	10
R 366	F110 heterometric angular quartz	1.2	1.4	23	36	10	10
R 383	F110 heterometric angular quartz	1.2	1.4	23	36	10	10
R 368	Microquartz	1.2	1.2	200	36	10	10
R 370	Microquartz	1.2	1.3	23	36	10	10
R 372	Microquartz	1.4	1.5	100	36	10	10
R 374	Microquartz	1.5	1.6	400	36	10	10

Table 1. Experimental conditions are shown for each experiment.

Experimental procedure

The used experimental procedure consists in:

1. Sample preparation and apparatus assembly.

Except for the experiment R 356, I used 1.2-1.5 g of quartz powder for every experiment, resulting in a sample thickness ranging from 1.1 to 1.6 mm. The samples were put into a cylindrical stainless steel sample holder of 28 mm outer diameter and 10 mm internal diameter (for a shearing surface of $0.537 \cdot 10^{-3} \text{ m}^2$) and jacketed with Nickel-and Aluminum-made rings, to avoid failure problems during shearing. Grooved sample holder was used to avoid localization of slip in the quartz-SS interface. Once the sample holder was ready to be installed in the apparatus, O-rings of the upper and lower gland were smoothed with a silicon-based grease that act as a lubricant (with high thermal and chemical stability) to avoid jamming of the components. Subsequently, the mounted sample holder with the lower nut and the lower header block attached was assembled within the tilted vessel. Then, the upper gland was inserted through the upper column and all the sensors were connected to the machine, ready to the start of the experiment.

2. Achievement of the experimental conditions (fluid pressure, axial load and temperature) and wait a standard amount of time for chemical equilibrium (2 hours).

To achieve the desired experimental conditions in terms of effective normal stress (σ_n'), the axial load was progressively increased using the air actuator, while the pore fluid pressure (P_p) was progressively increased too, using the ISCO syringe pump. Once the σ_n' - P_p conditions needed were reached, the temperature (T) was increased by the external furnace.

I used to wait around 2 hours to let the sample and the fluid reach a chemical equilibrium, which is function of the saturation degree S in the quartz-water system, proposed by *Rimstedt & Barnes (1980)*, *Karner et al. (1997)*:

$$S = 1 - e^{-k_t \cdot t} \quad (2.1)$$

$$\text{Where } k_t = (A/M \cdot M_0/A_0) \cdot \gamma H_2SiO_4 \cdot k \quad (2.2)$$

A is the interfacial area, M is the mass of the water, M_0/A_0 is the extent of a standard system, γ is the activity coefficient and k is the precipitation constant.

The combination of the equation above with the equilibrium constant and Arrhenius relations gives an expression that describes the temperature dependence of the time taken to reach equilibrium:

$$t = 5t_c = 5e^{(Ea/RT)} \cdot [\alpha \cdot aH_2SiO_4]^{-1} \cdot (M/A) \quad (2.3)$$

For *Karner et al. (1997)*, the frictional properties measured from SHS tests under hydrothermal conditions may depend on the concentration of silica.

3. Run-in (initial shear).

A controlled rotation velocity was imposed to the apparatus through the main control unit, corresponding to an effective sliding velocity of the experimental fault of 10 $\mu\text{m/s}$, calculated in an arbitrary radius which is around 2/3 of the sample holder external radius.

The experiment starts with an initial run-in, ranging from 15 mm to 50 mm, at a slip rate of 10 $\mu\text{m/s}$, to reach steady state in terms of shear torque and, if possible,

compaction. This phase is characterized by a slip hardening and compacting behavior. Once the elastic strain energy provided by the apparatus is counterbalanced by the energy used in the sample to generate heat, create new cracks and/or propagate old ones, the steady state is reached.

4. SHS test.

After the initial run-in, the SHS test is performed including a series of 1-2 mm slides alternating with increasing hold time (usually from 10 to about 50000 s). During the hold, the rotation of the column is halted and the stress starts to spontaneously relax, reaching μ_r values. During the reshear phase (slide), the data reveal how the experimental fault regain shear strength during stationary contact periods, under the P-T conditions investigated. Healing values ($\Delta\mu$) are computed as:

$$\Delta\mu = \mu_{peak} - \mu_{ss} \quad (2.4)$$

Where μ_{peak} is the friction peak that follow a reshear after a stationary contact period, and μ_{ss} is the dynamic friction coefficient when the sample was sliding before being halted (Figure 2.7).

The healing rate parameter (β) was computed using this equation:

$$\Delta\mu = \beta / \log(t_{hold}). \quad (2.5)$$

5. High-strain slide and second SHS stage.

After the last long hold, in experiments R 364, R 366, R 370, R 372 and R 374 I used to perform a new 10-15 mm slide and then repeat the SHS test, to investigate the effect of the shear strain on the mechanical response of the gouge.

Usually, the first SHS test was performed when the sample experienced a cumulative slip ranging from 15 to 50 mm, while the second SHS test after 50 to 90 mm of slip (Figure 2.8).

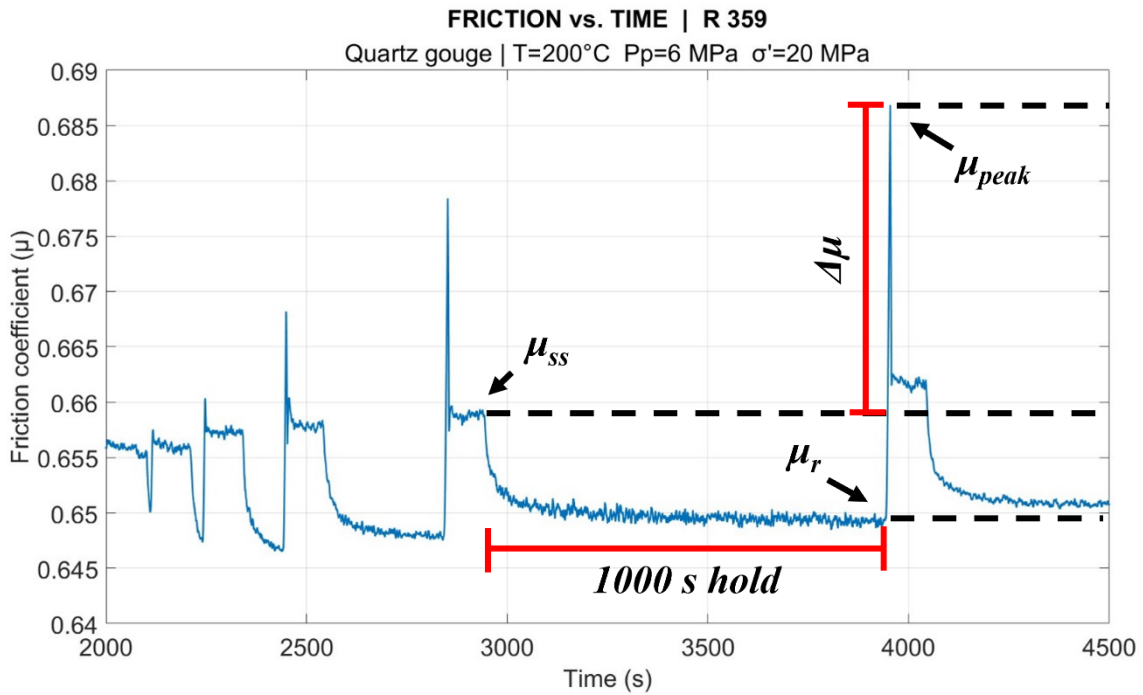


Figure 2.7. Typical Slide-Hold-Slide (SHS) series is shown. The shear stress relaxes during stationary contact periods, to then regain strength when reshear occurs.

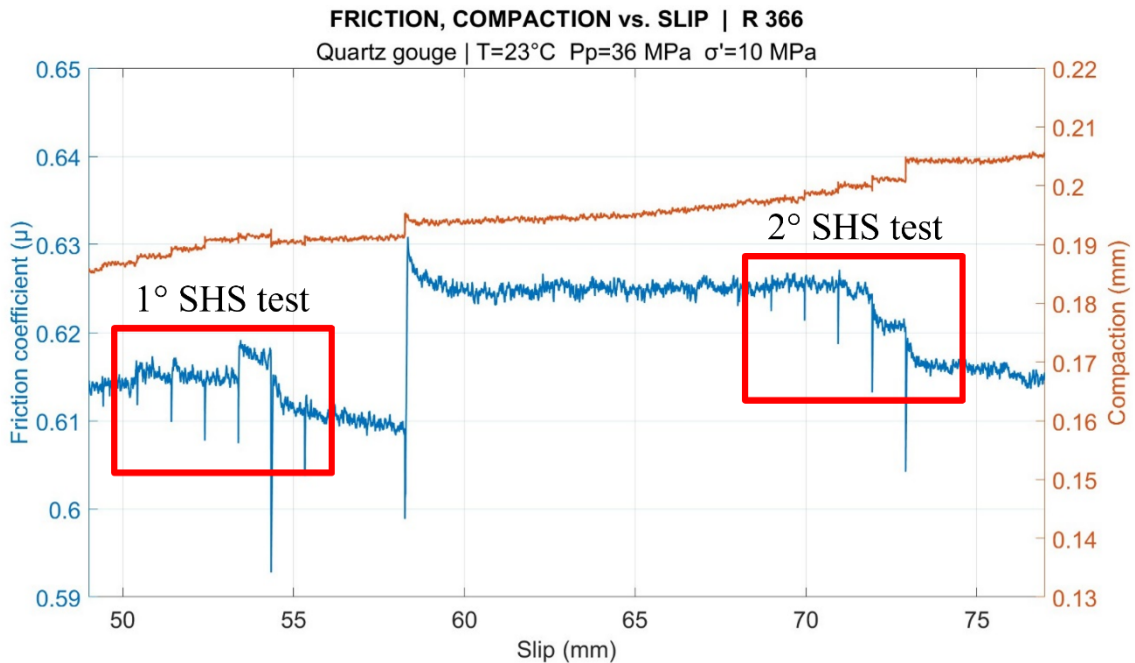


Figure 2.8. Experiment R 366. Two different SHS tests were conducted: the first after a cumulative slip of 50 mm and the second after a cumulative slip of 70 mm. In the middle, 10 mm slip to investigate different shear strain conditions of the sample.

6. Extraction of the sample from the apparatus.

At the end of every experiment, the samples were gently removed from the sample holder and dried off, trying to preserve them for microstructural/microanalytical analysis.

Unfortunately, as reported by many authors, the quartz gouge is very difficult to be removed correctly without breaking and/or disaggregating it (Figure 2.9).



*Figure 2.9. Quartz gouge sample extracted from RoSA.
Sample holder's grooves are visible.*

2.3 Data cleaning and analysis

To perform data cleaning and analysis I used “*Matlab*”, a programming and numerical computing environment widely used in scientific and engineering domains. Output data from the machine were:

- Time (s)
- Vertical load (kN)
- Vertical displacement (mm)

- Shear torque (N · m)
- Upper fluid pressure (MPa)
- Lower fluid pressure (MPa)
- Fluid temperature (°C)
- Furnace temperature (°C)
- Room temperature (°C)
- Angle (°)
- Tachometer (rpm)
- Pulse counter.

I had to convert shear torque (kN) and angle (°) measurements into geological oriented data, since I was interested in analyzing the friction coefficient (μ) and the slip (mm) occurred during the experiments.

Regarding the shear torque (kN), these were the calculations to obtain the friction coefficient (μ):

$$T = F_s \cdot r \Rightarrow F_s = \frac{T}{r}, \quad (2.6)$$

Where T (N·m) is the shear torque, F_s (N) is the shear force applied from the machine to the sample and r (m) is the radius of the sample holder.

$$\tau = \frac{F_s}{A} \Rightarrow F_s = \tau \cdot A, \quad (2.7)$$

Where τ is the shear stress (Pa) and A (m²) is the sliding area of the sample.

$$\Rightarrow \frac{T}{r} = \tau \cdot A \Rightarrow \tau = \frac{T}{r \cdot A}. \quad (2.8)$$

The shear torque value was then integrated along the radius of the sample, knowing that the internal radius is 5 mm, while the external one was 14 mm:

$$\text{Since } A = \pi \cdot r^2 = \int_0^r 2\pi r \cdot dr \quad (2.9)$$

$$\Rightarrow \tau^{-1} = \int_5^{14} \frac{r \cdot \pi r}{T} \cdot dr = \frac{2\pi}{T} \int_5^{14} r \cdot dr = \frac{2\pi}{3T} [r^3]_5^{14} \quad (2.10)$$

Then, the friction coefficient was obtained by normalizing the shear stress by the effective normal stress applied:

$$\mu = \frac{\tau}{\sigma_n}, \quad (2.11)$$

Regarding the angle measurements ($^\circ$), slip (mm) depends on the position along the radius of the circular sample.

I calculated the equivalent velocity v_e for one revolution per minute (from *Hirose & Shimamoto, 2005*):

$$v_e = \frac{4\pi R(r_i^2 + r_i r_o + r_o^2)}{3(r_i + r_o)}, \quad (2.12)$$

Where R is the number of revolutions per minute (rpm), r_i is the internal radius and r_o is the outer radius.

Given this, the equivalent displacement ((slip (mm))) was computed through this relation:

$$d_e = v_e \cdot t. \quad (2.13)$$

Once the friction coefficient and slip values were computed, I cleaned the data by smoothing them using the “*smoothdata*” function on *Matlab*. Precisely, I used a moving mean method in which a window of 31 points was considered. It’s noted that the sampling rate of the experiments was 10 Hz.

For each experiment, I determined the reference value of the friction (μ) by the mean value within selected data intervals where the friction was stable and constant throughout a relatively long period (e.g. during steady state sliding range between 10-25 mm). The associated uncertainty has been determined by the standard deviation of the measurements with respect to the mean value, e.g., $\mu = 0.65 \pm 0.002$.

Chapter 3

Results

3.1 Mechanical data

In the following, I show the mechanical results of all the performed experiments, in terms of friction coefficient (μ), compaction (mm) and slip (mm). For each experiment, the first graph gives an overview of the friction and compaction evolution throughout the test. The second graph is dedicated to zoom in to the SHS tests that have been used to evaluate the frictional healing ($\Delta\mu$). “*Qg*” or “*Quartz gouge*” on the figures are abbreviations of “F110 Heterometric angular quartz”, while “*Mq*” is the abbreviation of “Microquartz”. A discussion of the results will be found in the following chapter.

Experiment R 356

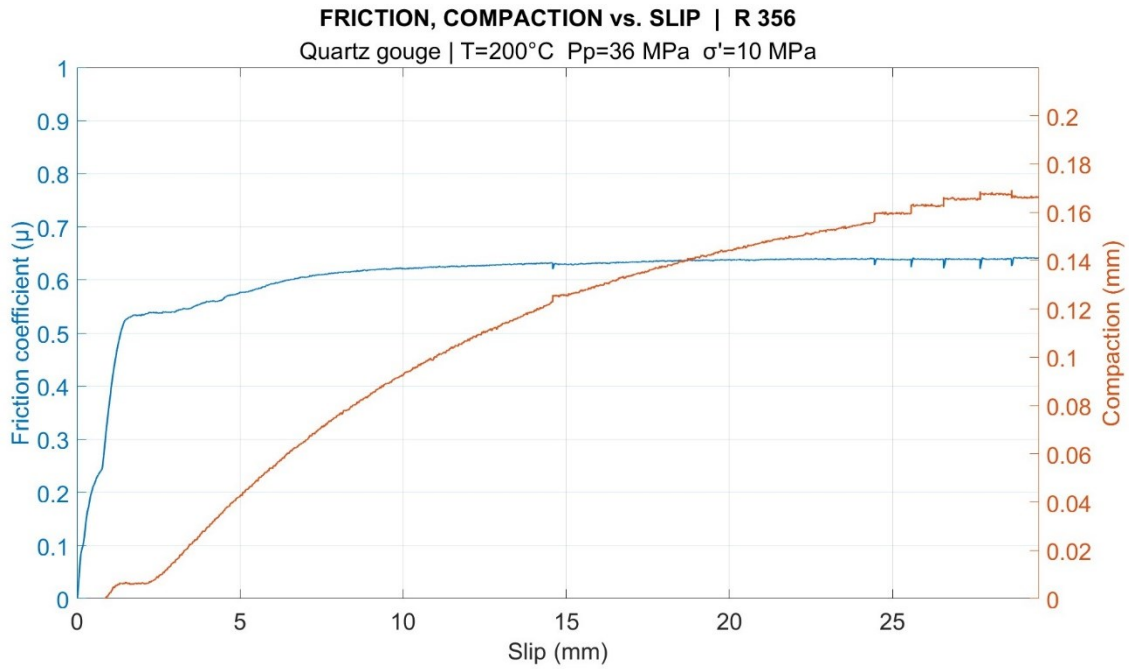


Figure 3.1. General overview of experiment R 356. Friction (μ) and compaction (mm) plotted against slip (mm).

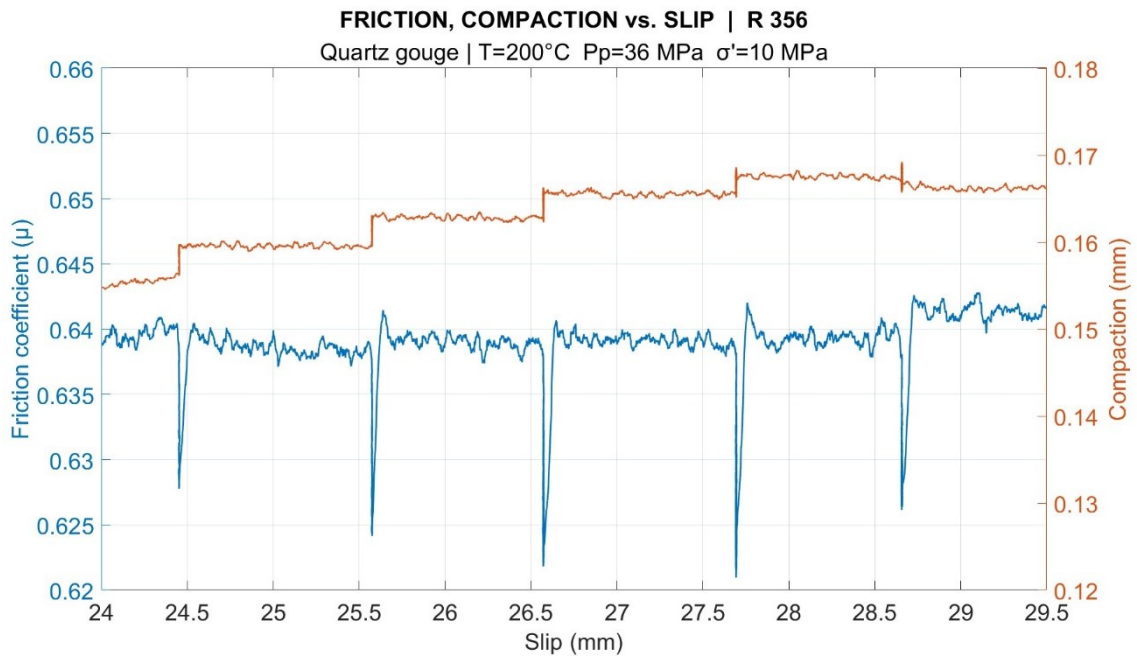


Figure 3.2. Experiment R 356. Zoom on the SHS test. Friction (μ) and compaction (mm) plotted against slip (mm).

Experiment R 359

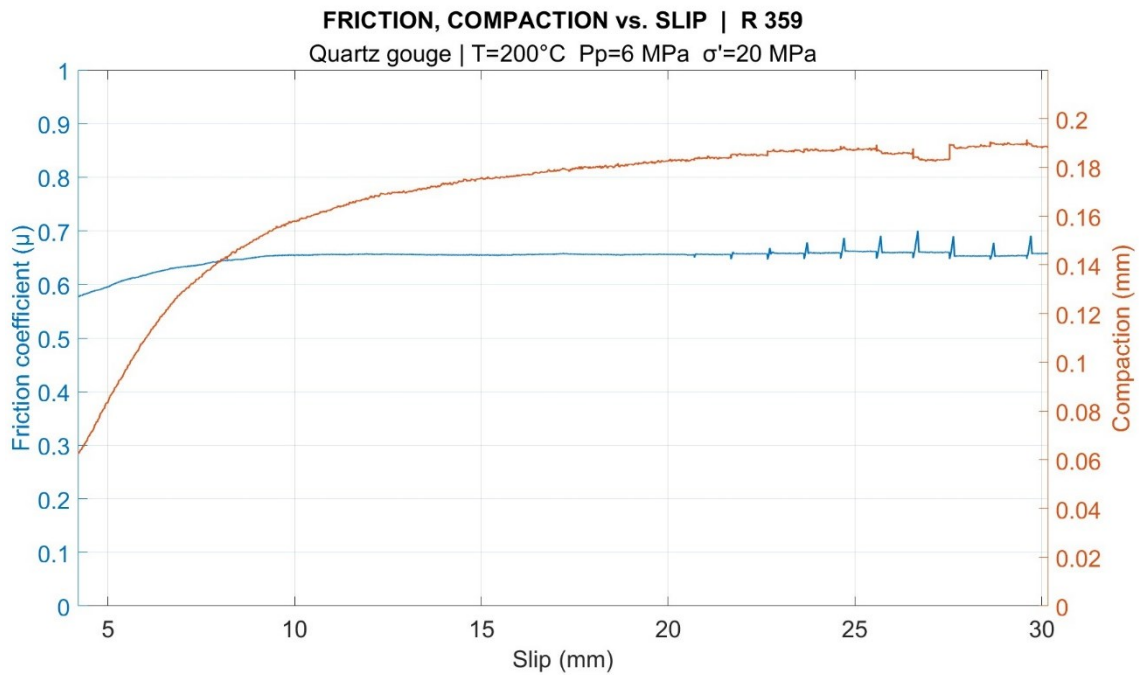


Figure 3.3. General overview of experiment R 359. Friction (μ) and compaction (mm) plotted against slip (mm).

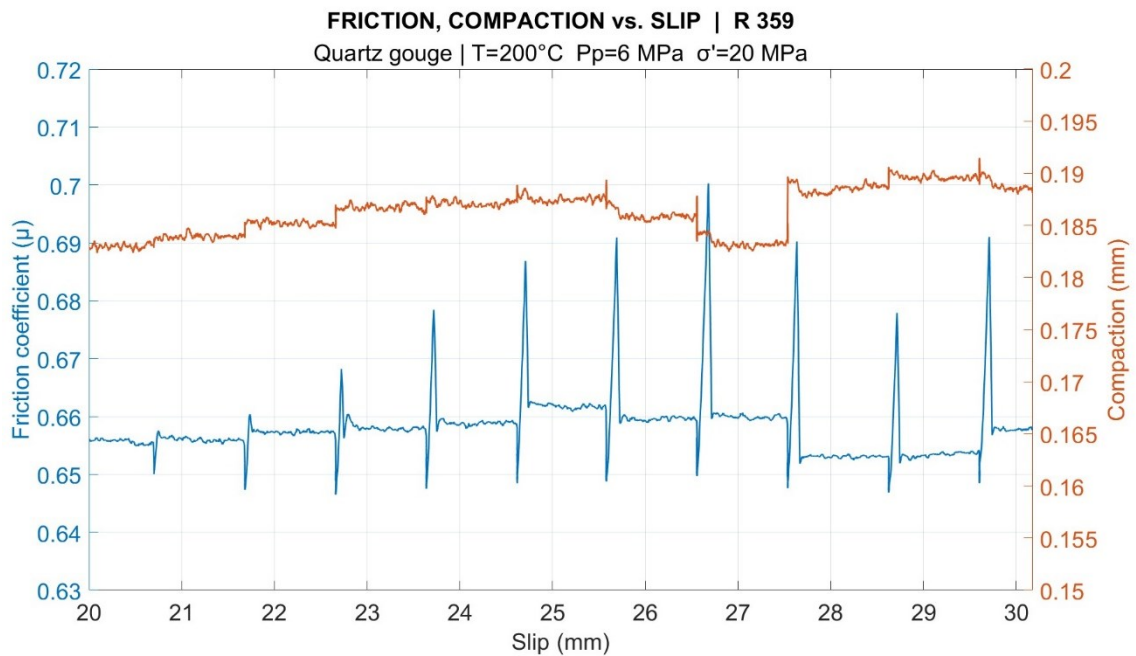


Figure 3.4. Experiment R 359. Zoom on the SHS test. Friction (μ) and compaction (mm) plotted against slip (mm).

Experiment R 361

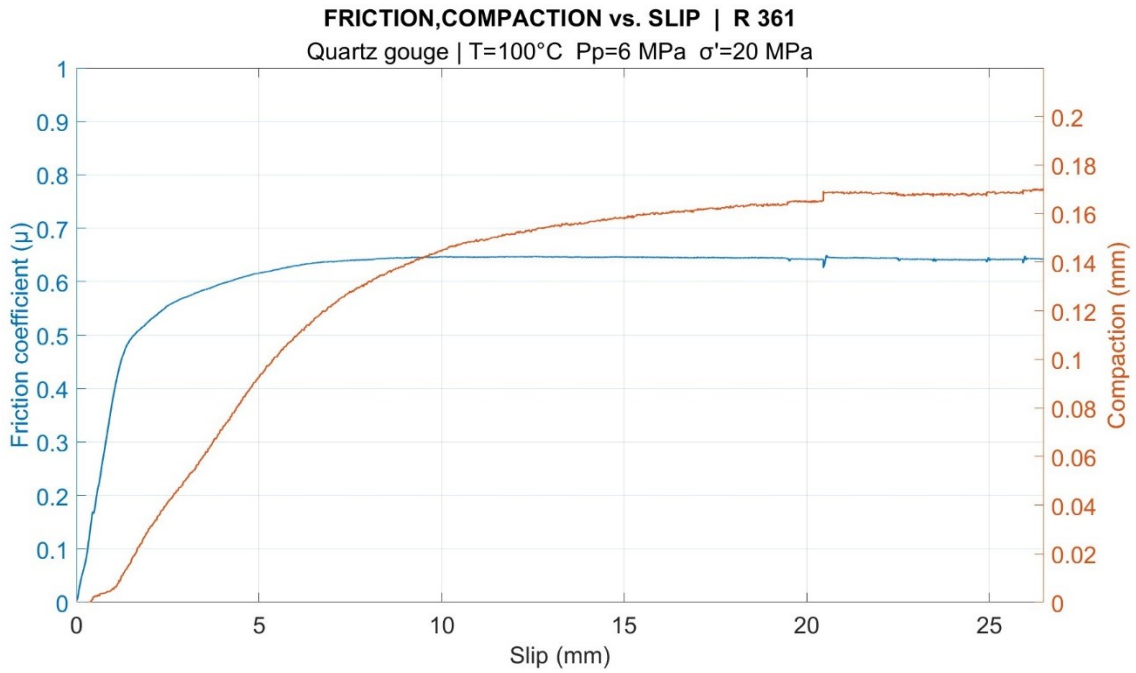


Figure 3.5. General overview of experiment R 361. Friction (μ) and compaction (mm) plotted against slip (mm).

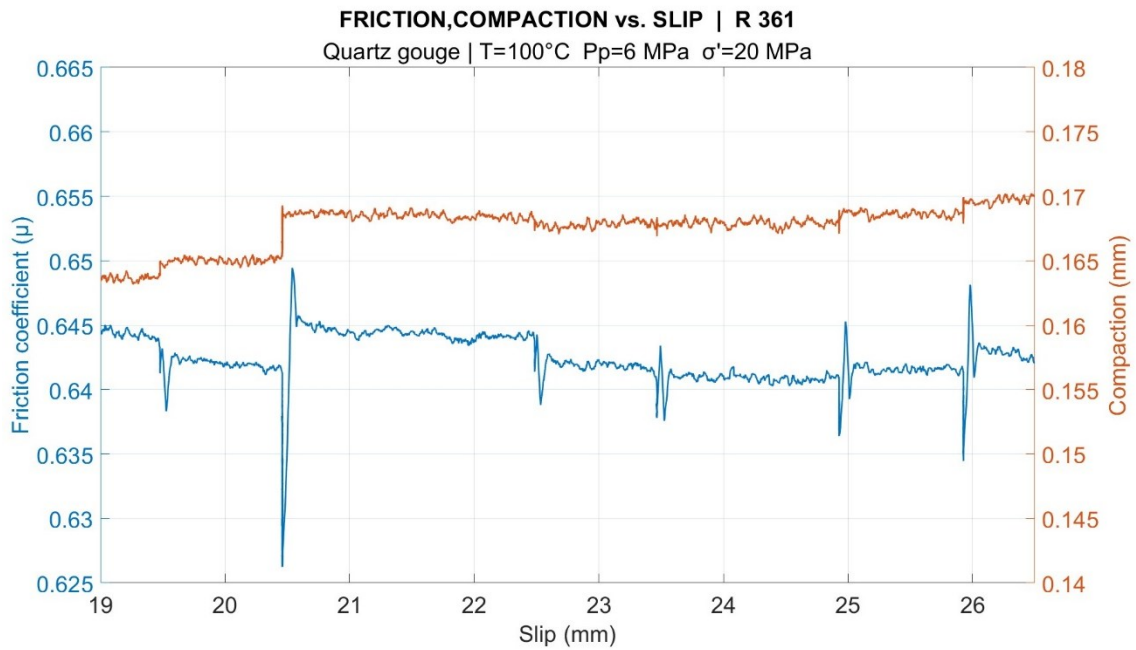


Figure 3.6. Experiment R 361. Zoom on the SHS test. Friction (μ) and compaction (mm) plotted against slip (mm).

Experiment R 364

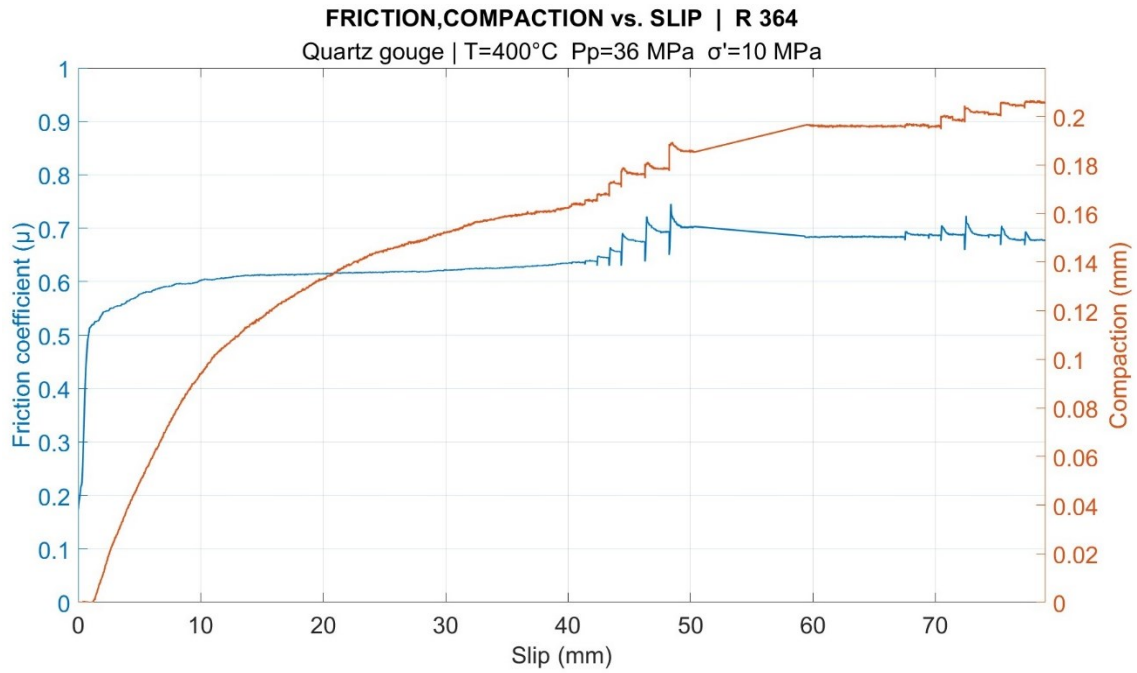


Figure 3.7. General overview of experiment R 364. Friction (μ) and compaction (mm) plotted against slip (mm).

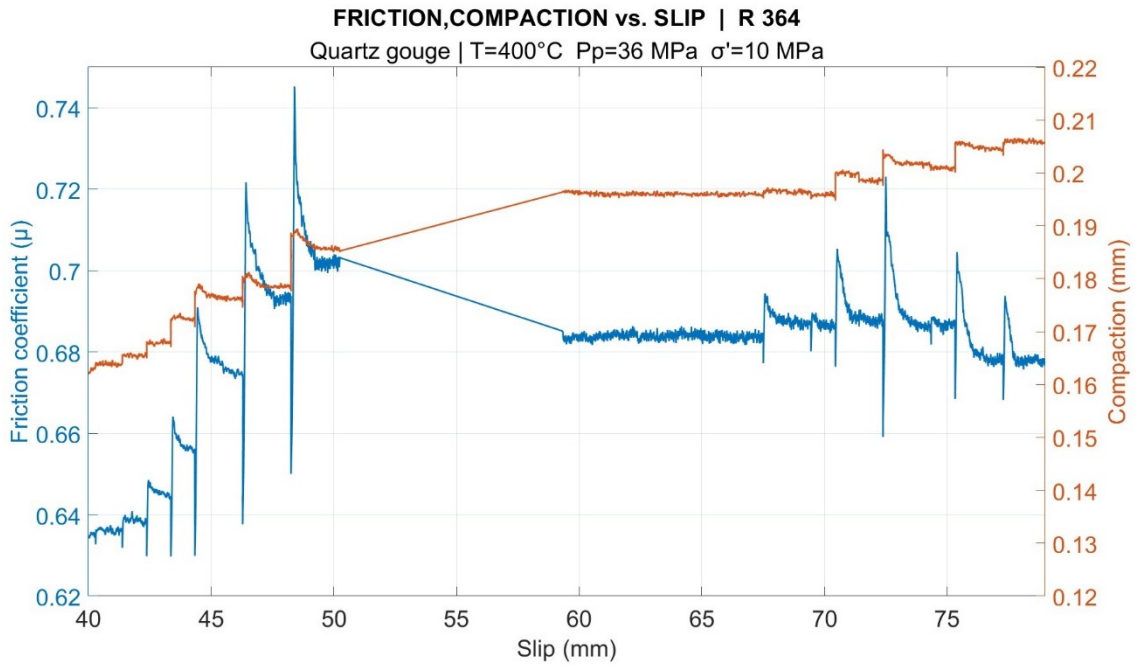


Figure 3.8. Experiment R 364. Zoom on the SHS test. Friction (μ) and compaction (mm) plotted against slip (mm).

Experiment R 366

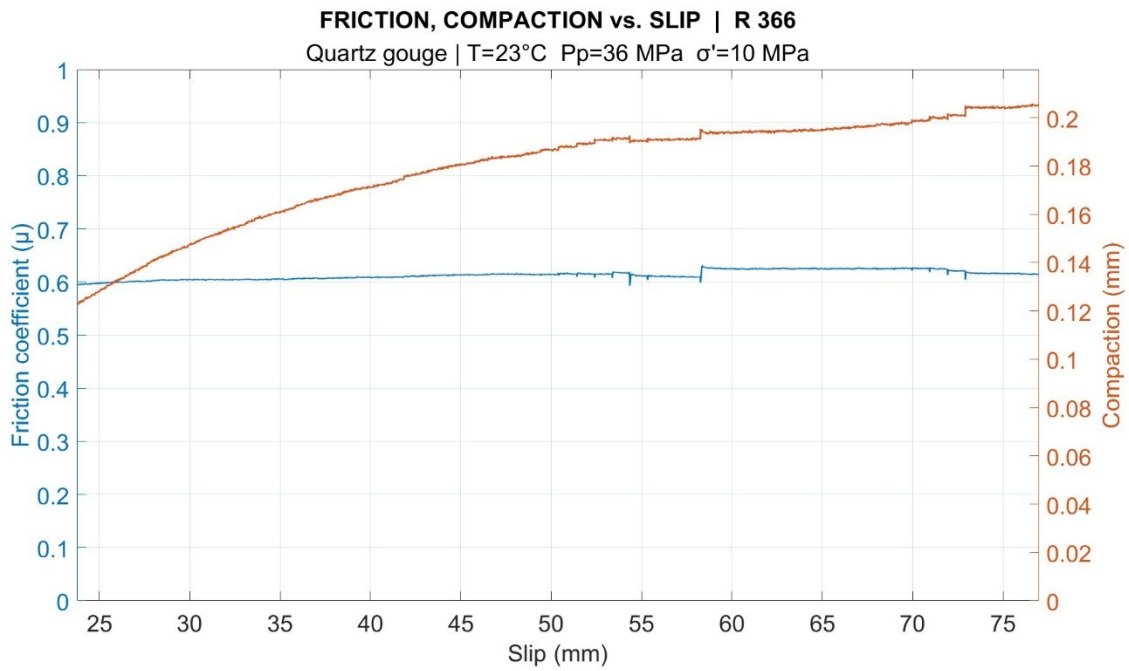


Figure 3.9. General overview of experiment R 366. Friction (μ) and compaction (mm) plotted against slip (mm).

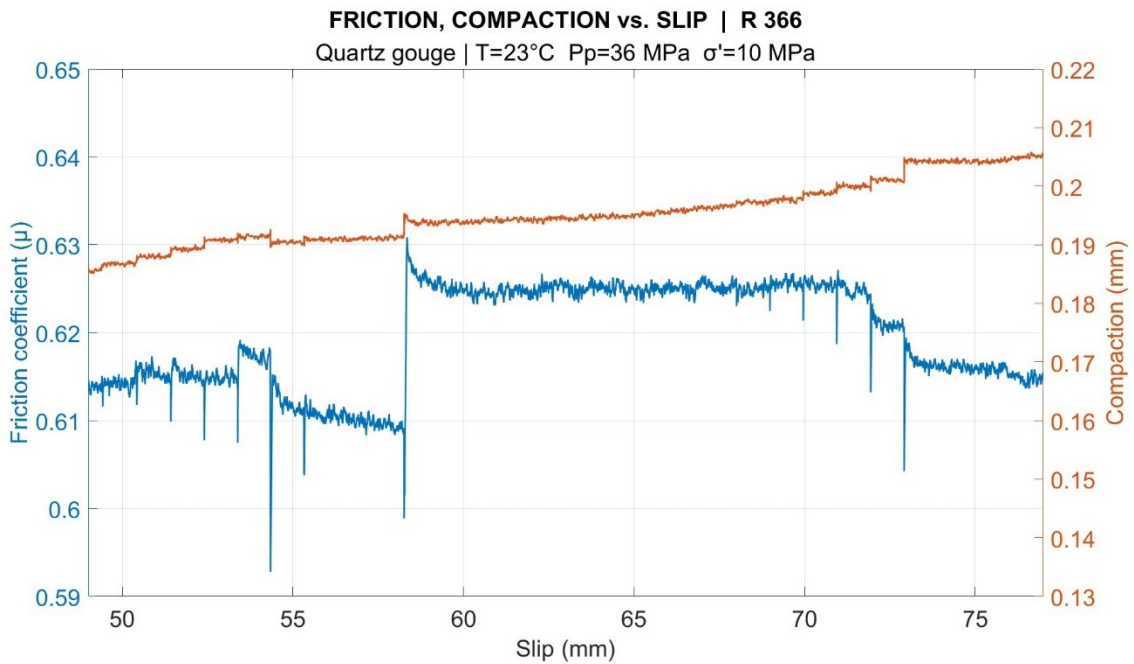


Figure 3.10. Experiment R 366. Zoom on the SHS test. Friction (μ) and compaction (mm) plotted against slip (mm).

Experiment R 383

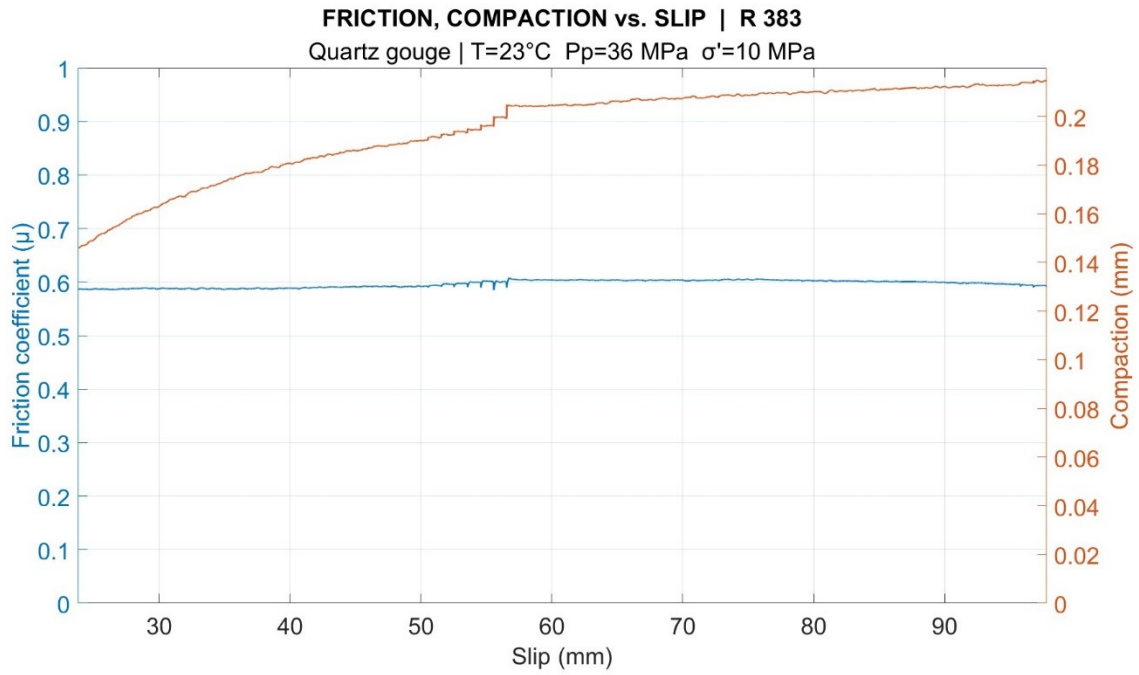


Figure 3.11. General overview of experiment R 383. Friction (μ) and compaction (mm) plotted against slip (mm).

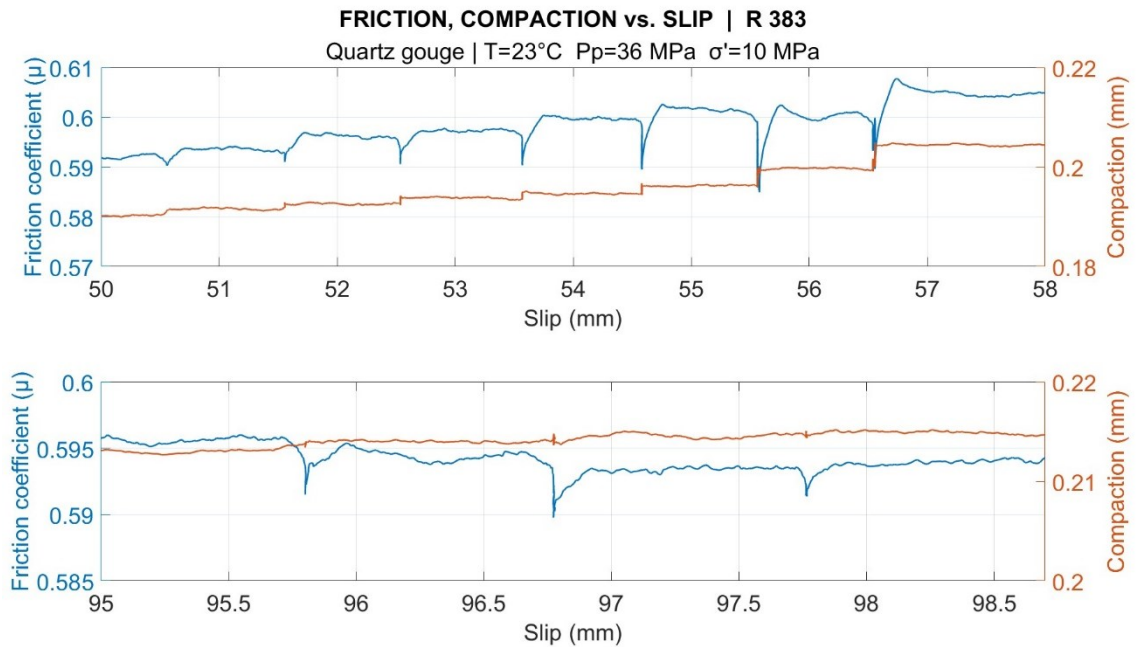


Figure 3.12. Experiment R 383. Zoom on the SHS test. Friction (μ) and compaction (mm) plotted against slip (mm).

Experiment R 368

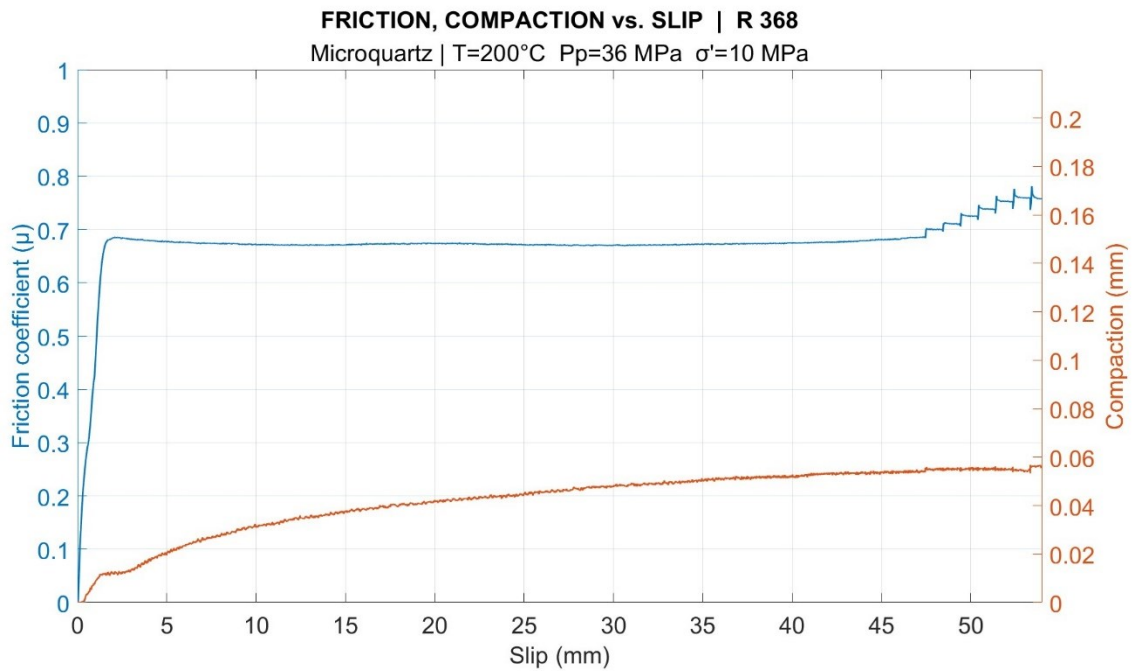


Figure 3.13. General overview of experiment R 368. Friction (μ) and compaction (mm) plotted against slip (mm).

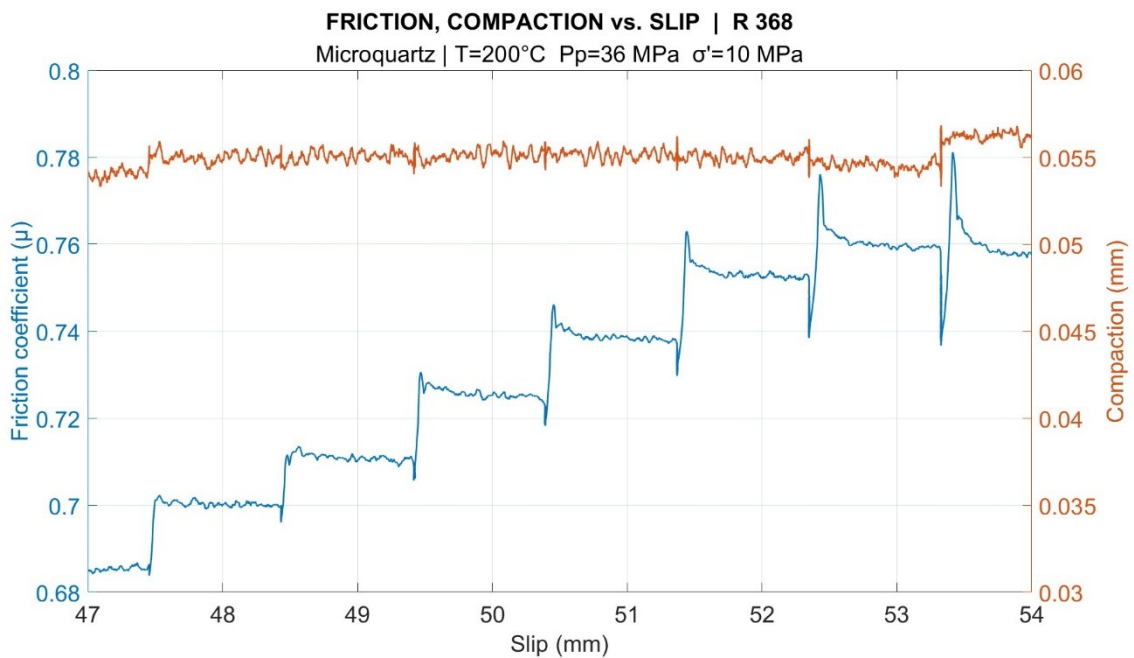


Figure 3.14. Experiment R 368. Zoom on the SHS test. Friction (μ) and compaction (mm) plotted against slip (mm).

Experiment R 370

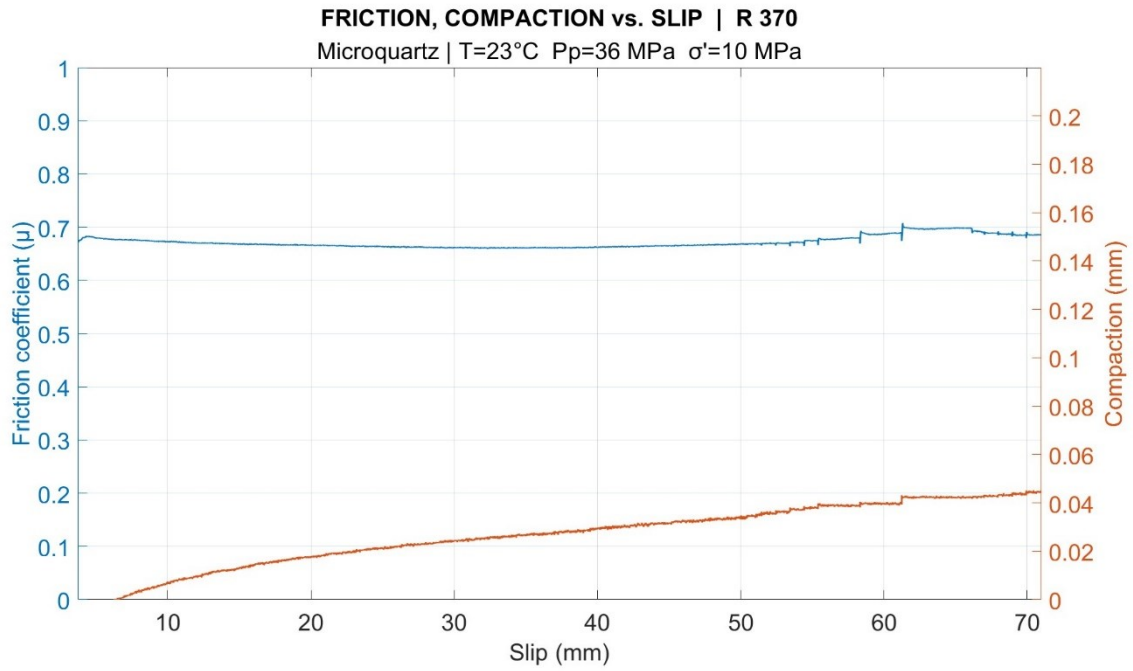


Figure 3.15. General overview of experiment R 370. Friction (μ) and compaction (mm) plotted against slip (mm).

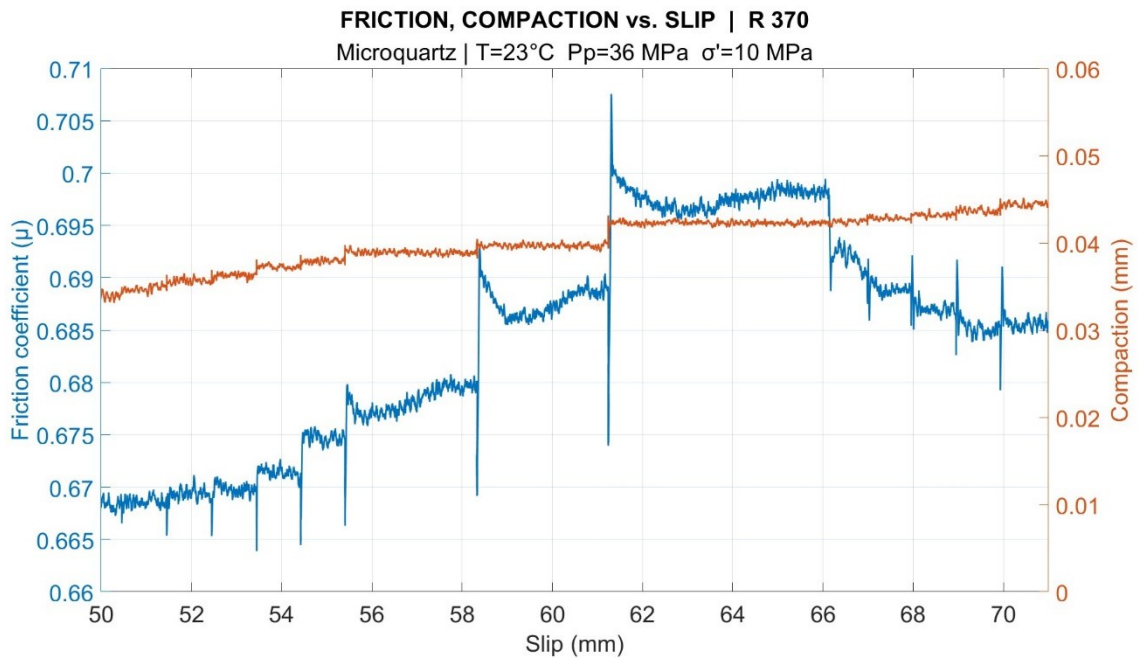


Figure 3.16. Experiment R 370. Zoom on the SHS test. Friction (μ) and compaction (mm) plotted against slip (mm).

Experiment R 372

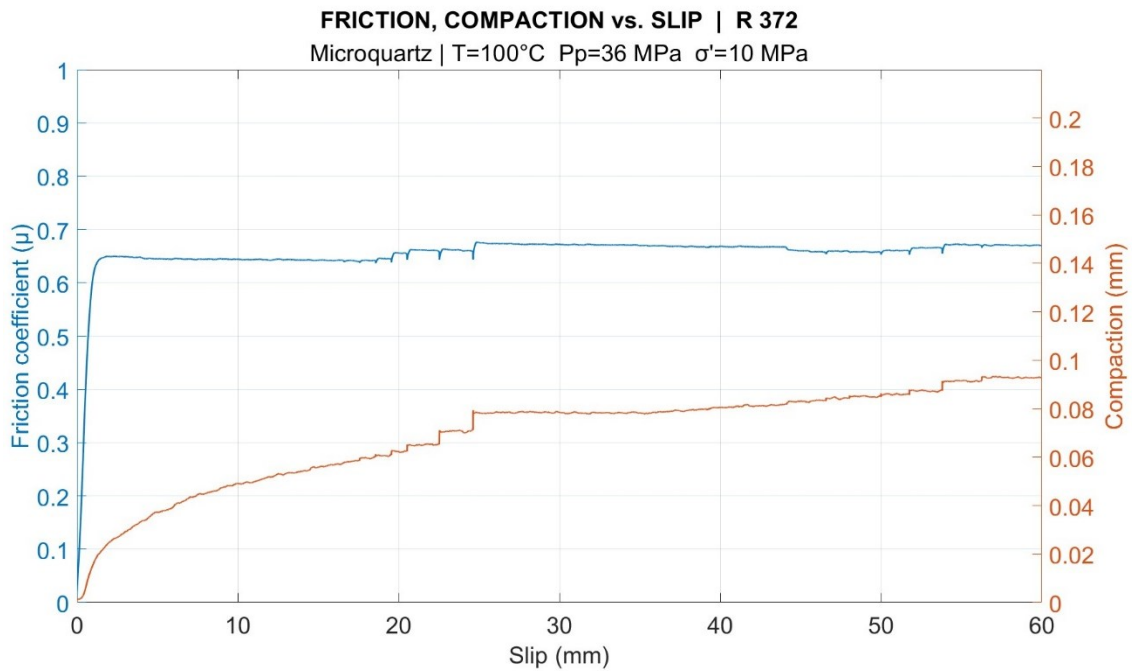


Figure 3.17. General overview of experiment R 372. Friction (μ) and compaction (mm) plotted against slip (mm).

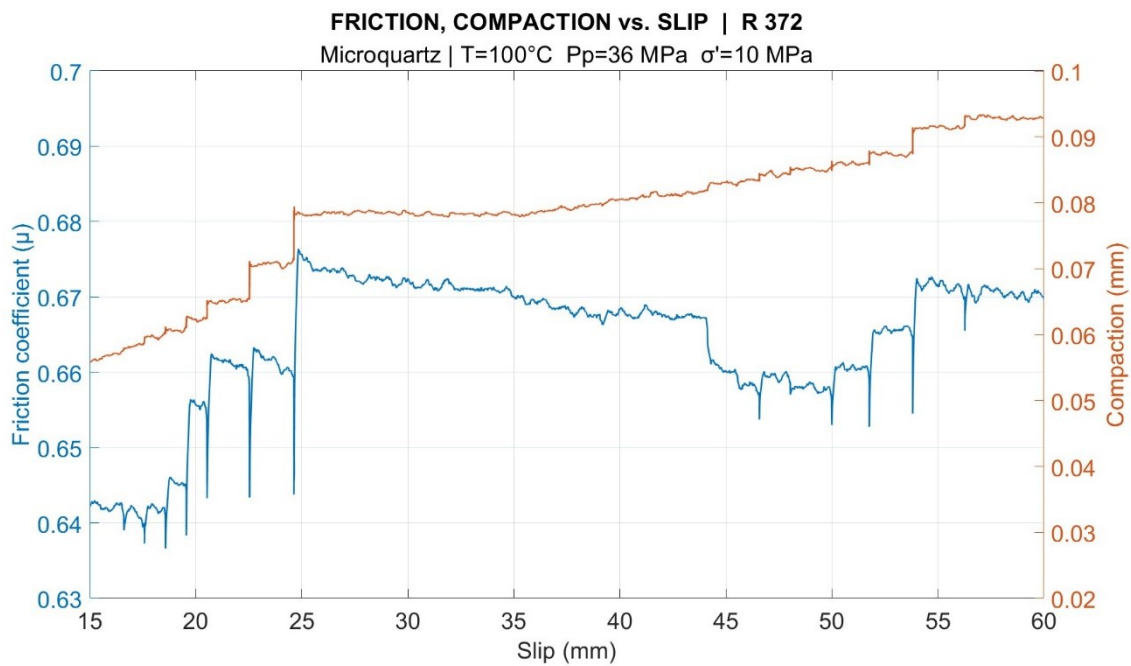


Figure 3.18. Experiment R 372. Zoom on the SHS test. Friction (μ) and compaction (mm) plotted against slip (mm).

Experiment R 374

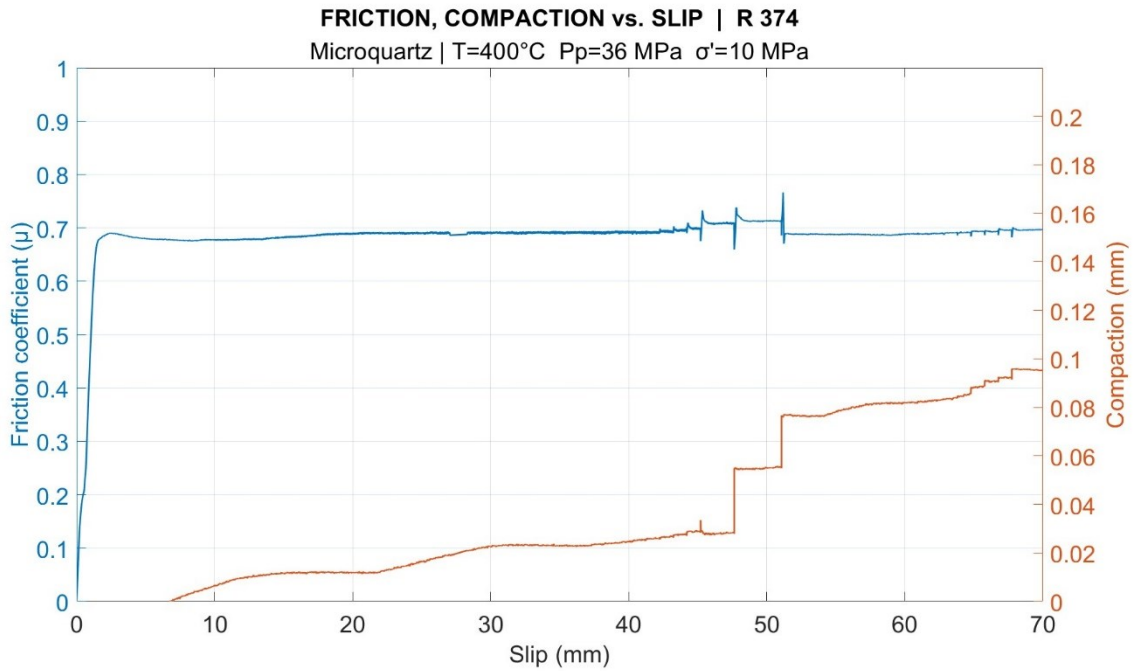


Figure 3.19. General overview of experiment R 374. Friction (μ) and compaction (mm) plotted against slip (mm).

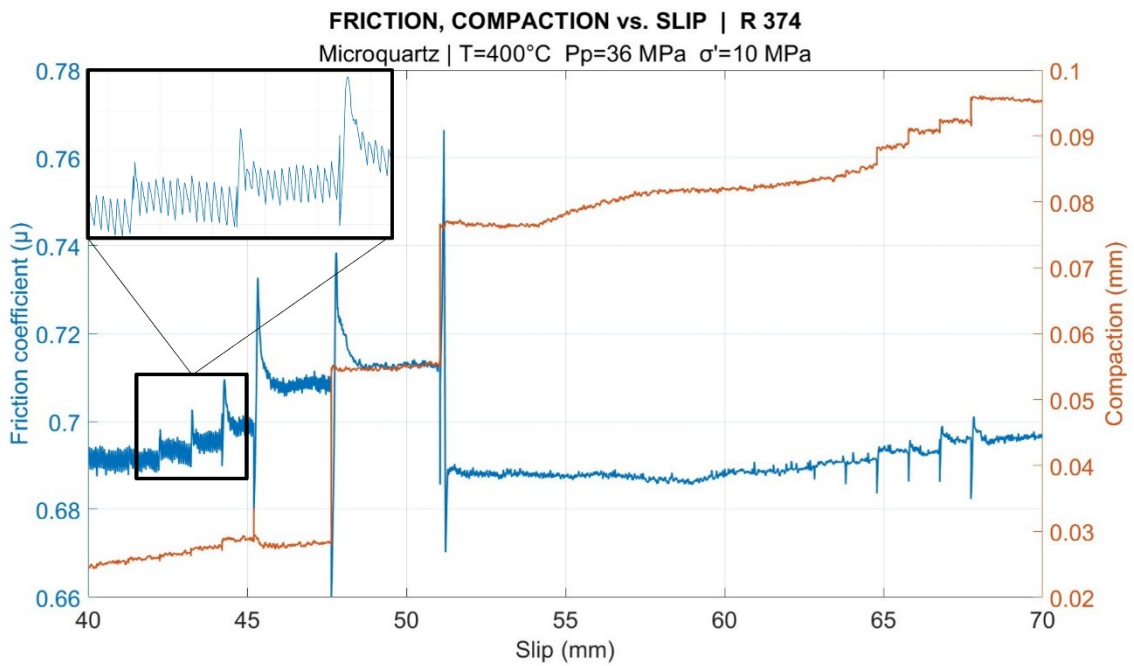


Figure 3.20. Experiment R 374. Zoom on the SHS test. Friction (μ) and compaction (mm) plotted against slip (mm). The inset shows stick-slip behavior during the first SHS test.

3.2 Description of mechanical data

Experiment R 356

Experiment R 356 was the first to be performed, the only one with sample thickness over 1.6 mm (3.5 mm precisely) and with sample weight over 1.5 g (3.4 g precisely). It is noted that the steady state shear strength $\mu \sim 0.64 \pm 0.001$ was attained long before compaction stabilized, between 16 and 17 mm slip.

Looking at the shear strength of the gouge along the whole experiment, it seems that the SHS test did not affect too much the mechanical behavior of the sample, which showed quite constant frictional strength at $\mu \sim 0.64 \pm 0.001$.

Focusing on the SHS test performed from 24 to 29 mm slip, it is noted that the sample did not gain almost any shear strength during hold times, maintaining $\mu \sim 0.64 \pm 0.001$ for the entire test. Compaction values increased constantly until the last hold-slide event, when the sample dilated.

During the SHS series, the gouge compacted of 0.012 mm, i.e. 7.2% of the total compaction.

Experiment R 359

Experiment R 359 was performed in the same conditions as experiment R 356, changing only pore fluid pressure and effective normal stress. In experiment R 356 the ratio P_p / σ_n' was 3.6, while in experiment R 359 the ratio P_p / σ_n' was 0.3.

The plot (Figure 3.3) starts at a slip value of 5 mm due to issues with the angle measurements provided by the apparatus. Fortunately, this happened during the initial run-in phase and not during a SHS series.

Also in this case the sample was still slightly compacting when the SHS test started, while the frictional behavior had already reached its steady state at $\mu \sim 0.66 \pm 0.0018$, after 10 mm slip from the start of the experiment.

Looking at the SHS test, it's noted how the sample gained and then lost less than $\Delta\mu = 0.01 \pm 0.0026$. Compaction values increased until 24 mm slip and then decreased until

27.6 mm slip, to then regain the compaction reached before during a single hold-slide event (1000 s hold). While μ_{ss} was the same before and after the SHS test, during the series the gouge compacted of 0.006 m, corresponding to 4.7% of the total compaction.

Experiment R 361

Also in this experiment, as in the experiments R 356 and R 359, it seems that the sample was still compacting when the SHS test started. Frictional steady state was reached after 9 mm slip and maintained constant through all the experiment at $\mu \sim 0.65 \pm 0.0014$.

Focusing on the SHS test, it doesn't show a regular behavior: the first 10 s hold-slide event produced a weakening of the sample, followed by a huge hardening in correspondence of the 3500 s hold-slide event.

Subsequent hold-slide events produce both weakening and hardening behaviors, showing a not defined trend. Compaction seems to increase with increasing hold time.

During the SHS series, the gouge compacted of 0.006 mm, corresponding to 3.8% of the total compaction.

Experiment R 364

Experiment R 364 was the first to experience a double SHS series, to show the dependence on the shear strain of the mechanical behavior of the gouge. This is one of the two cases (the other is experiment R 374) in which circulating water is under supercritical conditions. It's clearly noticeable that despite the long run-in phase (40 mm), when the SHS test started the gouge was still compacting, and friction coefficient was still increasing, so steady state was not reached at all while sliding at $\mu \sim 0.64 \pm 0.002$.

The two straight lines from 50 to 59 mm are due to issues during acquisition of angle data. Fortunately, this occurred during the 10 mm long reshear and not during a SHS test. Looking at the SHS series, the first one produced a strengthening in dynamic shear strength of 16%, while the second one produced a weakening in dynamic shear strength of about 0.007%. So, this is the first case of effective weakening of the experimental fault, i.e., the increase in static friction provided by healing mechanisms is not enough to balance the slip weakening behavior trend of the quartz gouge during a SHS series.

Compaction measurements show an almost constant increase for every hold-slide event, with a particular compaction peak followed by a slight dilation during the slide phases.

During the first SHS test the sample compacted of 0.03 mm, while during the second one it compacted of 0.013 mm, corresponding respectively to 14% and 6% of the total compaction.

Experiment R 366

Experiment R 366 is performed at room temperature (23 °C), to have an end member in terms of effect of temperature on the mechanical behavior of the gouges.

The plot (Figure 3.9) starts at a slip value of 25 mm because of other issues with the angle measurements provided by the apparatus. Analyzing the general trends of the entire experiment, also in this case it is easy to affirm that the first and the second SHS series affect in a different way the gouge, with a general weakening behavior.

Frictional steady state (with a very mild hardening behavior) was reached after 25 mm slip at $\mu \sim 0.61 \pm 0.0017$, while compaction values continued to increase for the whole experiment.

Focusing on the two SHS series, both show a loss of shear strength, quantifiable in 0.008% during the first series and 0.016% during the second one.

The sample compacted quite constantly during both the first and the second SHS series, except for the dilation showed during the hold-slide event of 22500 s hold.

During the first SHS test the gouge compacted of 0.01 mm as in the second test, producing in each case the 4.8% of the total compaction.

Experiment R 383

Experiment R 383 was originally performed to have a comparison with experiment R 366. In fact, P-T conditions are identical to the latter. As in experiment R 366, the plot (Figure 3.11) starts at a slip value of 25 mm because we managed to reproduce precedent issues coming from angle measurements by the apparatus.

Frictional steady state was reached after 23 mm slip at $\mu \sim 0.59 \pm 0.002$, while compaction values were increasing before, during and after the SHS tests performed.

Since the two SHS tests are separated by 38 mm of slip, I subdivided them in two different plots. The first SHS series shows a quite constant increase in static and dynamic friction, highlighting a 2.2% increase in shear strength, with respect to when the SHS test started. In addition, the sample compacted of 0.015 mm, corresponding to the 6.9% of total compaction.

The same is not true for the second SHS series, that showed a weakening behavior, decreasing the shear strength of the gouge of 0.3%. On the other hand, during the second SHS test the sample compacted of 0.0013 mm, corresponding to the 0.68% of the total compaction.

Experiment R 368

Experiment R 368 is the first performed on microquartz.

Frictional steady state was reached after 10 mm slip at $\mu \sim 0.68 \pm 0.0013$, while when the SHS test started, the sample was sliding at constant value of 50 μm of compaction.

The single SHS test shows a huge hardening behavior. For every hold-slide event, the sample was able to maintain from 50 to 100% of the shear strength gained during hold times, resulting in an always harder sample to slide.

Despite this strong frictional trend, compaction values seem to remain constant through all the test, except for the slight dilation during the 3000 s hold-slide event and the slight compaction during the 10000 s hold-slide last event.

During the SHS test the sample compacted of 0.003 mm, corresponding to 5.2% of the total compaction.

Experiment R 370

Experiment R 370 shows two distinct mechanical behaviors in function of the two distinct SHS series.

Frictional steady state was reached after 20 mm slip, at $\mu \sim 0.67 \pm 0.001$, while in this case the sample was still compacting when the SHS test began.

In the case of SHS tests performed during experiment R 370, it's the first time that it's possible to see this particular behavior: from 3000 s hold-slide event, at every reshear, the sample gained a certain shear strength value, to then weaken (as in previous cases) and subsequently regain part of the lost strength.

For example, in the case of 10000 s hold-slide event, the gouge gained 0.024% in shear strength when it restarts sliding. Then, after 0.8 mm it lost 0.011% of the strength and in the end it regained 0.004% during the last slip stage.

If the first SHS series produced a huge hardening ($\Delta\mu = 0.039 \pm 0.0011$ with respect to the start of the SHS test, until 56000 s hold-slide event), the second one left the sample weaker than before ($\Delta\mu = - 0.013 \pm 0.0011$, with respect to the start of the second SHS test, until the end of the experiment), but still stronger than its original steady state.

During the first SHS test the sample compacted of 0.008 mm, while during the second one it compacted of 0.002 mm, corresponding respectively to 17% and 4.4% of the general compaction.

Experiment R 372

Experiment R 372 was performed conducting the two SHS tests with the most shear displacement range between them, of 20mm.

Frictional steady state was reached after 8 mm slip at $\mu \sim 0.65 \pm 0.0005$, while compaction increased throughout the experiment.

Both the first and the second SHS series show strong hardening and compacting trends. The sample compacted of 25 μm during the first SHS test, and of 14 μm during the last one. In this case, it seems that after each hold-slide event, the gouge did not show a clear friction peak followed by a friction drop as in other experiments, but a quasi-steady state with a soft weakening behavior. However, the simple sliding of the sample (i.e. from 25 to 43 mm slip) produced a constant weakening.

During the first SHS series the sample gained $\sim 5\%$ of shear strength and compacted of 0.023 mm (24.7%), while during the second one it gained $\sim 1.5\%$ of shear strength and compacted of 0.013 mm (13.9%).

Experiment R 374

Experiment R 374 is the one of the second series in which the sample compacted the most (0.1 mm). Frictional steady state was reached after 20 mm slip, at $\mu \sim 0.69 \pm 0.0014$.

From 10 mm to about 48 mm of slip, the gouge exhibited a stick-slip behavior, to then evolve to stable sliding.

Compaction doesn't show a clear trend, as the gouge seems to oscillate between compacting and dilating until the first SHS started.

Focusing on the two SHS series, it's clearly noticeable a different mechanical trend.

During the first test, the sample gained 12% of shear strength with respect to the original steady state, (corresponding to an increase of $\Delta\mu = 0.08 \pm 0.0017$) and compacted of 0.055 mm, corresponding to the 58% of its total compaction value. The second SHS test did not produce such results, gaining only 0.11% in shear strength and compacting only for the 19% with respect to the total compaction during the experiment.

3.3 Mechanical comparison between experiments

The next figures will show the effect of the temperature, grain size and shear strain on the mechanical behavior of each experiment, displaying several comparisons in terms of friction coefficient (μ), compaction (mm), healing ($\Delta\mu$) and healing rate (β).

The abbreviation “*hs*” in some plot’s legend stays for “*high stress*” and means that experiment was performed under an effective normal stress $\sigma_n' = 20$ MPa and pore fluid pressure $P_p = 6$ MPa, with respect to all other experiments performed with $\sigma_n' = 10$ MPa and $P_p = 36$ MPa. Where not otherwise reported, healing data always refer to the first SHS test.

3.3.1 The effect of temperature

Experiments performed on F110 heterometric angular quartz

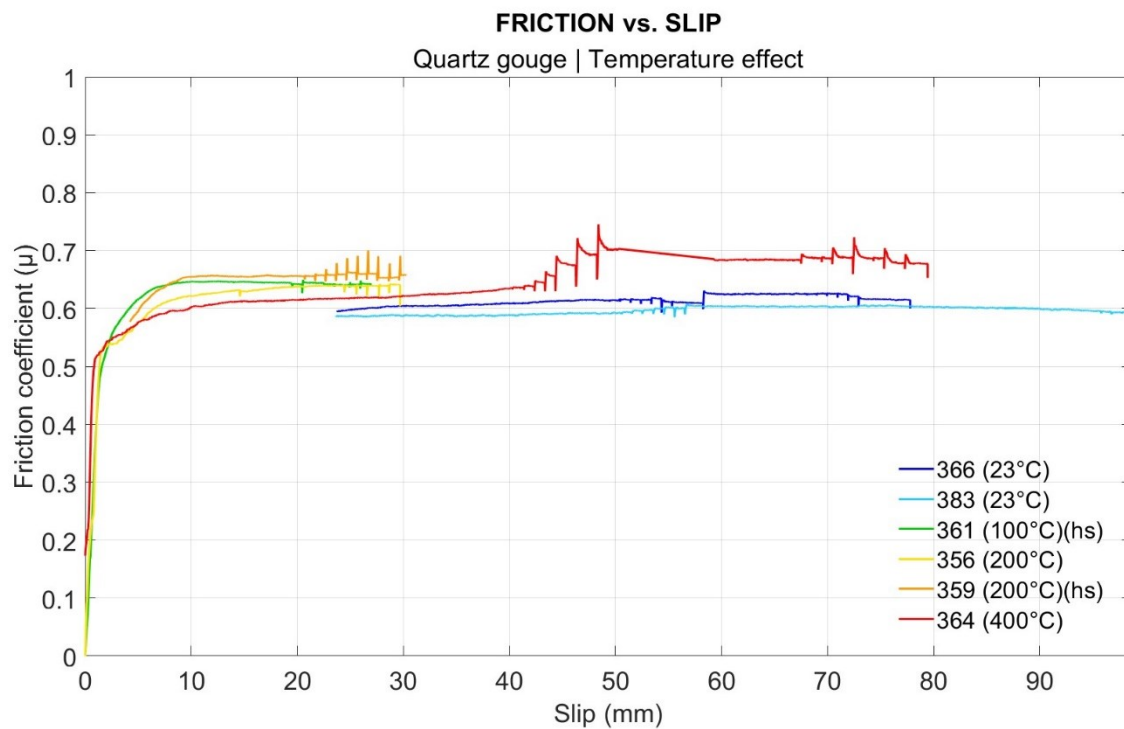


Figure 3.21. Comparison between experiments performed on F110 heterometric angular quartz. Friction (μ) plotted against slip (mm).

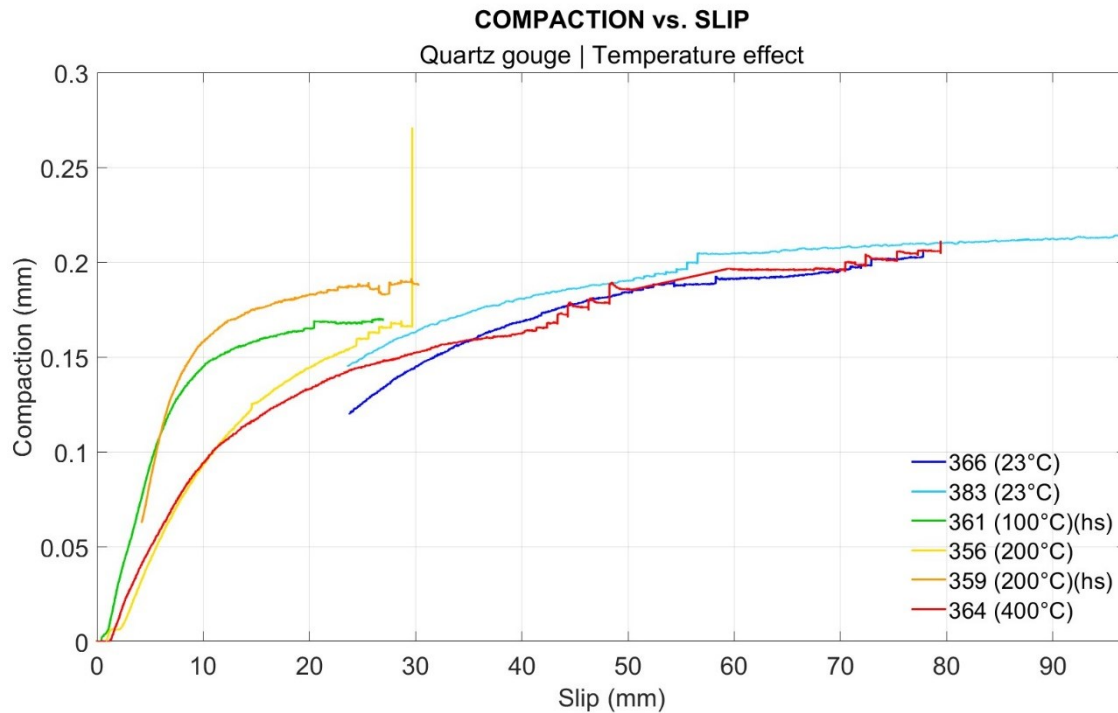


Figure 3.22. Comparison between experiments performed on F110 heterometric angular quartz. Compaction (mm) plotted against slip (mm).

The comparison between the experiments performed on F110 heterometric angular quartz (Figure 3.21), shows that there is not a clear temperature dependence of dynamic friction. Basically, experiments R 383 (and R 366, both performed at room temperature) and experiment R 364 (performed at 400 °C) are the end members in terms of sliding friction, but there is not a clear distinction between the other three experiments.

It's noticeable that experiment R 359 (200 °C, high stress) shows higher friction values than experiment R 356 (200 °C, low stress), suggesting a small but noticeable direct effective stress dependence of friction. The largest influence of temperature is appreciable looking at the friction peaks and friction drops, as experiment R 364 exhibits the highest shear strength buildups and friction, while experiment R 366 the lowest ones.

The abrupt variation in compaction at the end of experiment R 356 is due to the removal of the sample from the machine while still recording.

Compaction values and trends of experiments performed on F110 heterometric angular quartz (Figure 3.22) look almost identical, apart from the initial larger compaction in angular quartz samples. The major temperature effect showed by this plot is, once again, the large vertical displacement drops of experiment R 364, the one performed at 400 °C, that however follows in his way the compaction trends of other experiments.

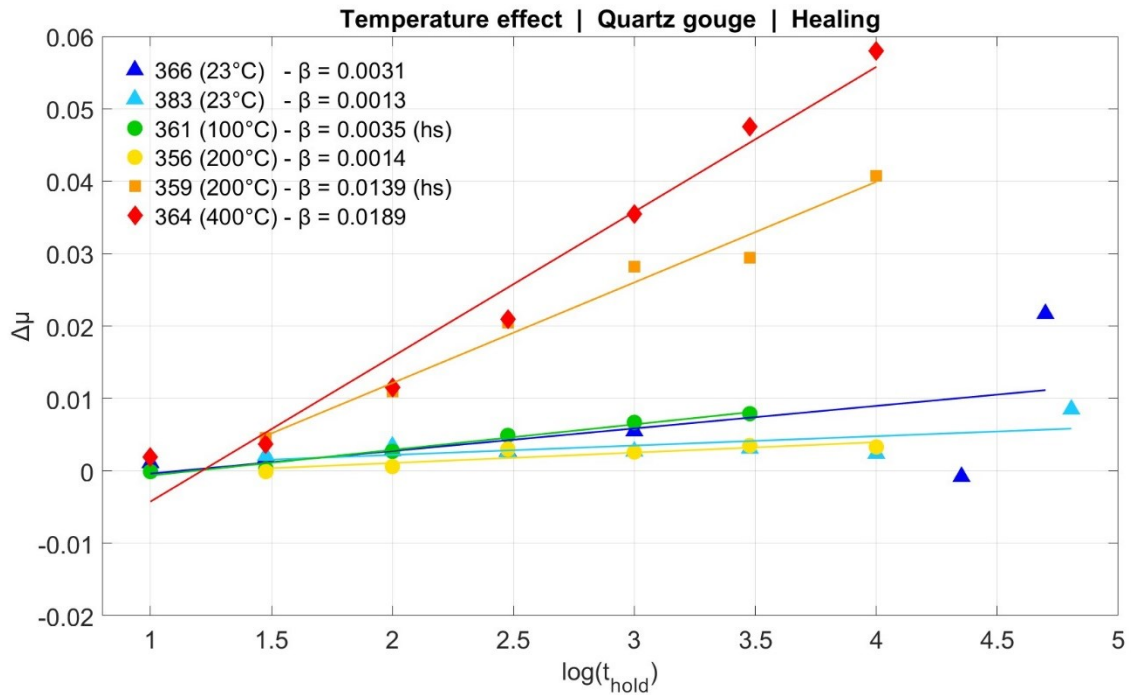


Figure 3.23. Comparison between healing data of experiments performed on F110 heterometric angular quartz. $\Delta\mu$ plotted against $\log(t_{\text{hold}})$. Healing rate parameter (β) is shown in the box.

Focusing on healing and healing rate shown in Figure 3.23, there's a clear temperature dependence of healing ($\Delta\mu$) and healing rate parameter (β). The higher the temperature, the higher the shear strength gained during stationary contact periods, but also the rate of increase of the shear strength (β). This is particularly noticeable for end members experiments (R 366, R 383 and R 364) in terms of temperature.

It seems also that the increase in effective normal stress (represented by experiment R 359) causes an increase in frictional healing, both magnitude and rate.

Experiments performed on microquartz

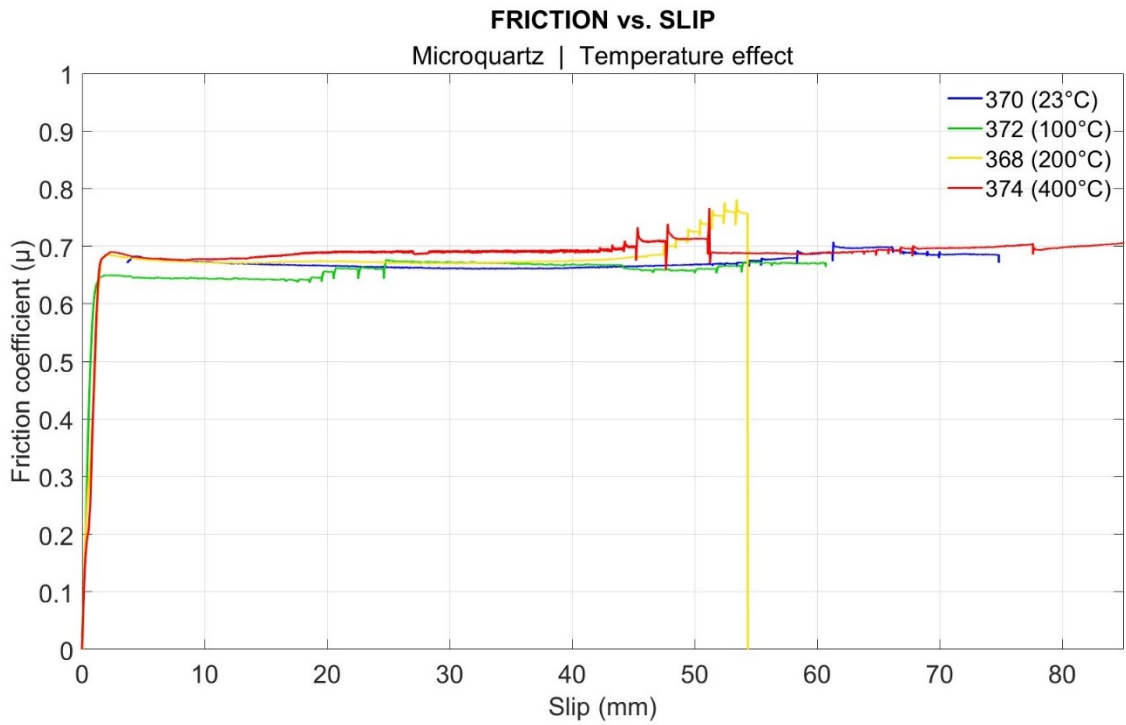


Figure 3.24. Comparison between experiments performed on microquartz. Friction (μ) plotted against slip (mm).

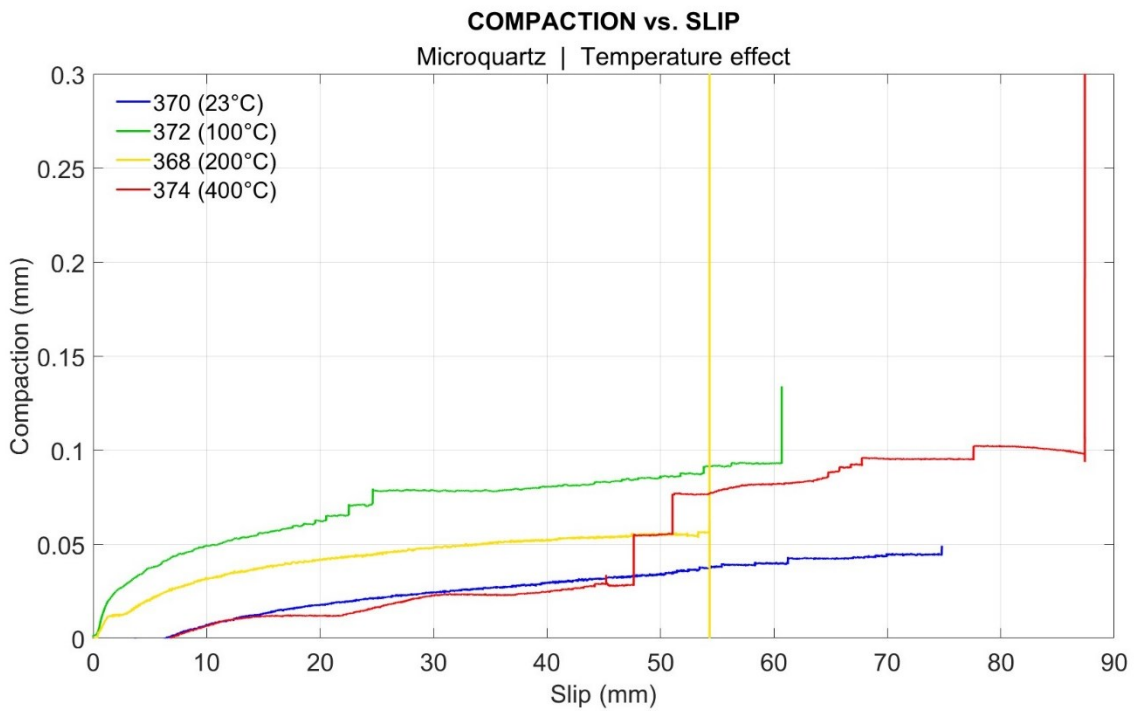


Figure 3.25. Comparison between experiments performed on microquartz. Compaction (mm) plotted against slip (mm).

Focusing on the comparison between the experiments performed on microquartz (Figure 3.24), the same trends mentioned for angular quartz can be noted. Also in this case, end members in terms of friction coefficient are almost identical.

The same reasoning can be done looking at compaction values of experiments performed on microquartz (Figure 3.25), which exhibit similar trends, but shifted down of about 0.1 mm. The largest vertical displacement drops are shown by the data of experiment R 374, the one performed at 400 °C. The other experiments show almost the same trends. The abrupt variation at the end of experiments R 368, R 72 and R 374 is due to the removal of the sample from the apparatus while still recording.

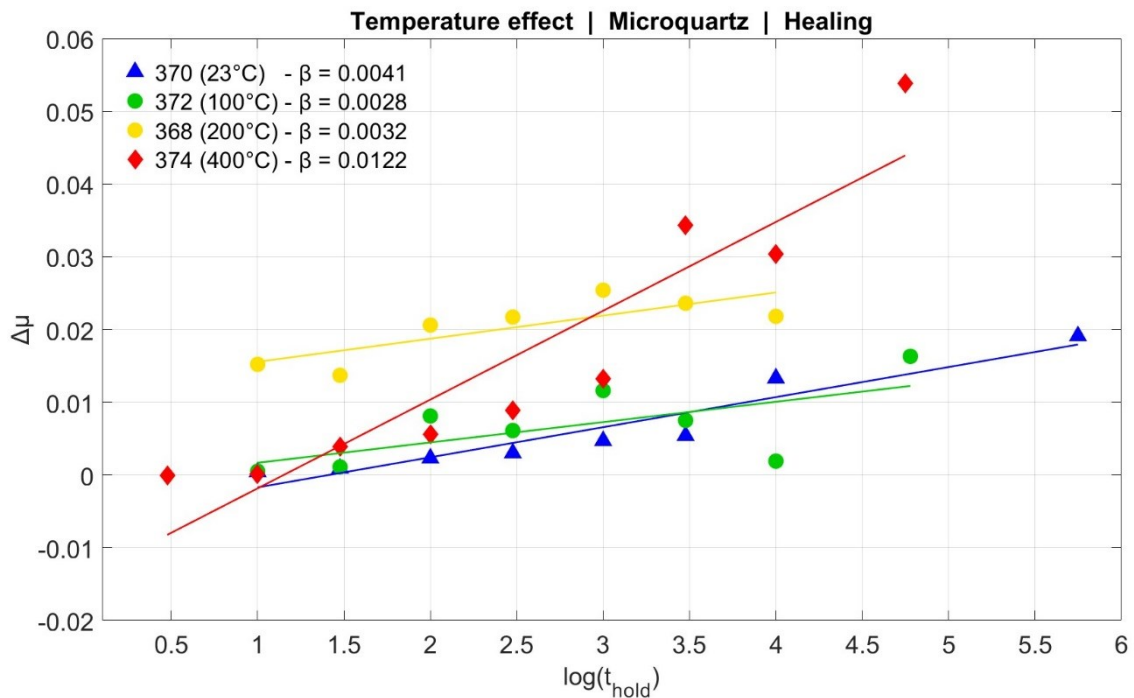


Figure 3.26. Comparison between healing data of experiments performed on microquartz. $\Delta\mu$ plotted against $\log(t_{\text{hold}})$. Healing rate parameter (β) is shown in the box.

Healing ($\Delta\mu$) and healing rate (β) measured on microquartz samples (Figure 3.26) show a positive temperature dependence of the magnitude and rate of healing. It is interesting to note how experiments R 372, R 368 and R 374 display a $\Delta\mu$ drop corresponding to a hold time of 3000 s.

3.3.2 The effect of grain size

Another major goal of this work was to determine whether the mechanical properties of the gouges were affected by the difference in grain size. The next plots show a comparison between experiments performed at the same temperature but on different grain size (F110 heterometric angular quartz, < 110 μm vs. microquartz, < 5 μm). Also in this case, the plots showing healing data are relative to the first SHS series.

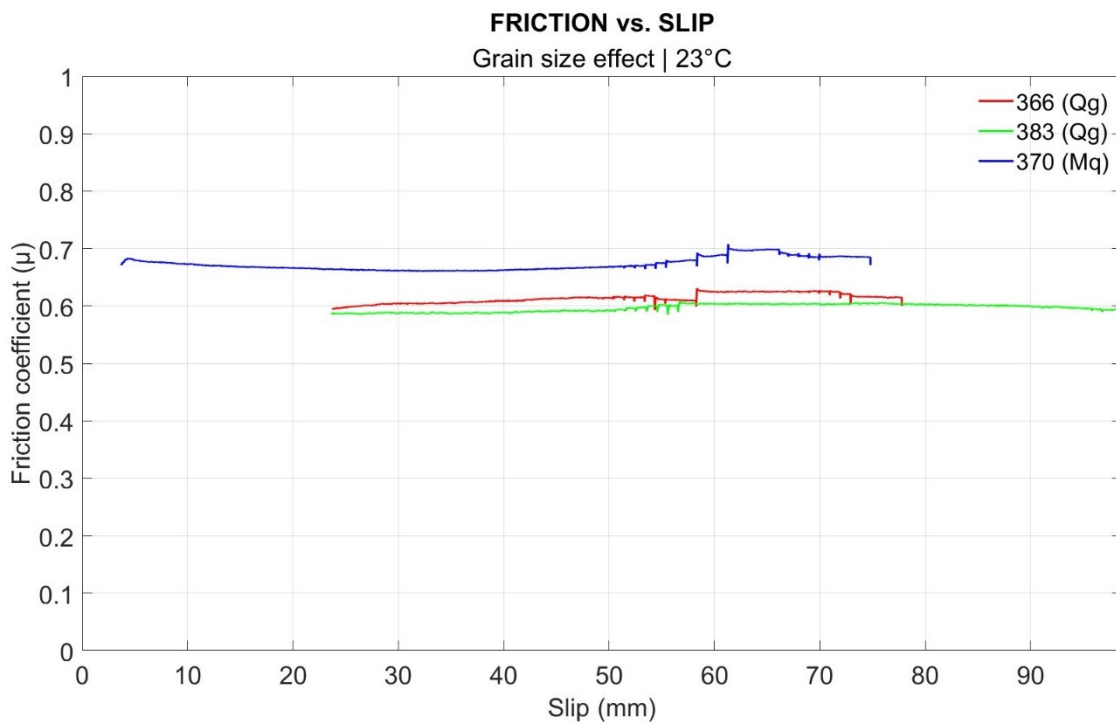


Figure 3.27. Comparison between experiments performed at 23 °C (room temperature). Friction (μ) plotted against slip (mm).

Looking at the comparison between experiments performed at 23 °C it is noticeable a clear grain size dependence of the steady state friction μ_{ss} . While experiments performed on angular quartz show $\mu_{ss} \sim 0.6$, the experiment performed on microquartz exhibits $\mu_{ss} \sim 0.67$. This different shear strength is maintained throughout the experiment.

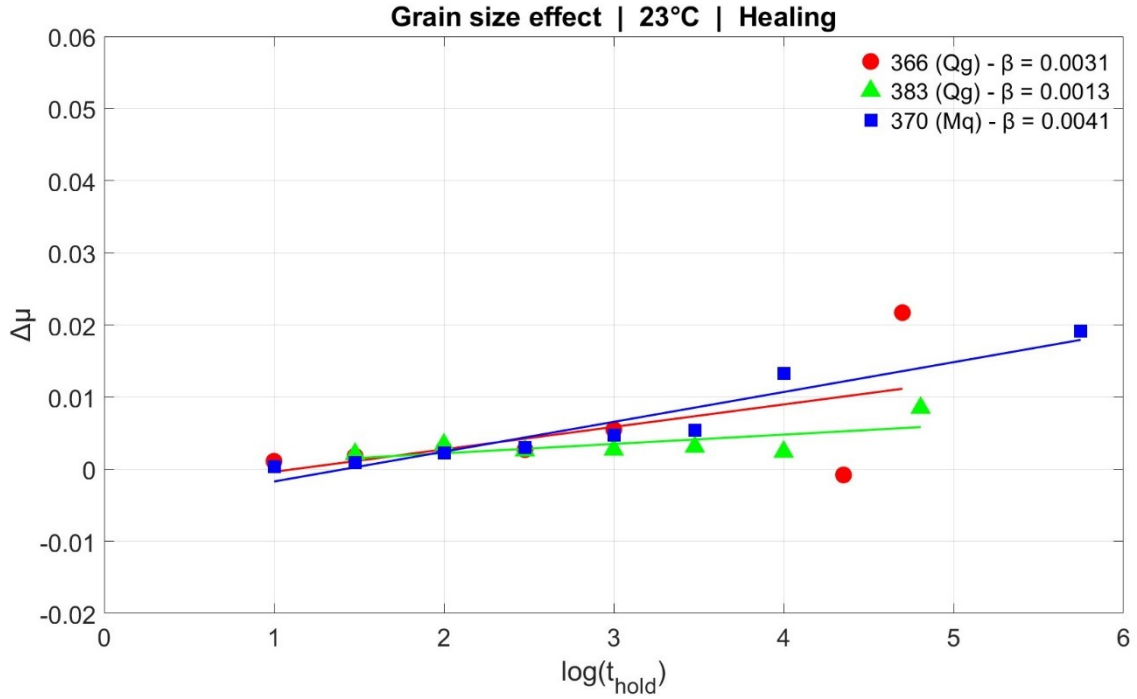


Figure 3.28. Comparison between experiments performed at 23 °C (room temperature). $\Delta\mu$ plotted against $\log(t_{\text{hold}})$. Healing rate parameter (β) is shown in the box.

Healing magnitude ($\Delta\mu$) measurements do not appear to be systematically affected by the difference in grain size at 23 °C. Healing rate (β) data suggest a minor influence of grain size on this parameter, since for angular quartz $\beta = 0.0012$ and $\beta = 0.0031$, while for microquartz $\beta = 0.0041$.

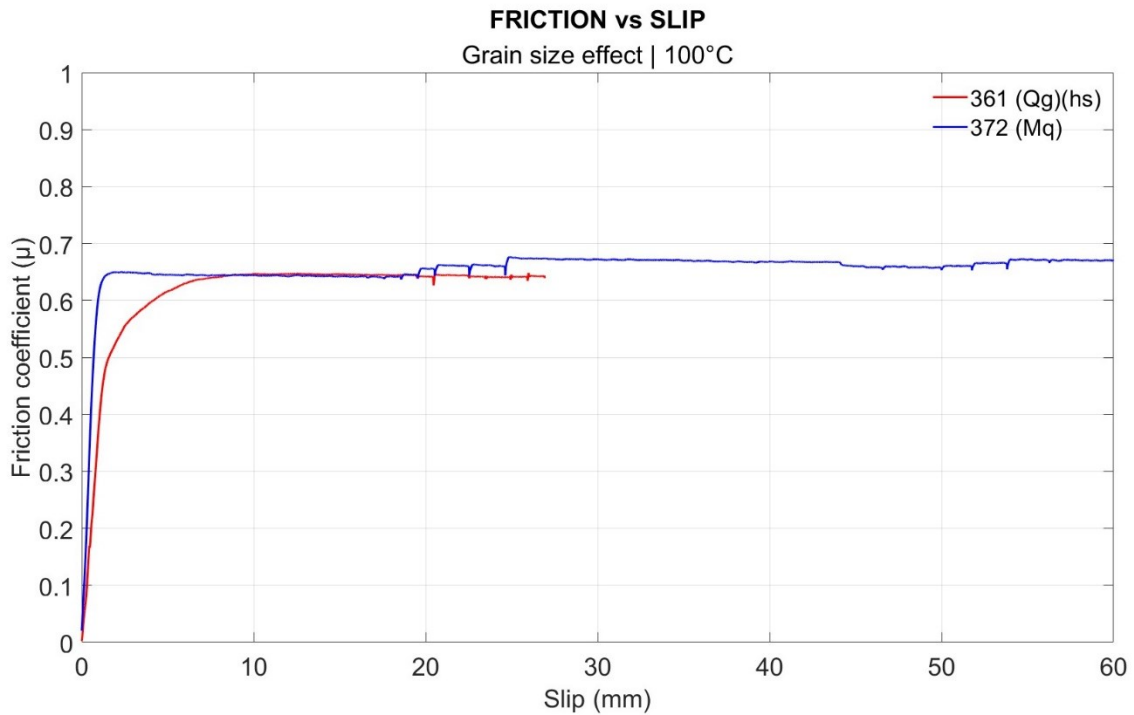


Figure 3.29. Comparison between experiments performed at 100 °C. Friction (μ) plotted against slip (mm).

In this case, apart from the first 4-5 mm of slip, where the microquartz sample reached the steady state $\mu_{ss} \sim 0.65$ long before the angular quartz sample, there is almost no difference between the frictional steady states. However, the comparison is not totally consistent since experiment R 361 was performed under higher effective normal stress conditions ($\sigma_n' = 20$ MPa with respect to $\sigma_n' = 10$ MPa). As in the case of experiments R 356 and R 359, this different effective stress could affect mechanical behavior of the gouge by increasing its steady state shear strength reached the steady state μ_{ss} .

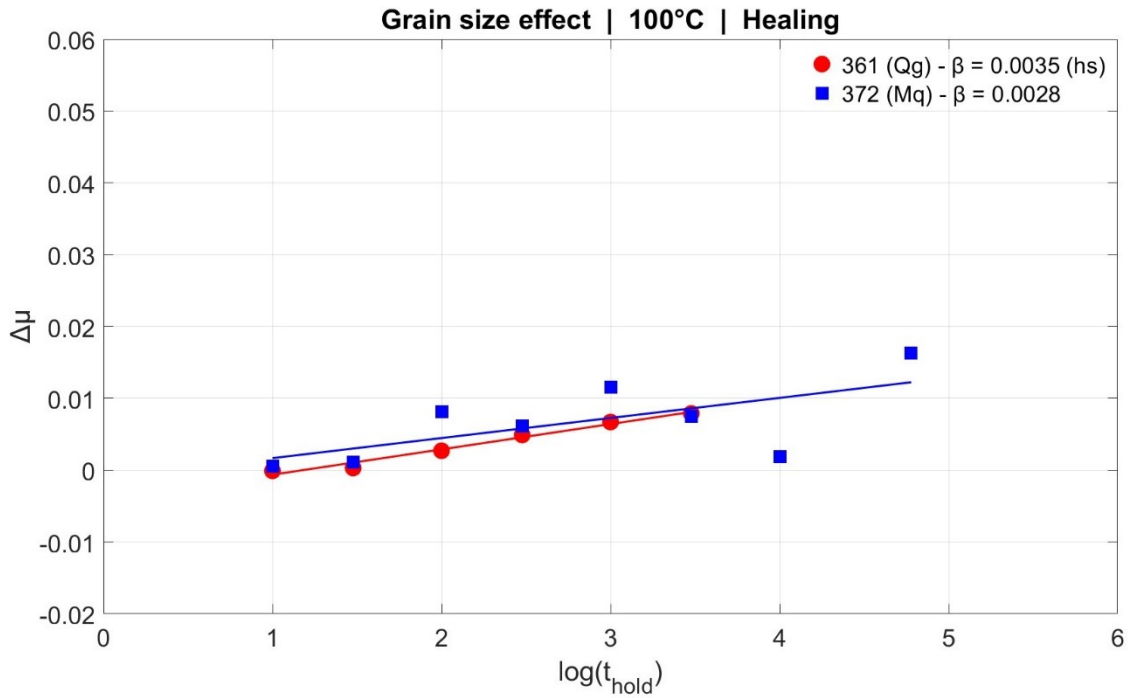


Figure 3.30. Comparison between experiments performed at 100 °C. $\Delta\mu$ plotted against $\log(t_{\text{hold}})$. Healing rate parameter (β) is shown in the box.

Also at a temperature of 100 °C both healing magnitude and rate are not systematically different. $\Delta\mu$ values are generally higher in measurements relative to microquartz, but the large fluctuation of these data makes it difficult to state whether this is a systematic effect. The healing rate (β) measured on angular quartz sample appears to be slightly higher than the one measured on microquartz sample, but again this could be related to the different effective normal stress applied during these experiments ($\sigma_n' = 20$ MPa in experiment R 361).

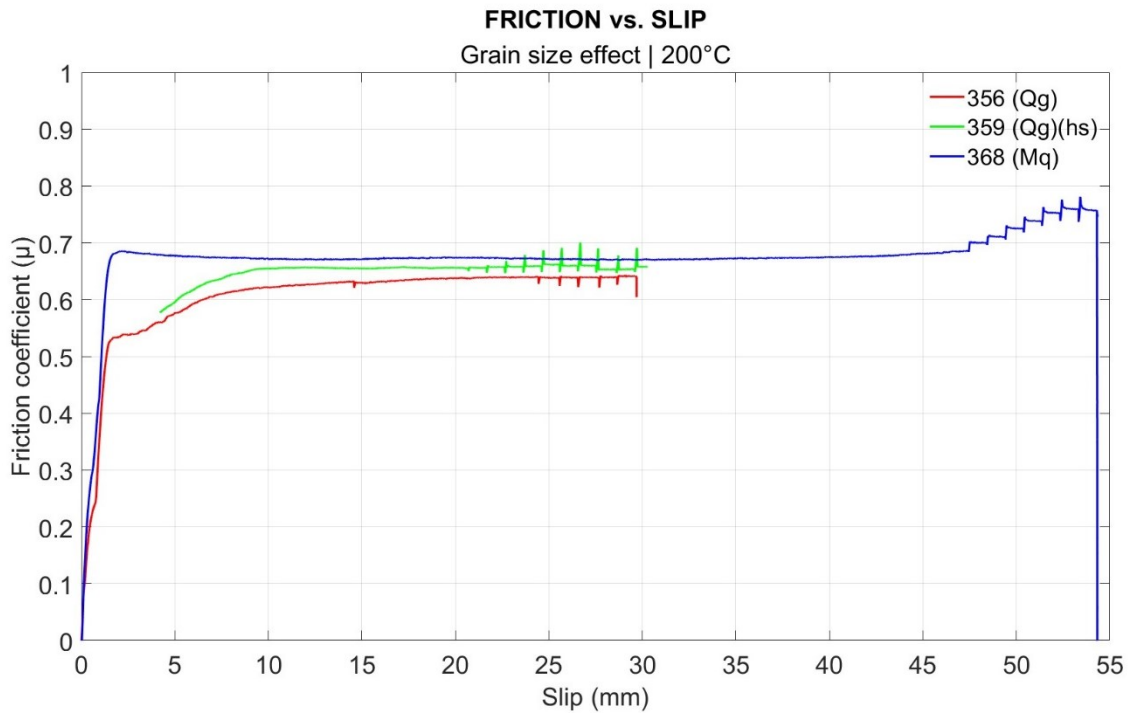


Figure 3.31. Comparison between experiments performed at 200 °C. Friction (μ) plotted against slip (mm).

Looking at the comparison between experiments performed at 200 °C it is confirmed what was observed in previous cases: the experiment performed on microquartz shows a steady state $\mu_{ss} \sim 0.68$, the experiment performed on angular quartz at higher effective normal stress ($\sigma_n' = 20$ MPa) shows a steady state $\mu_{ss} \sim 0.66$ while the experiment performed on angular quartz at lower effective normal stress shows a steady state $\mu_{ss} \sim 0.64$. Also in this case the microquartz gouge achieved the frictional steady state long before the angular quartz gouge, by reaching a yield point after ~ 2 -3 mm of slip.

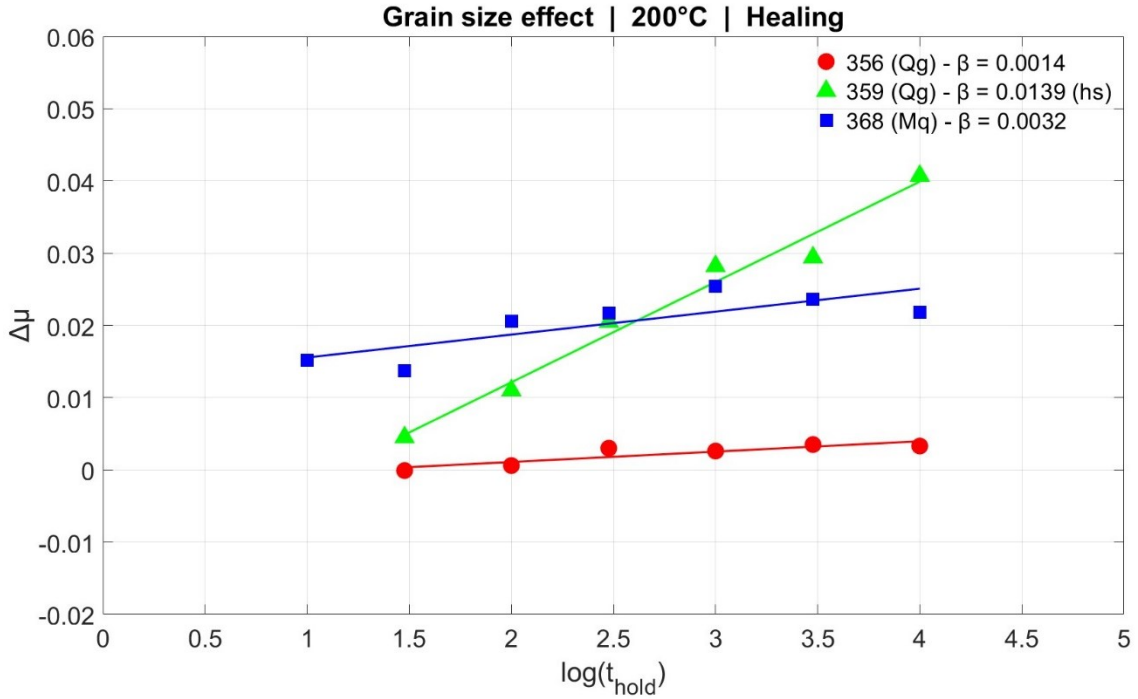
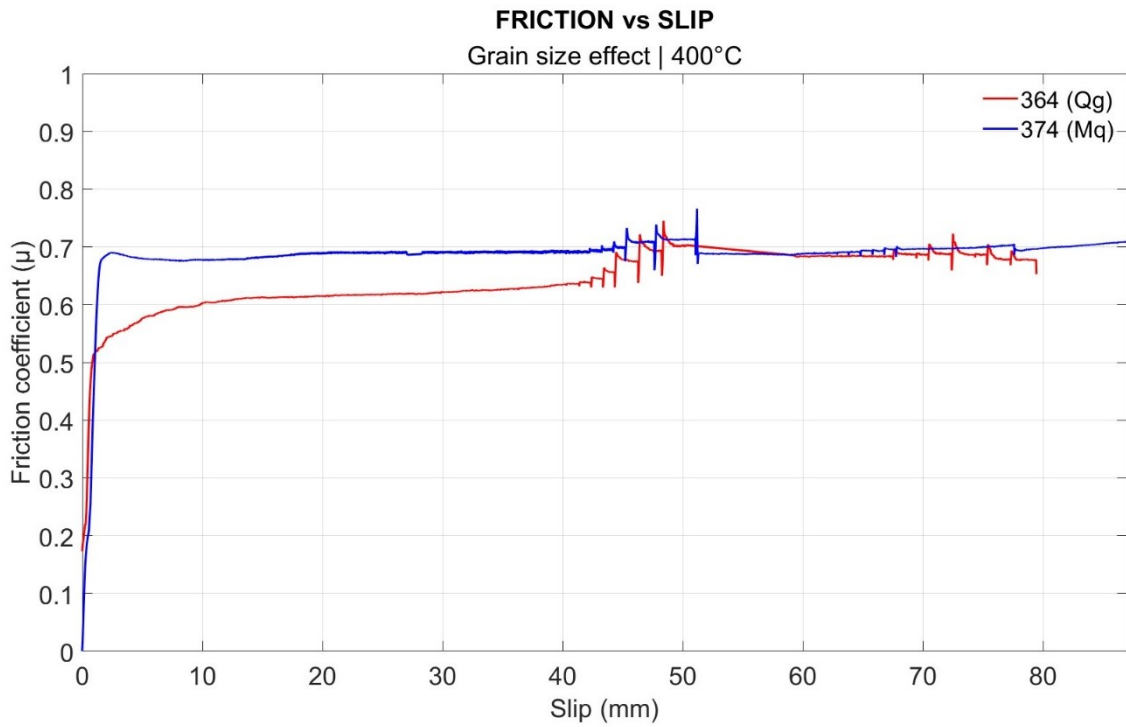


Figure 3.32. Comparison between experiments performed at 200 °C. $\Delta\mu$ plotted against $\log(t_{hold})$. Healing rate parameter (β) is shown in the box.

In the case of experiments performed at 200 °C, healing magnitude ($\Delta\mu$) values measured on microquartz are remarkably higher than those measured on angular quartz. Despite that, the healing rate (β) of experiment R 368 (microquartz) is not much higher than that of experiment R 356 (angular quartz). A totally different observation regards experiment R 359, which shows the highest healing rate value, indicating again of the higher effective normal stress ($\sigma_n' = 20$ MPa) of the experiment affected these measurements, contributing to further strengthen the experimental fault.



*Figure 3.33. Comparison between experiments performed at 400 °C.
Friction (μ) plotted against slip (mm).*

Experiments performed at 400 °C do not represent an exception in terms of grain size effect on the frictional steady state μ_{ss} : experiment R 374, performed on microquartz resulted to slide at $\mu_{ss} \sim 0.69$ while experiment R 364, performed on angular quartz, at $\mu_{ss} \sim 0.64$. This difference seems to disappear after the first SHS test, when both samples show $\mu_{ss} \sim 0.68$. The plot confirms that microquartz samples reach the frictional steady state μ_{ss} before angular quartz samples.

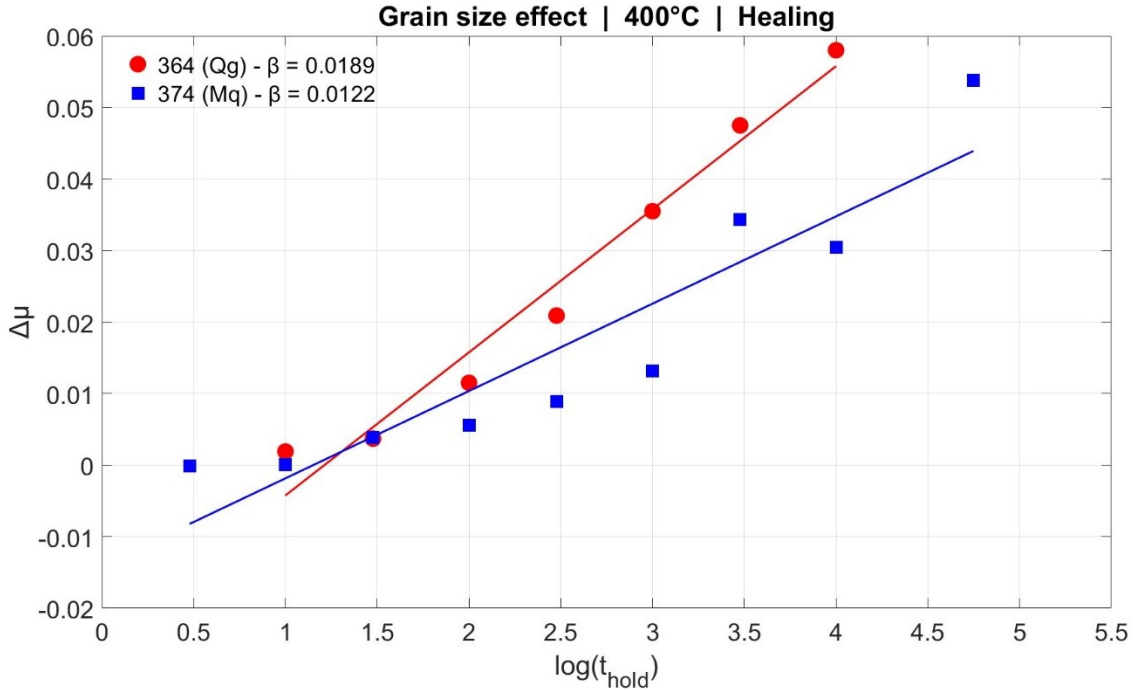


Figure 3.34. Comparison between experiments performed at 400 °C. $\Delta\mu$ plotted against $\log(t_{hold})$. Healing rate parameter (β) is shown in the box.

An important remark, looking at this plot (Figure 3.34), is that healing data ($\Delta\mu$) of experiments performed at 400 °C are not well fitted with a linear regression.

Apart from that, both healing magnitude ($\Delta\mu$) and rate (β) measurements are higher in experiment R 364, performed on angular quartz ($\beta = 0.0189$ vs. $\beta = 0.0122$).

In conclusion, the main observation looking at the mechanical behaviors of the gouges of different grain size (from Figure 3.27 to Figure 3.34) is that microquartz samples show higher dynamic friction levels. Another major observation is that microquartz samples behave in a different way for the first 4-5 mm of slip. In fact, while F110 heterometric angular quartz gouge samples reach gradually their steady state, microquartz samples show a fairly sharp curve with a friction peak, to then weaken until steady state is reached and maintained throughout the experiment.

By observing the plots regarding the magnitudes and the rates of healing with respect to the two different grain sizes, I observe no systematic grain size dependence of these parameters under tested P-T conditions.

3.3.3 The effect of shear strain on healing

In the following plots, I show the differences in healing magnitude ($\Delta\mu$) and rate (β) between the first and second SHS series (performed at higher shear strain values), where the second one was performed (i.e. during experiments R 364, R 366, R 370, R 372 and R 374). Differences in healing magnitude and healing rate between first and second SHS series of experiment R 383 are not illustrated because its second SHS test was performed without progressive increase in hold time.

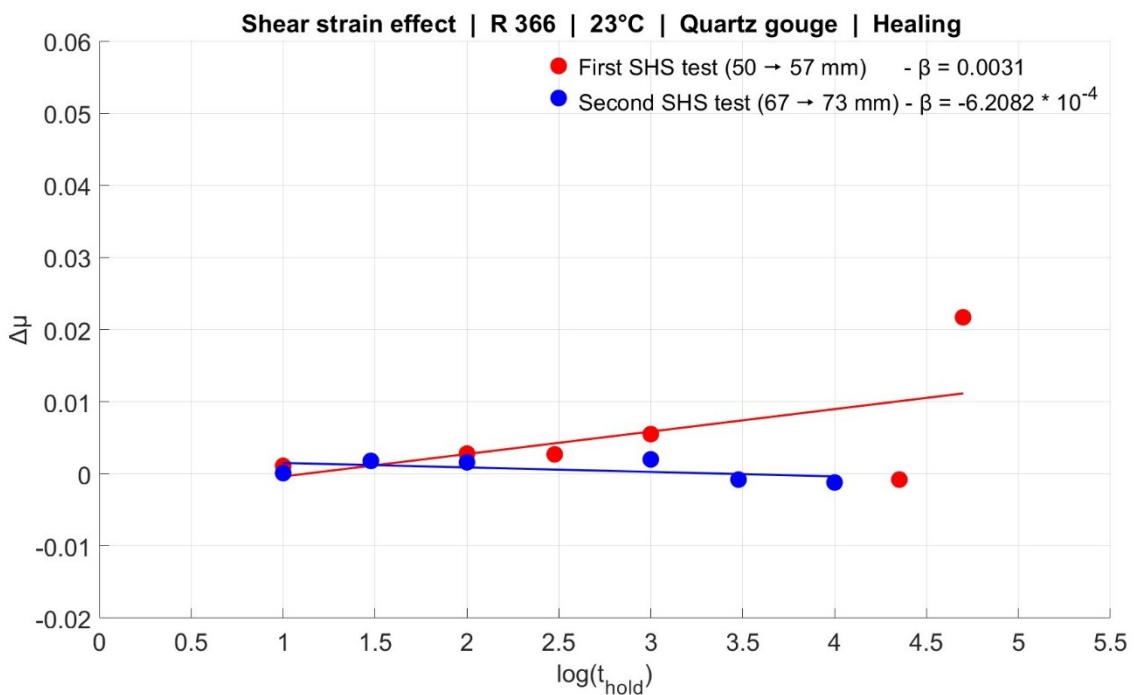


Figure 3.35. Experiment R 366. Healing magnitude and rate comparison between first and second SHS test performed. $\Delta\mu$ plotted against $\log(t_{\text{hold}})$. Healing rate parameter (β) is shown in the box.

The two SHS tests performed during experiment R 366 (23 °C) are separated by ~ 10 mm of slip. This resulted in a large variation of the healing rate parameter (β), which dropped from $\beta = 0.0031$ to $\beta = -6.2082 * 10^{-4}$. In addition, $\Delta\mu$ values corresponding to 3000 s and 10000 s hold are negative. The second SHS test weakened the experimental fault.

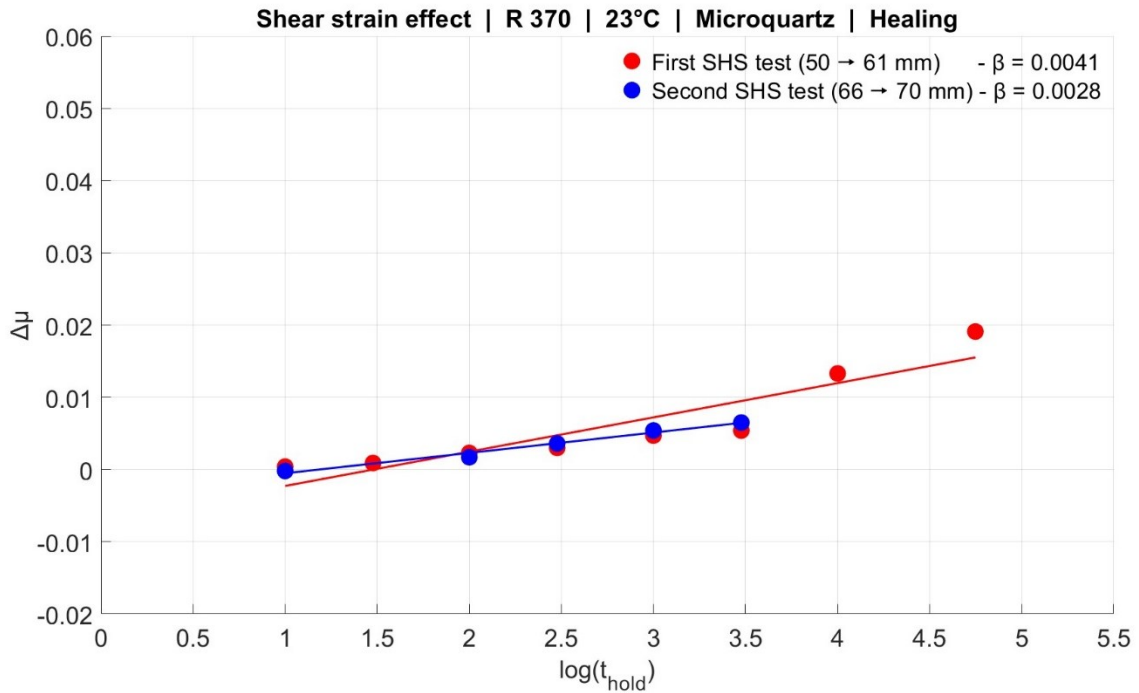


Figure 3.36. Experiment R 366. Healing magnitude and rate comparison between first and second SHS test performed. $\Delta\mu$ plotted against $\log(t_{hold})$. Healing rate parameter (β) is shown in the box.

In the case of experiment R 370 (23 °C), performed on microquartz, the SHS series are separated by 5 mm of slip, exactly half of the slip between the SHS tests of experiment R 366 (Figure X). This minor shear strain did not affect the sample which exhibited almost the same healing magnitude and rate within the two SHS tests performed.

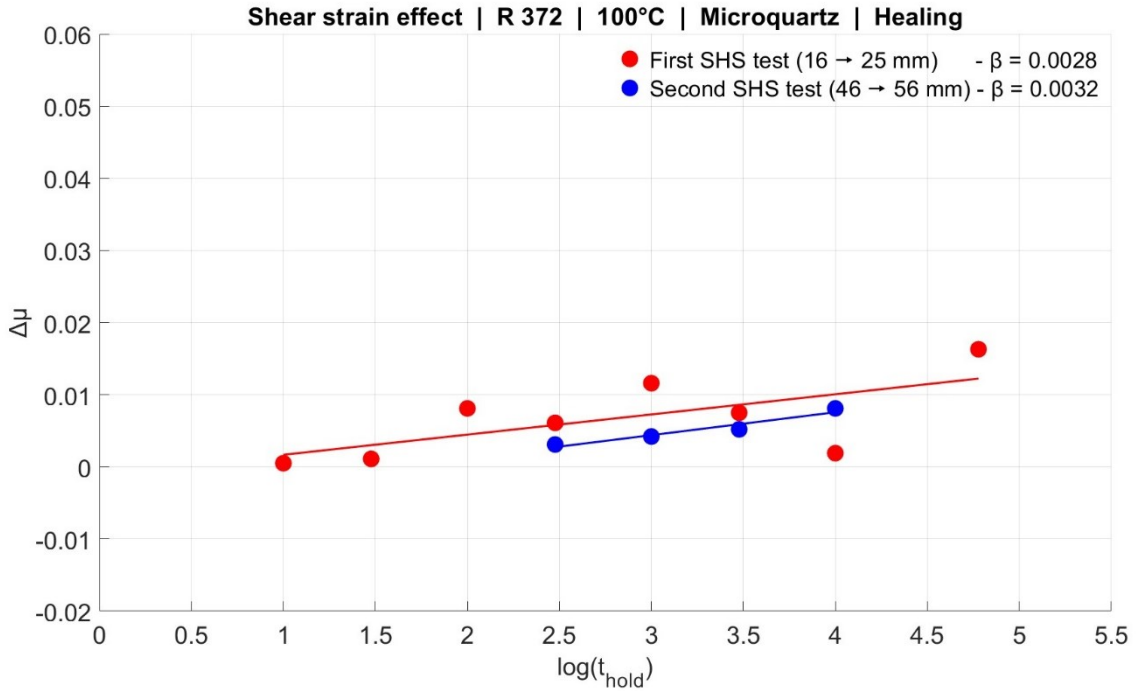


Figure 3.37. Experiment R 370. Healing magnitude and rate comparison between first and second SHS test performed. $\Delta\mu$ plotted against $\log(t_{\text{hold}})$. Healing rate parameter (β) is shown in the box.

Between the two SHS series of experiment R 372 (100 °C), a very large shear strain occurred, since 21 mm of slip separate the two tests. However, this did not produce any significant weakening of the experimental fault. On the contrary, the healing rate parameter (β) slightly increased (from $\beta = 0.0028$ to $\beta = 0.0032$).

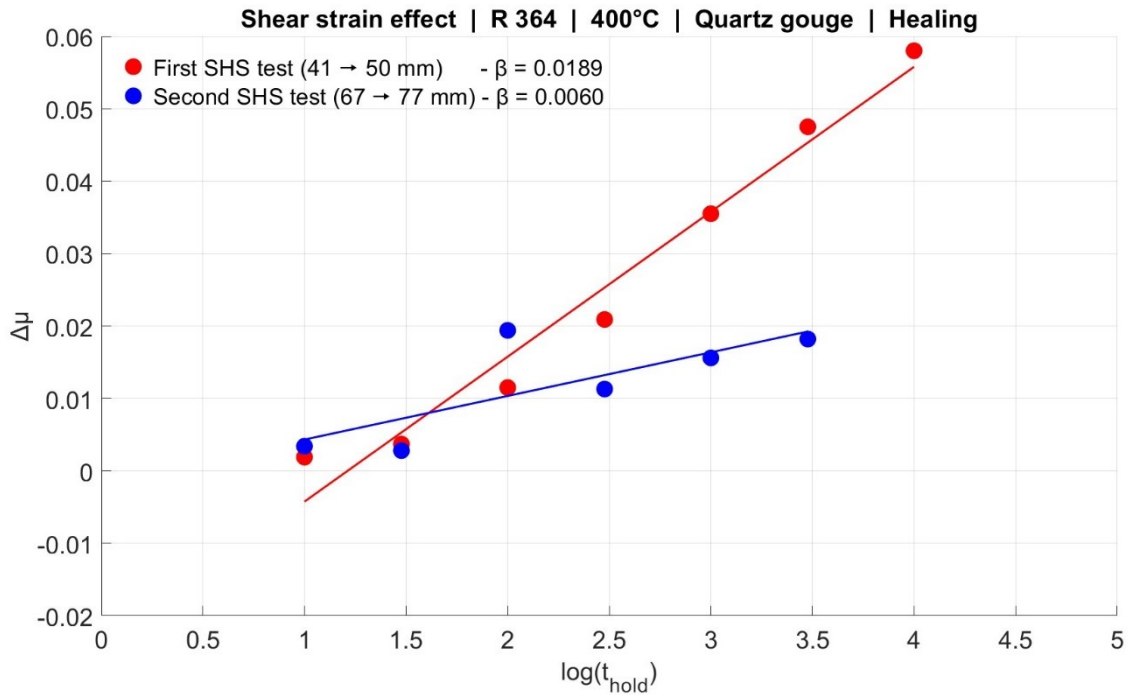


Figure 3.38. Experiment R 372. Healing magnitude and rate comparison between first and second SHS test performed. $\Delta\mu$ plotted against $\log(t_{\text{hold}})$. Healing rate parameter (β) is shown in the box.

In the case of experiment R 364 (400 °C), performed on angular quartz, 17 mm of slip separate the SHS tests. Such shear strain produced a minor strengthening of the experimental fault, as the healing rate parameter (β) dropped from $\beta = 0.0189$ to $\beta = 0.006$. Also healing magnitude ($\Delta\mu$) values decreased from the first to the second test.

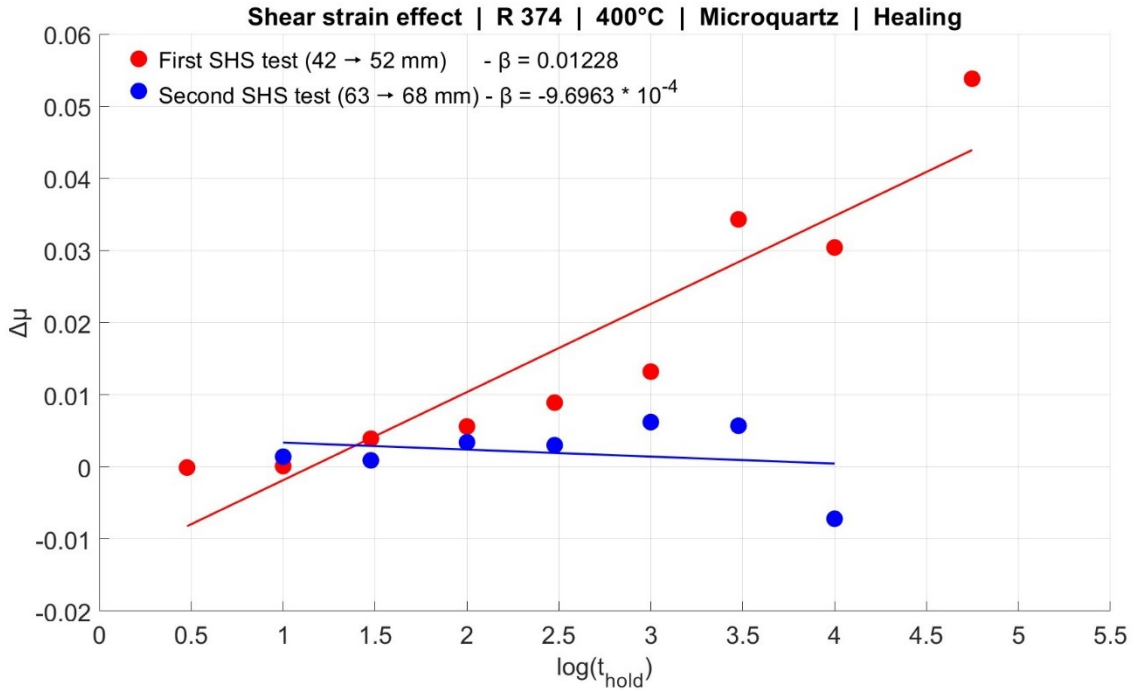


Figure 3.39. Experiment R 374. Healing magnitude and rate comparison between first and second SHS test performed. $\Delta\mu$ plotted against $\log(t_{hold})$. Healing rate parameter (β) is shown in the box.

The data coming from the SHS tests performed during experiment R 374 (400 °C), performed on microquartz, confirm the trend observed in experiment R 364 (Figure 3.38): the healing rate parameter (β) dropped from $\beta = 0.01228$ to $\beta = -9.6963 * 10^{-4}$.

In conclusion, looking at the different healing behaviors shown in the plots (from Figure 3.35 to Figure 3.39), it immediately comes out how each second SHS test show a healing rate parameter (β) generally lower than the one of the first test. It is possible to affirm the same also for healing magnitude values. Table 2 summarizes the difference in healing rate parameter (β) between first and second SHS test in these experiments.

In experiments R 366 (angular quartz, 23 °C) and R 374 (microquartz, 400 °C), β is negative, meaning that higher is the hold time, lower will be the shear strength gained during stationary contact periods. Furthermore, also healing magnitude corresponding to hold times $t_{hold} = 10000$ s results negative in these experiments, indicating that for those hold-slide events the experimental fault lost frictional shear strength with respect to the precedent steady state level.

	Sample type	T (°C)	Slip between SHS tests (mm)	β - 1 st SHS test	β - 2 nd SHS test
R 364	F110 heterometric angular quartz	400	17	0.0189	0.006
R 366	F110 heterometric angular quartz	23	10	0.0031	-0.0006
R 370	Microquartz	23	5	0.0041	0.0028
R 372	Microquartz	100	21	0.0028	0.0032
R 374	Microquartz	400	11	0.0123	-0.0009

Table 2. Healing rate (β) values are shown for each SHS test of experiments R 364, R 366, R 370, R 372 and R 374. The length of the slip occurred between the SHS series is reported.

Table 3 reports some relevant data from each experiment.

	Sample type	Sample weight (g)	Initial thickness (mm)	T (°C)	Compaction during sliding (mm)	Cumulative slip (mm)	Healing rate parameter (β)
R 356	F110 heterometric angular quartz	3.4	3.5	200	0.166	29.6	0.0014
R 359	F110 heterometric angular quartz	1.2	1.3	200	0.182	30.2	0.0139
R 361	F110 heterometric angular quartz	1.2	1.2	100	0.17	26.9	0.0035
R 364	F110 heterometric angular quartz	1.2	1.1	400	0.205	79.4	0.0189
R 366	F110 heterometric angular quartz	1.2	1.4	23	0.202	77.8	0.0031
R 383	F110 heterometric angular quartz	1.2	1.4	23	0.215	98	0.0012
R 368	Microquartz	1.2	1.2	200	0.057	54.2	0.0032
R 370	Microquartz	1.2	1.3	23	0.044	74.7	0.0041
R 372	Microquartz	1.4	1.5	100	0.093	60.6	0.0028
R 374	Microquartz	1.5	1.6	400	0.1	87.3	0.0122

Table 3. Relevant information about each performed experiment. Healing rate parameter (β) refers to the first SHS test.

Chapter 4

Discussion

The fundamental physical-chemical processes underlying the mechanics of the seismic cycles observed in laboratory are reviewed in this chapter. Results obtained by each experiment are discussed, with particular focus on the comparison between the different tests to identify the various mechanical trends as a function of parameters such as temperature (T), effective normal stress (σ_n'), pore fluid pressure (P_p) and grain size. Another parameter affecting the behavior of the gouges, derived from the combination of pressure and temperature variation, is the physical state of the water, which in experiments R 364 and R 374 (400 °C) was in its supercritical state, while in all the other experiments was under liquid conditions. As mentioned before, one of the major goals of this thesis was to assess the deformation mechanisms that operated at the different P - T -grain size conditions, analyzing the healing mechanisms highlighted in the SHS tests.

4.1 The role of fluid

4.1.1 Solubility of quartz

Since all the experiments were performed on quartz (SiO_2) in the presence of hot and pressurized water (H_2O) under liquid (except for experiments R 364 and R 374) and drained conditions, it is important to consider the most important physical-chemical relationships taking place within this system, i.e. SiO_2 - H_2O . First, silica dissolves in water by the reaction



that can be generalized to



because the SiO_2 : H_2O ratio in the aqueous species may not be exactly 1:2 (*Walther & Helgeson, 1977*). The solubility of quartz increases both with increasing temperature and increasing pressure (*Fournier et al., 1982a*) (Figure 4.1). The increase in quartz solubility with increasing pressure is related to the interaction of the OH groups of H_4SiO_4 with dipolar water molecules. This hydrogen-bonding reaction was investigated by *Chakoumakos & Gibbs (1986)* who found that two water molecules arrange around the OH groups of H_4SiO_4 with a particular “lowest energy configuration”.

Increasing pressure results in increasing density of water, so there are more water molecules in the neighborhood of the OH groups increasing the frequency of encounters between the H_4SiO_4 and H_2O molecules. This results in a greater silica solubility (*Dove & Rimstidt, 1994*).

On the other hand, since

$$\Delta G_r = \Delta H_r - T\Delta S_r, \quad (4.3)$$

where ΔG_r is the Gibbs free energy of the reaction, ΔH_r is the enthalpy of the reaction, T is the temperature and ΔS_r is the entropy of the reaction. Increasing temperature causes the $T\Delta S_r$ to become larger making ΔG_r more negative so that quartz solubility increases. In addition, ΔH_r can be further described as:

$$\Delta H_r = \Delta Q + \Delta W, \quad (4.4)$$

where ΔQ is the thermal work and ΔW is the mechanical work.

The mechanical work ΔW could be subdivided into:

$$\Delta W = PdV + VdP. \quad (4.5)$$

Assuming a quasi-isochoric system for the experiments of this thesis, PdV is negligible. VdP is interpreted as the work to be done to overcome frictional forces at asperities contacts, where normal load concentrates. In this case, the large negative difference in pressure between stressed asperities and less stressed zones makes VdP negative, resulting in a reduction of ΔG_r and increasing the solubility of silica.

Another parameter which solubility of quartz depends on is the grain size. The solubility of convex surfaces (positive radius of curvature) increases with decreasing particle size. For radii less than $\sim 0.1 \mu\text{m}$ the particles have a measured increased solubility. This causes small particles to dissolve while large particles increase in size. On the other hand, the solubility of silica at concave surfaces decreases with decreasing radius of curvature. This produces silica precipitation at or near the tips of cracks to cause the closed growth of cracks, resulting in a crack healing mechanism (Dove & Rimstidt, 1994). This may have a big relevance while considering frictional experiments under hydrothermal conditions, as the dissolution and precipitation processes depend on the solubility of quartz in an aqueous fluid. Probably during shearing stages the solubility of quartz increases with the number of small particles ($< \sim 0.1 \mu\text{m}$) due to cataclastic processes, while during stationary contact periods quartz tends to precipitate from crack tips, contributing to enhance the operating healing processes.

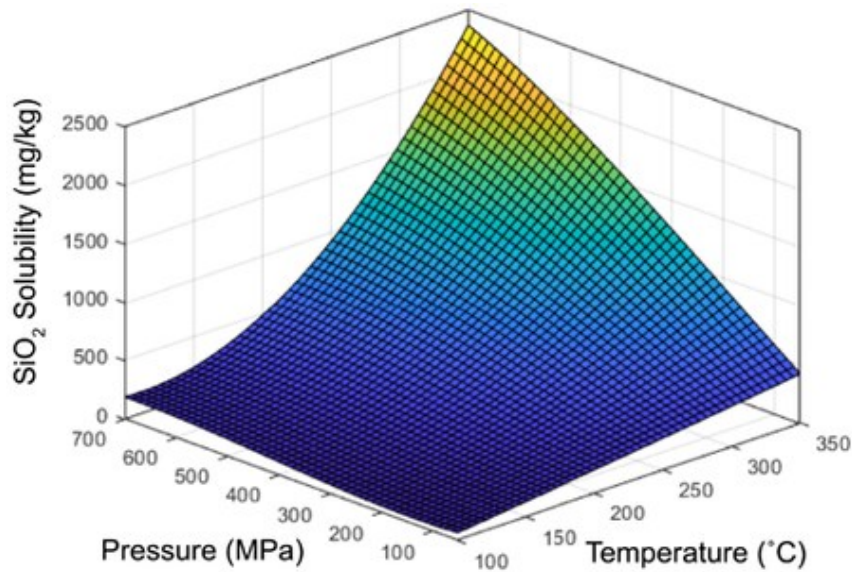


*Figure 4.1. SiO₂ solubility as function of pressure and temperature.
From Williams & Fagereng, 2022.*

4.1.2 Mechanical role of fluid

The inelastic mechanical properties of rocks are strongly influenced by the presence of aqueous fluids, both through physical changes in the state of stress associated with the introduction of internal pore pressure and through chemical interactions that change the energetics of breaking bonds (*Kronenberg, 1994*).

Hydrogen species adsorbed at quartz surfaces lead to significant reductions in surface energies (γ) altering the kinetics of reactions between H_2O , OH and Si-O bonds at crack tips (*Freiman, 1984*). Surface energies may decrease by an order of magnitude as hydrogen species are adsorbed, dropping from values in excess of 2 J/m^2 for quartz surfaces exposed to high vacuum to $\gamma = 0.4\text{-}0.45 \text{ J/m}^2$ for surfaces saturated with H_2O and to $\gamma = 0.3\text{-}0.4 \text{ J/m}^2$ for surfaces in contact with water (*Kronenberg, 1994, and references therein*).

Again, grain comminution plays a significant role in affecting the surface energy of particles, producing smaller grains with higher S/V ratio counterbalancing the loss due to water contact. The relevance of this topic concerns the dynamic shear strength of rocks, since smaller particles with higher S/V ratio are tougher to break. Consistently, I observe that microquartz gouges, with grain size already reduced before the experiments, are relatively stronger than coarser heterometric F110 quartz.

Grain comminution and water-related surface energy loss are antagonistic processes as one strengthens the grains on the sliding surface, while the other weakens them (via film of fluid within the slip plane).

4.1.3 Pressure solution mechanism

I observe that compaction in the experiments of this thesis occurs under both shearing and quasi-static loading conditions. Also, both higher stress (e.g. Figure 3.22) and temperature (Figure 3.22, 3.25) favor inelastic compaction of the fault gouges, suggesting a fluid-mediated and stress/temperature favored process of grain compaction.

Compaction and viscous creep of quartz gouges may occur through a variety of processes, including pressure solution, if interstitial and thin fluid films exist between quartz grains to promote silica transport (*Kronenberg, 1994*). With pressure solution, dissolution of quartz occurs at grain boundaries on highly stressed surfaces, diffusion through intergranular fluid films and precipitation within less stressed surfaces. This may lead to

a further welding of grain-to-grain contacts, resulting in a huge healing of the experimental fault, in addition to compaction and shape changes by porosity reduction. Solubility of silica could play a fundamental role in increasing locally, leading to dissolution of silica molecules. Strain rates may be controlled both by quartz-water reaction kinetics and by dissolution rate within intergranular fluid films (*Niemeijer et al., 2002; Rutter, 1983*). Intergranular fluid films are thought to exist since continued dissolution and precipitation requires silica transport from sources to sinks by diffusion processes (*Rutter, 1976*). Characteristic texture are grain interpenetration and overgrowth (Figure 4.2), and stylolites at much larger scale. *Yasuhara et al. (2005)* demonstrated experimentally pressure solution while shearing gouges is a thermally activated and enhanced mechanism.

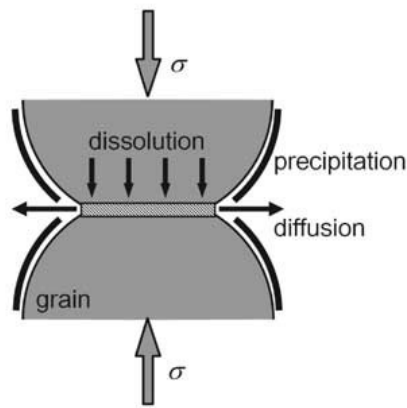


Figure 4.2. Schematic illustration of pressure solution. This incorporates the serial processes of dissolution at grain-to-grain contacts, interfacial diffusions, and precipitation at the free wall of grain and results in growth and welding of the contact area. From *Yasuhara et al., 2005*.

4.2 Slip hardening and friction

From the initiation of slip to the first 15 to 20 mm, each experiment showed a slip hardening stage, during which friction evolved until μ_{ss} was achieved. First 1-1.5 mm of slip are characterized by rapid shear stress increase along an elastic loading curve followed by the onset of inelastic strain and achievement of a peak strength with a friction coefficient $\mu = 0.53-0.65$ for angular quartz and $\mu = 0.65-0.69$ for microquartz. This trend is consistent with most of precedent works on hydrothermal experiments on quartz (*Karner et al., 1997; Niemeijer et al., 2008*).

Initial friction occurs by slip of normally contacting asperities, strengthening nonlinearly with slip, so the rate of increase was diminishing with displacement, i.e. du/dx decreased with slip (Scholz, 2019). If the sliding surface has relatively long-wavelength asperities as measured for natural surfaces in Scholz (2019), when sliding commences the asperities may ride up one on another, so that sliding occurs at a small angle Ψ to the direction of the applied shear stress. This process is called *asperity interlocking*, and is responsible for the initial slip hardening stage, but also for the initial *joint dilatancy* during first 0.3-1 mm of slip (Figure 4.3) since a component of the motion is perpendicular to the sliding surface. At major grain scale, the same process is called *grain rolling* (Figure 4.4) and is responsible for the same effects produced by asperity interlocking.

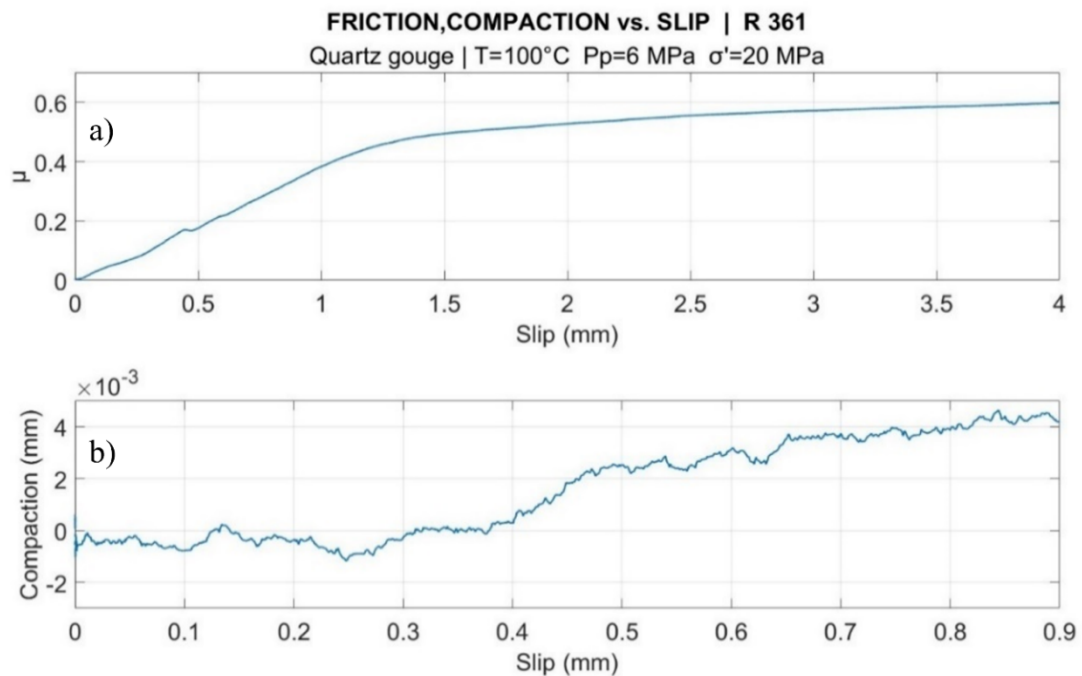


Figure 4.3. a) Initial hardening phase observed in experiment R 361 and b) Initial dilatancy.

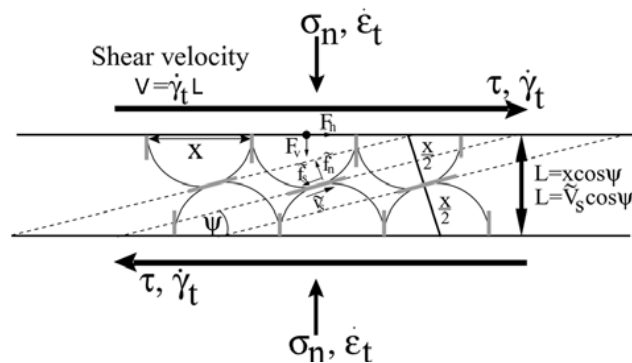


Figure 4.4. Grain rolling mechanism in a simulated fault gouge. Dilatancy angle Ψ is indicated. From Niemeijer & Spiers, 2007.

A minor role in this initial hardening and dilatancy stage could be played by *dilatancy hardening* effect, as suggested by *Segall & Rice (1995)* and *Helmons & Miedema (2013)*. Dilatancy hardening is found to be an efficient mechanism with low ambient permeability: in this case shear-induced dilation causes a local pressure drop within the pores previously filled by pressurized fluid, leading to a strengthening of the gouge.

However, it's widely accepted how permeability k is function of the grain size as follow (*Shepherd, 1989*):

$$k = ad^2. \tag{4.6}$$

Where a is a dimensionless fit constant and d is particle diameter.

Although permeability of quartz gouges is known to assume high values (10^{-14} to 10^{-19} m²) (*Townend & Zoback, 2000; Giger et al., 2007*), *Zhang & Tullis (1998)* analyzed how mechanical shearing of quartz gouge shows a sharp decrease in permeability due to grain size reduction within the sliding interface.

In my experiments, as the initial run-in phase starts the gouge needs to localize the slip within a thin surface by grain crushing and comminuting, creating an increasingly finer grain size within the localized slip zone. This results in a decreased dilatancy effect in experiments performed on F110 heterometric angular quartz with respect to experiments performed on microquartz. Once the gouge found a localized plane where slip became efficient, grain comminution processes stopped as the energy provided by the apparatus was enough to reactivate the well-oriented experimental fault instead of breaking new grains and creating new cracks, and steady state was achieved.

4.3 The role of temperature

4.3.1 Temperature effect during first stages of slip

Temperature is the parameter which varied the most within my experimental series, since I performed experiments at 23 °C, 100 °C, 200 °C and 400 °C. Figure 4.5 summarizes the first stage of each experiment in term of friction coefficient (μ). It seems to be present an almost neglectable temperature dependence on the steady state sliding friction μ_{ss} reached before the intervention of any SHS test, since for angular quartz μ_{ss}

goes from ~ 0.59 to ~ 0.65 while for microquartz μ_{ss} goes from ~ 0.65 to ~ 0.69 . Friction curves at different temperatures (Figure XX) for each experiment are quasi juxtaposed, apart from experiments R 366 and R 383, the ones performed at room temperature, which result to slide at lower μ_{ss} values. In Figure 4.6, the plots do not show any change in compaction trend in correspondence of achievement of frictional steady state, indicating a non-dependence of vertical displacement on the rate of shear strength $d\mu/dt$ of the gouges while sliding. Focusing on Figure 4.6, I observe that the lower compaction during the first 30 mm of slip is generally attributable to experiments performed at 400 °C, except for experiment R 366 (23 °C) which shows even lower values. This relationship could be explained by thermal expansion provided firstly by the large amount of heat available, and then by frictional heating produced along the gouge radius while sliding. However, given the very low slip rate (10 $\mu\text{m/s}$), frictional heating thermal expansion could be neglected (Rice, 2006).

Furthermore, during loading stage and equilibration time, samples exposed to higher temperatures could have experienced higher compaction related to pressure solution, leading to a subsequent minor compaction during initial run-in.

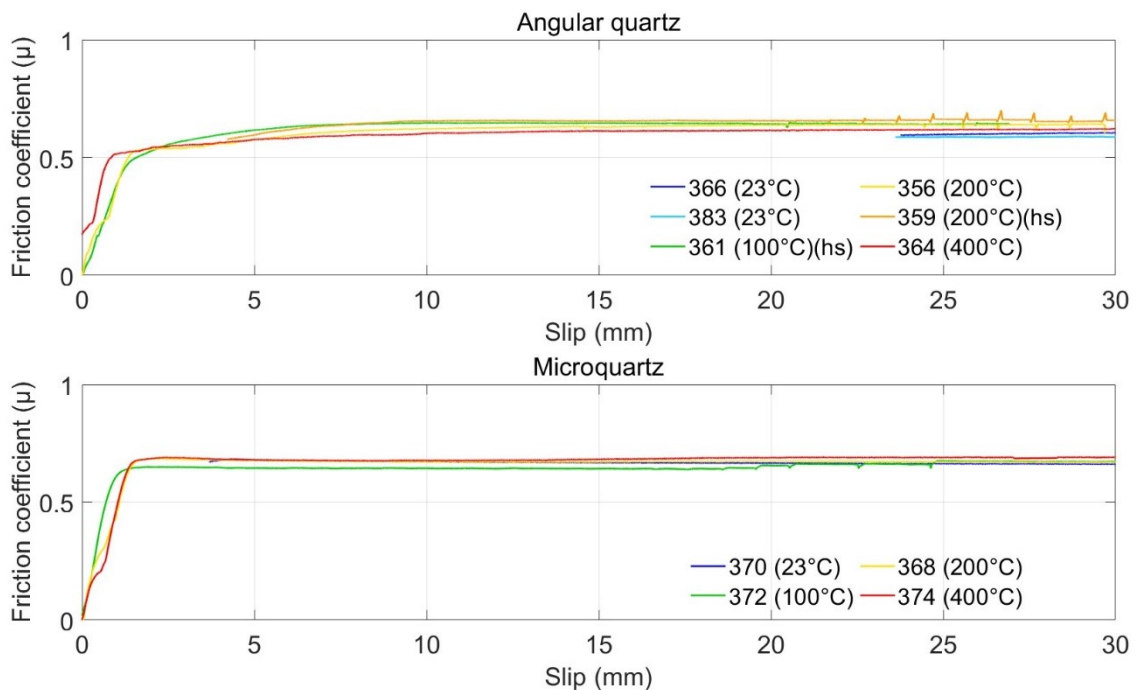


Figure 4.5. Comparison between friction coefficient (μ) of all experiments during the first 30 mm of slip. Lines appear to be juxtaposable both for F110 heterometric angular quartz and for microquartz.

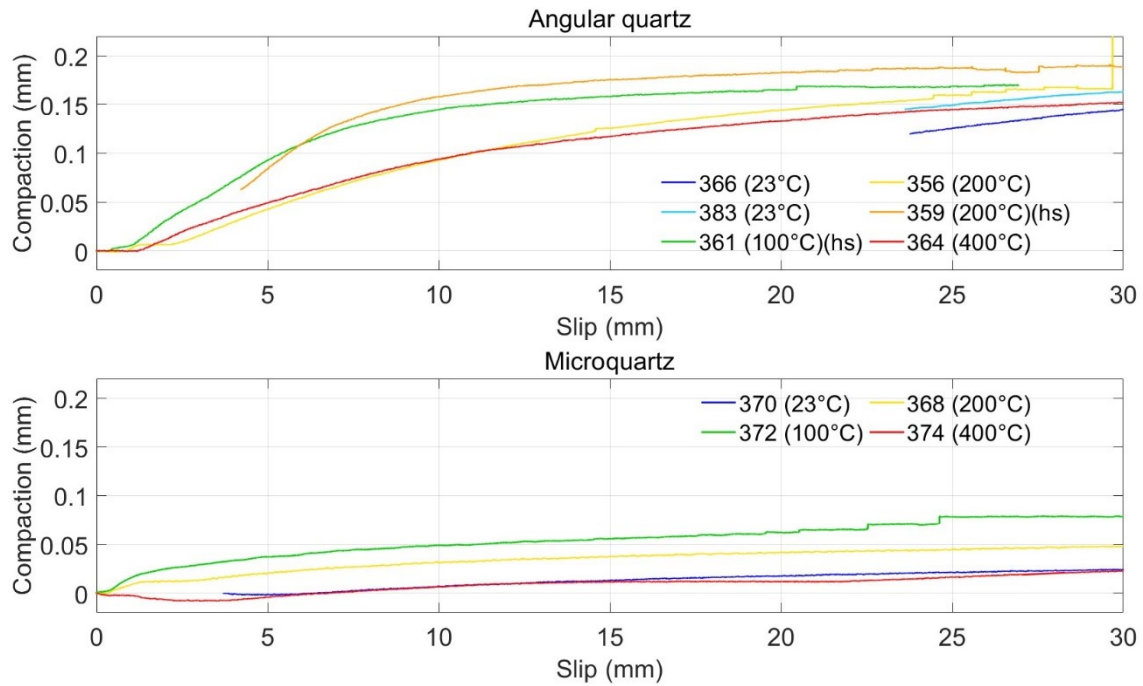


Figure 4.6. Comparison between compaction (mm) of all experiments during the first 30 mm of slip.

4.3.2 Temperature effect on healing

A major role of temperature in frictional experiments can be played during SHS tests. Looking at the comparison between SHS tests in experiments R 370 (23 °C), R 372 (100 °C), R 368 (200 °C) and R 374 (400 °C) (Figure 4.7), performed under the same σ_n' - P_p -grain size conditions, it's easy to appreciate the effect of temperature on steady state friction before and after the simulated interseismic time and the effect on the healing magnitude. The SHS test performed in experiment R 370 (23 °C) stepped the steady state friction coefficient (μ) from ~ 0.67 to ~ 0.68 , producing an increase of 1.4% with respect to μ_{ss} before the SHS test. In experiment R 372 (100 °C), the SHS test raised the friction coefficient (μ) from ~ 0.64 to ~ 0.68 , producing an increase of 6.2% with respect to μ_{ss} before SHS test.

For experiments R 368 (200 °C) and R 374 (400 °C), the shear strength during SHS tests increased for both from $\mu \sim 0.69$ to ~ 0.77 , corresponding to an enhancement of 11.6 % with respect to μ_{ss} before SHS test.

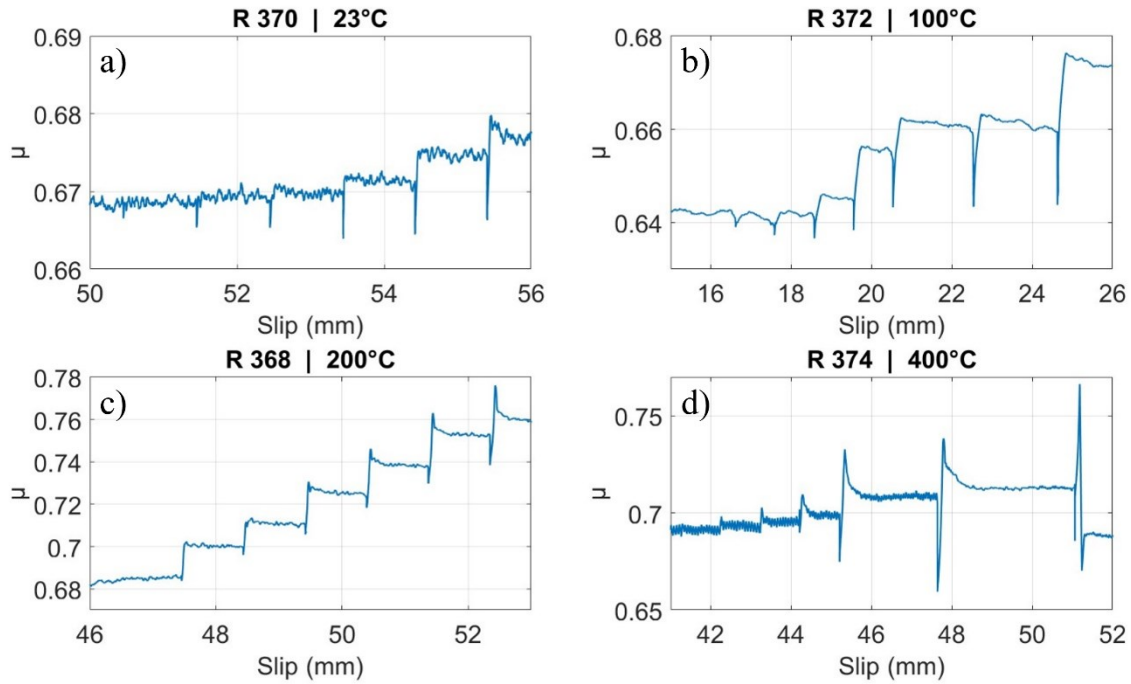


Figure 4.7. Temperature effect on the shear strength during SHS tests performed in experiments R 370, R 372, R 368 and R 374.

These measurements describe the enormous influence of temperature on the shear strength gained during hold times by the experimental faults. Looking at the plots showed in section 3.3.1, the majority of healing data in this thesis can be fitted with a linear regression, extrapolating a regression coefficient, that is the healing rate parameter (β). However, plots showing healing magnitude ($\Delta\mu$) against $\log(t_{hold})$ relative to experiments performed at 400 °C fit better with a 2nd degree polynomial in the form:

$$y = ax^2 + bx + c. \quad (4.7)$$

Coefficients for the polynomial which fits data of experiment R 364 (Figure 4.8) are:

$$a = 0.0034$$

$$b = 0.0028$$

$$c = -0.0062,$$

and coefficients for the polynomial which fits data of experiment R 374 (Figure 4.9) are:

$$a = 0.0032$$

$$b = -0.0042$$

$$c = 0.0014.$$

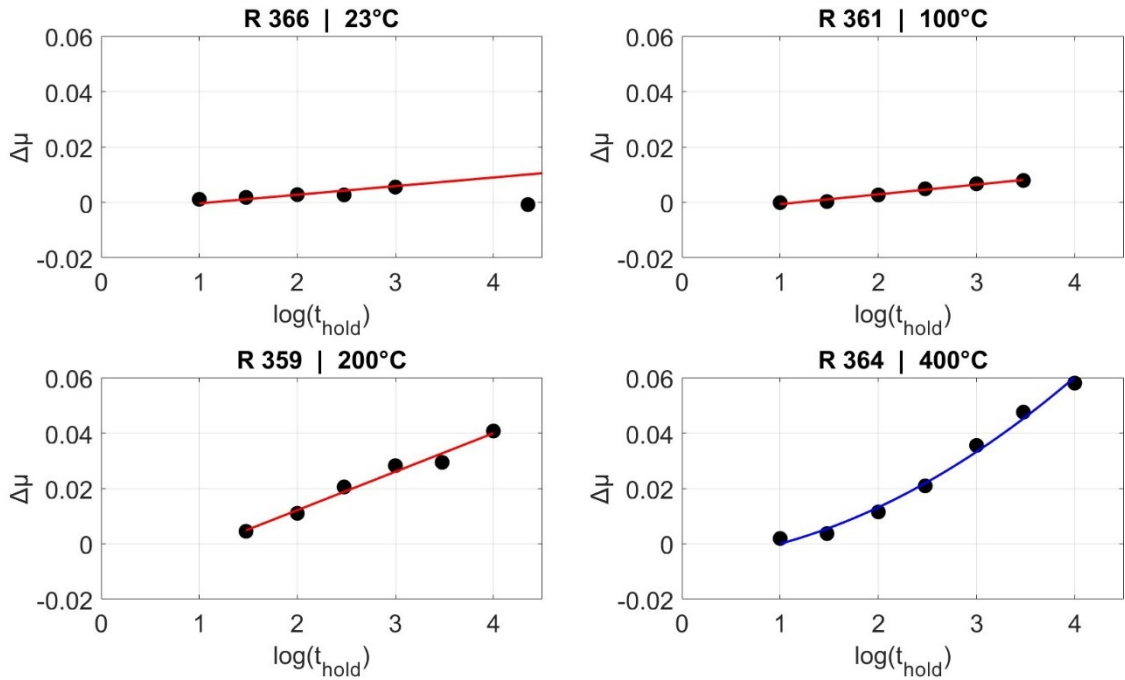


Figure 4.8. Comparison between healing magnitude and rate measured in experiment performed on F110 heterometric angular quartz. Experiment R 364, performed at 400 °C results fitted better with a 2nd degree polynomial, with respect to experiments performed at lower temperatures. The data are relative to the first SHS test.

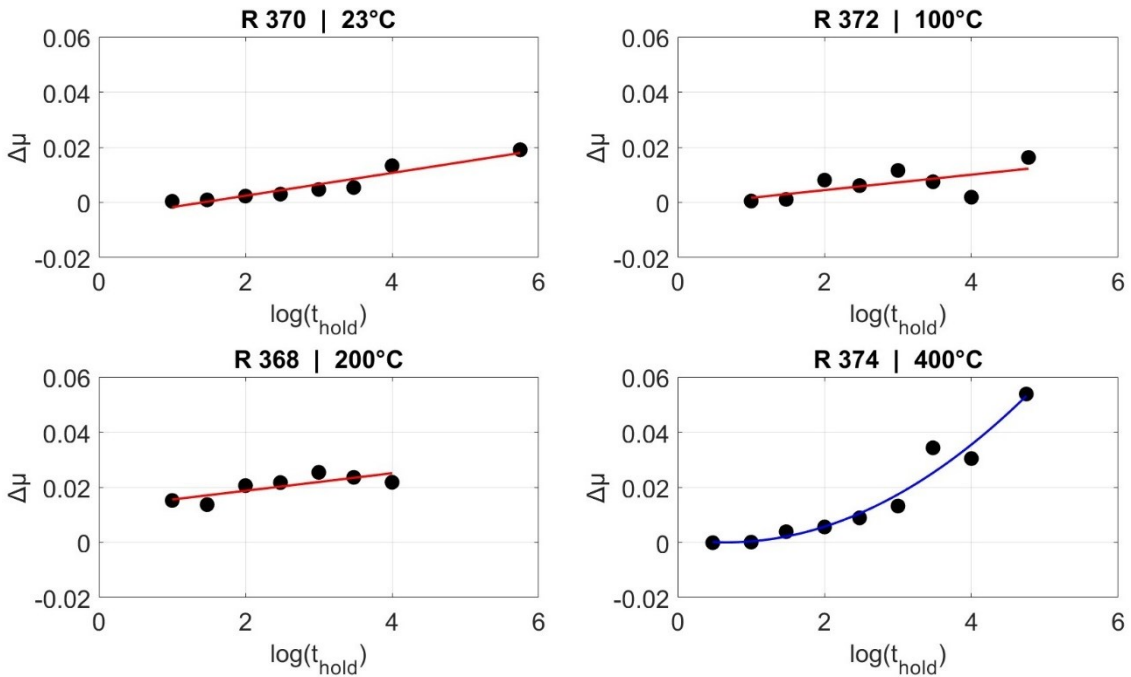


Figure 4.9. Comparison between healing magnitude and rate measured in experiment performed on microquartz Experiment R 374, performed at 400 °C results fitted better with a 2nd degree polynomial, with respect to experiments performed at lower temperatures. The data are relative to the first SHS test.

This is clearly indicating how temperature affects the relationships between both healing magnitude ($\Delta\mu$) and rate (β), and $\log(t_{hold})$. These results are consistent to what found in previous similar studies (*Karner et al., 1997; Nakatani & Scholz, 2004; Yasuhara et al., 2005; Chen et al., 2015*). While until 200 °C $\Delta\mu$ increases linearly with temperature, over this threshold temperature $\Delta\mu$ starts to increase quadratically with the logarithm of hold time, in the form:

$$\Delta\mu = [\log(t_{hold})]^2. \quad (4.8)$$

In experiments R 370 (23 °C) and R 372 (100 °C) (Figure 4.7a and b), once the laboratory fault gets reactivated friction reached μ_{peak} values and maintained a sort of plateau with $\mu_{peak} \approx \mu_{ss}'$ after the reshear event (light slip softening behavior in experiment R 372). On the other hand, in experiments R 368 (200 °C) and R 374 (400 °C) (Figure 4.7c and d) the laboratory fault reached μ_{peak} values to then drop to lower μ_{ss}' values. μ_{ss}' is defined as the steady state friction coefficient measured after the friction peak upon reshear.

$\Delta\mu_{drop}$ is therefore defined as:

$$\Delta\mu_{drop} = \mu_{peak} - \mu_{ss}'. \quad (4.9)$$

$\Delta\mu_{drop}$ values were fitted with a 2nd degree polynomial in the form of eq. (4.7):

$$y = ax^2 + bx + c. \quad (4.10)$$

Coefficients for the polynomial which fits data of experiment R 368 are:

$$a = 0.0024$$

$$b = - 0.0046$$

$$c = 0.0055.$$

While coefficients for the polynomial which fits data of experiment R 374 are:

$$a = 0.0041$$

$$b = - 0.0117$$

$$c = 0.0111.$$

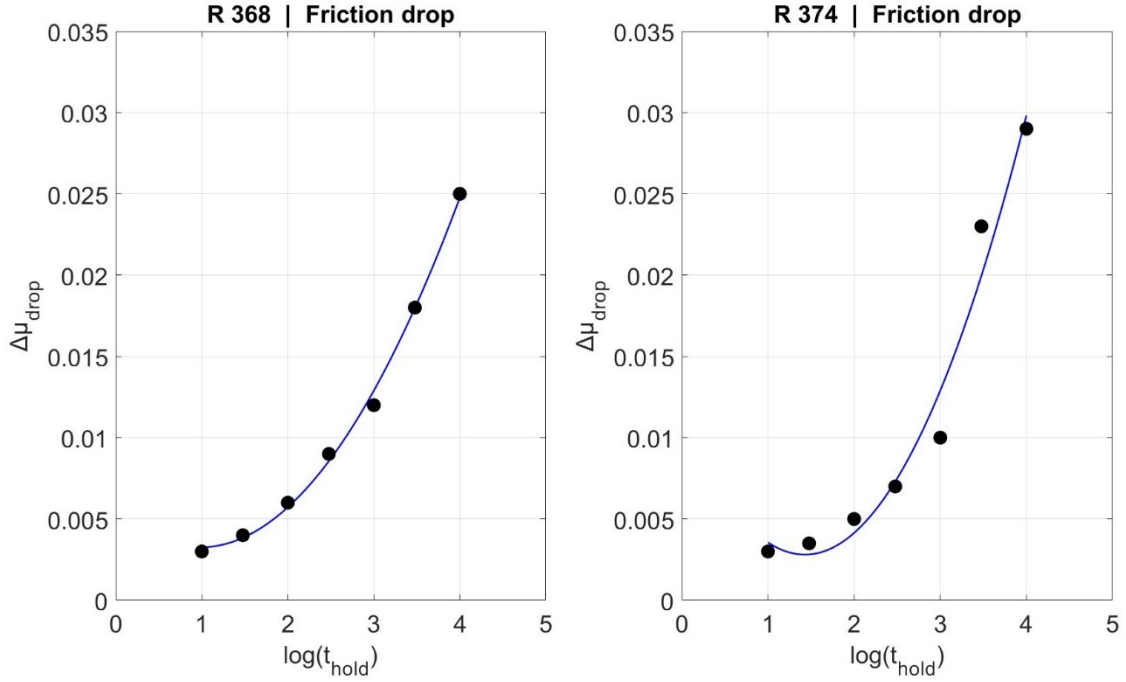


Figure 4.10. Friction drop ($\Delta\mu_{drop}$) plotted against $\log(t_{hold})$ in SHS test of experiments R 368 (200 °C) and R 374 (400 °C).

These data are suggesting that a major role is played by temperature in enhancing μ_{peak} values after a reshear event during a SHS test. This has no influence on the dynamic steady state μ_{ss} , as the quartz gouge is not capable of maintaining the shear strength gained during hold. The friction drops after μ_{peak} also increase quadratically with the logarithm of hold time, in the form of eq. (4.8):

$$\Delta\mu_{drop} = [\log(t_{hold})]^2. \quad (4.11)$$

These data confirm how temperature enhances not only healing magnitudes and rates but also friction drops.

The physical interpretation of these post-peak weakening behavior is related to pressure solution mechanism. Pressure solution (as already mentioned) operates in the presence of a thin fluid film at the interface between two stressed surfaces and its rate may be controlled by silica dissolution and/or diffusion at this interface/within intergranular fluid.

Dissolution is in turn controlled by solubility of quartz, which at this pressure ($\sigma_n' = 10$ MPa, $P_p = 36$ MPa) increases quasi-linearly with increasing temperature, as can be found in Figure 4.1. Highly stressed grain-to-grain contacts lead to higher dissolution of silica accompanied by transport through intergranular fluid probably during hold times.

All these processes result in a welding of grain-to-grain contacts and in an increase of the real contact area, distributing normal loads over a wider surface and so resulting in a higher shear strength. Increase in contact area is also accompanied by marked compaction during holds (discussed below).

Another strengthening factor is represented by the neck growth through reprecipitation of silica, concurring to increase the shear strength of the bonds between grains. The energy required to break these strengthened grain-to-grain contacts, recreate a critical dilatancy (destroyed by compaction) and a new localized plane to slip is much higher than the one required to break grain-to-grain contacts that have not experienced these processes. This may result in a large release of elastic strain energy, and microcrack growth and propagation could lead to the complete failure of the microstructures produced during static loading, hence the friction drops. Friction drops are not present in experiments performed at lower temperature, probably because under certain temperature threshold pressure solution mechanisms do not efficiently operate, resulting in a better conservation of the “*paleo slip zone*”. Much less energy is required to make the surfaces shear again. Then, minor (or absent) friction drop occurs in sliding again along the old slip zone.

Dieterich (1972, 1994) described frictional healing observed in experiments under dry (room humidity) conditions as a time-dependent mechanism due to the increase in real contact area between grains (Figure 4.11). The explanation for the increase of real contact area provided by *Dieterich (1972)* was that the formation of adhesive junctions (asperities) across the slip surface is controlled by time-dependent localized plastic flow in the area of contact points, so the real contact area increased with increasing stationary contact time.

Frictional experiments performed by *Dieterich (1972)* showed a linear relationship between healing magnitude ($\Delta\mu$) and $\log(t_{hold})$, in the form:

$$\Delta\mu = \beta \log(t_{hold}), \tag{4.12}$$

where β represents the coefficient of the regression line used to fit the healing data.

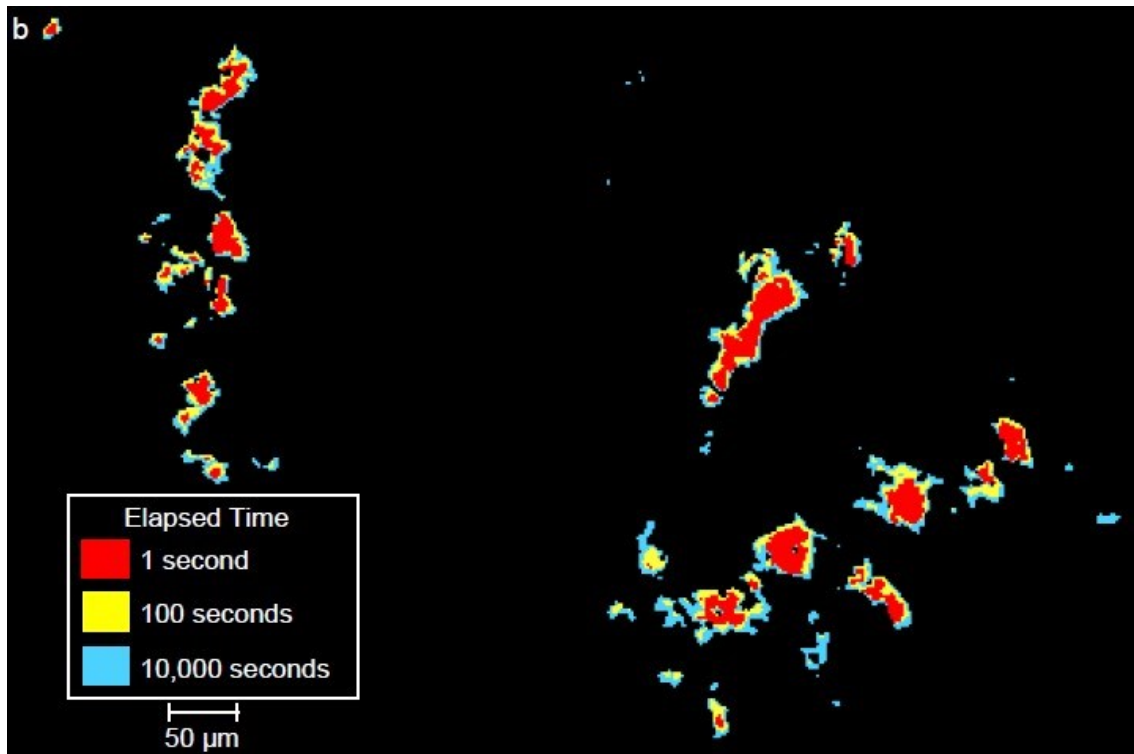


Figure 4.11. Time-dependent increase in contact area. From Dieterich & Kilgore, 1994.

Looking at compaction values during SHS tests (Figure 4.12), it seems that temperature also in this case affected the mechanical behavior of the gouges. As already mentioned in section 3.2, compaction measured during SHS series at different temperatures resulted affecting the samples in a different way. In experiment R 370 (23 °C, microquartz), during SHS test the gouge compacted of 17% with respect to the total compaction. This value accounts for the 24.7% in experiment R 372 (100 °C, microquartz), 5.2% in experiment R 368 (200 °C, microquartz) and 58% in experiment R 374 (400 °C, microquartz).

Except for experiment R 368, the data show again a clear dependence of compaction on temperature during SHS tests. Focusing on the plots in section 3.1, it's noticeable that samples compacted during hold stages and not when reshear phases occurred. This could be related to pressure solution mechanism leading to further compaction (*Kronenberg, 1994; Niemeijer et al., 2002; Bos & Spiers, 2002; Yasuhara et al., 2005*), for the reasons discussed earlier.

Another possible explanation is related to plastic deformation that likely occur for quartz above 300-350 °C. Low-temperature plasticity, in which dislocation glide dominates (pile-up of dislocation and work hardening to be done) associated with recovery and recrystallization may be considered as a secondary deformation mechanism, under a brittle overprint (*Brace & Kohlstedt, 1980; Scholz, 1988*).

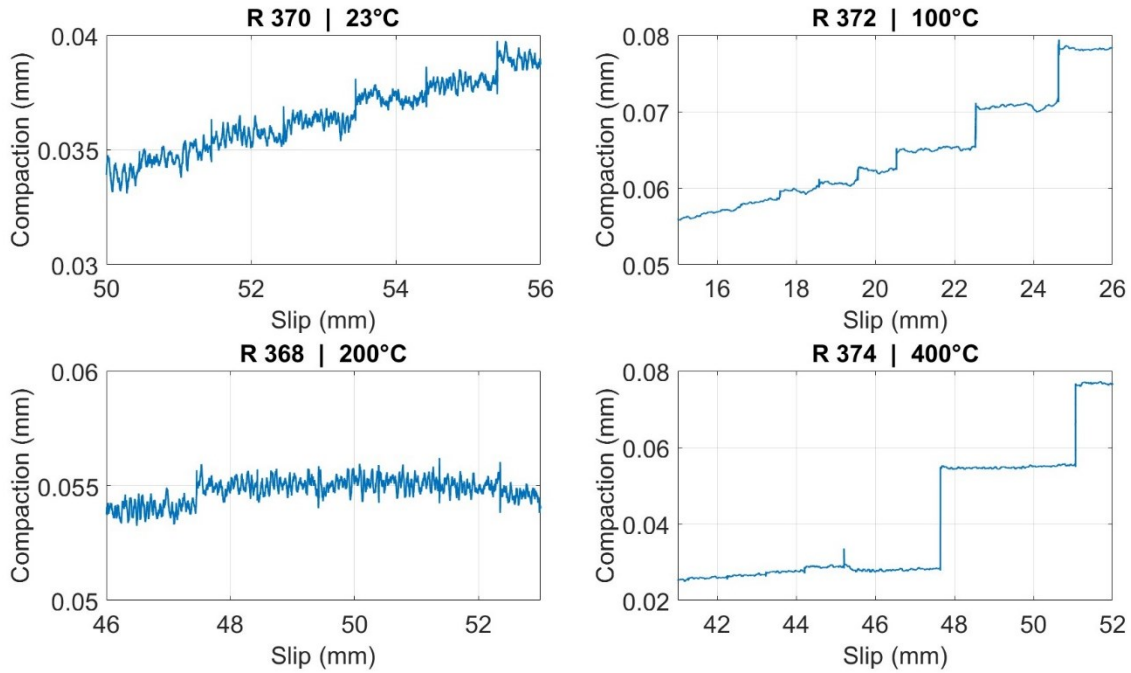


Figure 4.12. Temperature effect on the compaction values during SHS tests performed in experiments R 370, R 372, R 368 and R 374. The data refer to the first SHS test in experiments performed on microquartz.

This ductile deformation style is often associated with cataclastic processes, as work hardening allows stresses to raise until brittle processes occur. This plastic behavior could be related to inelastic compaction occurring during hold times, associated to restrengthening measured in high temperature experiments.

In conclusion, pressure solution-related compaction is thought to be accompanied by time-related increase in asperity contact areas in experiments performed at temperatures up to 200 °C. Regarding high temperature experiments (i.e. at 400 °C), that show highly non-linear healing, pressure solution could be accompanied by cementation-related neck growth, due to higher silica concentration (induced by temperature) which favors silica precipitation within less stressed surfaces.

4.4 The role of grain size

One of the major aims of this thesis was to determine whether and how grain size could influence the mechanical behavior of the gouges. Results in section 3.3.2 show how smaller grains are harder to break, leading to a higher friction coefficient (μ) in all experiments, consistent with results from *Scott et al. (1994)*. This, as discussed before,

could be due to the higher S/V ratio of smaller grains, that results in a higher surface energy of the particles and in a higher energy required to break them and localize the slip (Figure 4.13). Another interesting data to discuss is how gouges reach steady state friction μ_{ss} during the first millimeters of slip. While in experiment performed on angular quartz ($< 110 \mu\text{m}$) frictional steady state is achieved through progressively increasing shear strength passing through a not well-defined yield point around 1.5-2 mm of slip, in experiments performed on microquartz ($< 5 \mu\text{m}$) steady state is achieved through overcoming the yield point peak friction around 1.5-2 mm of slip followed by a slip weakening behavior toward μ_{ss} value, usually reached after 10-20 mm of slip.

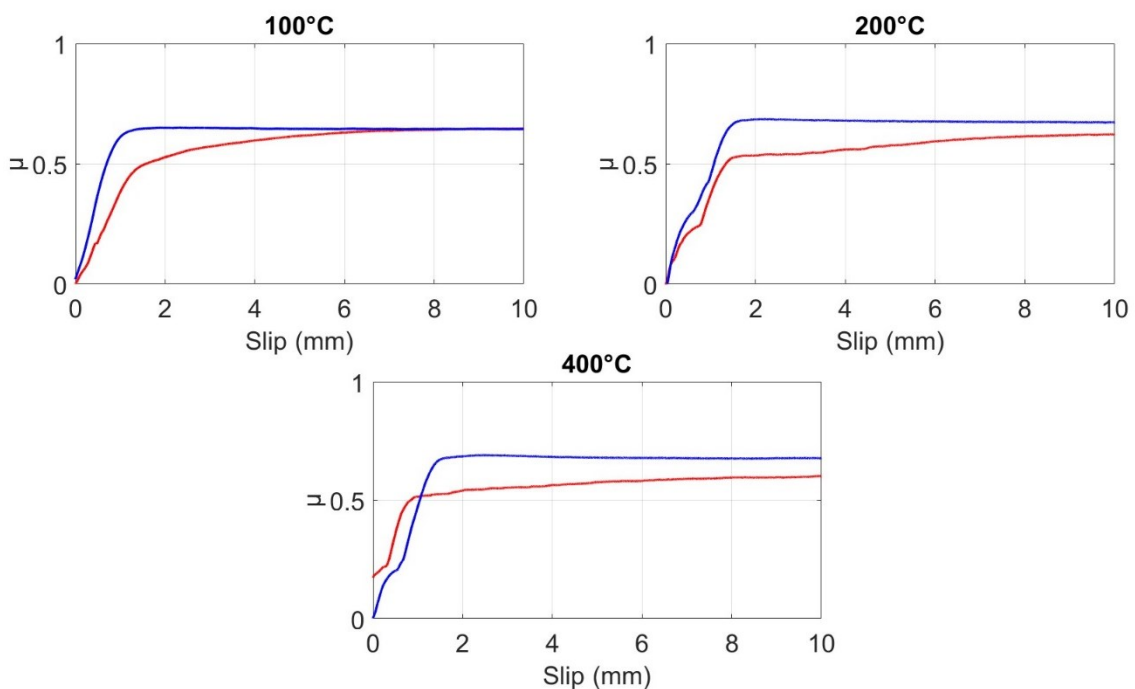


Figure 4.13. Experiments performed on gouges with different grain size exhibit different shear strength during the first 10 mm of slip. Blue line: microquartz; Red line: F110 heterometric angular quartz.

Another parameter that could be influenced by the grain size is the healing, both magnitude and rate. As mentioned before, dissolution/precipitation of quartz is controlled by solubility of silica. Within convex surfaces solubility increases with decreasing particle size (for radii $< \sim 0.1 \mu\text{m}$), while for concave surfaces solubility decreases with decreasing particles radii. This could result in enhanced or diminished role of pressure solution during hold-slide events, leading to different types of healing in function of different grain size. Looking at Figure 4.14, grain size does not influence in any way the magnitude and the rate of healing in experiments performed at temperatures up to 100 °C.

Experiments performed at 200 °C show an influence of grain size on the magnitude of healing but not on its rate. Experiments performed at 400 °C show an influence of grain size on both magnitude and rate of healing. These results could be interpreted by attributing a fundamental role to solubility-controlled pressure solution mechanisms. At temperatures up to 100 °C probably pressure solution is not enough efficient to deform the gouge, so cataclastic processes (grain fracturing and comminution) dominate. At temperatures of 200 °C, healing rate results identical in both angular quartz and microquartz, but healing magnitude is higher in microquartz gouges. The reason for this difference could be related to higher dissolution of quartz for higher particles radius within concave surfaces, so promoting crack growth resulting in less shear stress required to break the grains when the laboratory fault get sheared. At temperatures of 400 °C, both healing magnitude and rate are higher in experiments performed on angular quartz. Following *Dove & Rimstidt (1994)* reasonings explained in section 4.1.1, I would have expected the opposite, since the higher solubility of quartz for smaller particles radius within convex surfaces (grain-to-grain contacts) promotes silica dissolution making more efficient pressure solution mechanisms and resulting in a better welding of grain-to-grain contacts for microquartz. This solubility-controlled mechanism does not occur in experiments performed at 400 °C, probably indicating different processes ongoing between the stressed surfaces and the film of fluid.

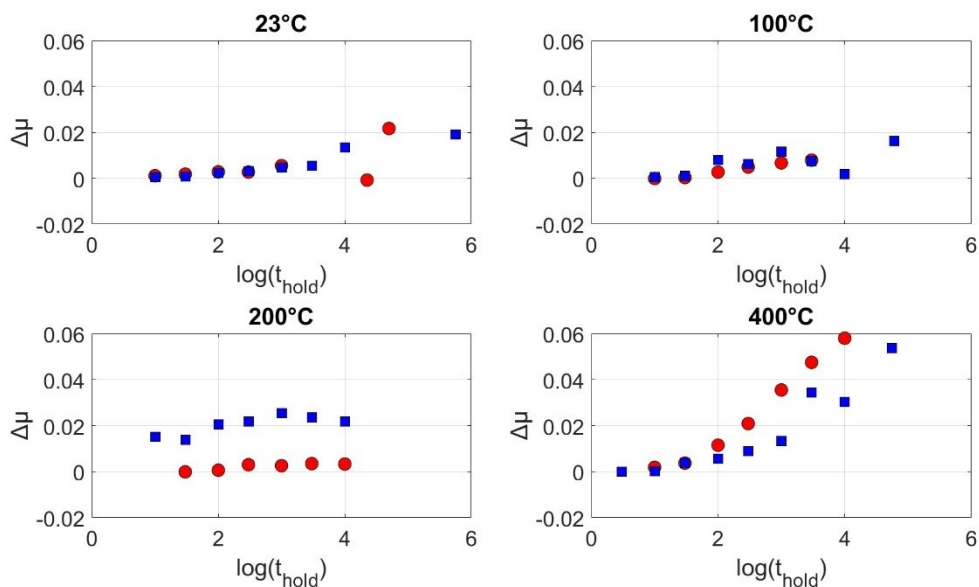


Figure 4.14. Both healing magnitude and rate appear to be superimposable at temperatures up to 100°C, confirming how grain size does not affect healing of the experimental fault under these P-T conditions. Different results came out at higher temperatures, indicating an influence of grain size on these parameters. Red dots: angular quartz; Blue dots: microquartz.

4.5 The role of shear strain on healing

By reviewing the literature, the mechanical influence of shear strain on strength and healing behavior of quartz gouges is poorly investigated. I performed sliding tests with very high horizontal displacement (hence shear strain in the gouge) and repeated SHS tests at different shear strain conditions. Plots showed in section 3.1 and measurements indicated in section 3.2, show that the second SHS test affected less the mechanical behavior of the gouge, in terms of variations of shear strength and compaction. Table 2 of section 3.3.3 shows the differences in the healing rate parameter (β) between the first and second SHS test showing that, except for the 100 °C test, healing is noticeably lower after the gouges experienced high shear strains. Figure 4.15 provides an example of how SHS series affected shear strength, compaction and healing of the sample during experiment R 374, performed on microquartz at 400 °C.

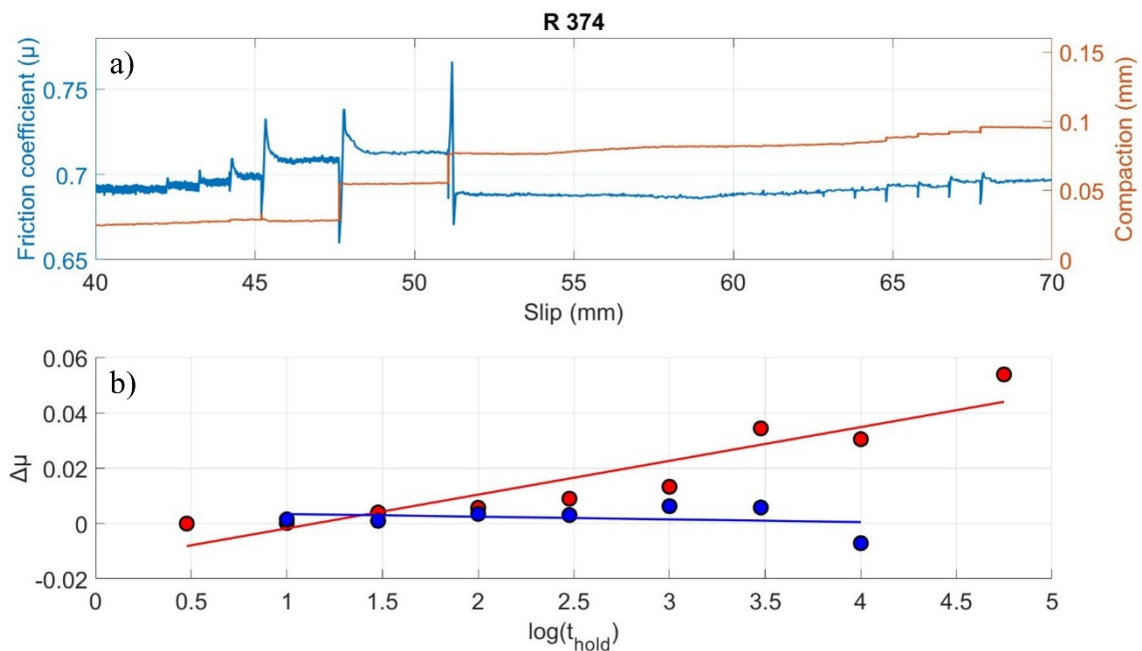


Figure 4.15. Experiment R 374 (400 °C). There are relevant differences in a) shear strength, compaction and b) healing measurements between the first and second SHS test performed. In b) red dots and line are relative to the first SHS test, while blue dots and line to the second one.

Between SHS tests 10 mm of slip occurred, during which shear strength remained constant while compaction slightly increased. As reported in section 3.2, during the first test the gouge gained 12% of shear strength with respect to the original steady state, and compacted for the 58% of its total compaction value. The second SHS test did not produce such results, gaining only 0.11% in shear strength and compacting only for the 19% with

respect to the total compaction during the experiment.

On the other hand, looking at data in section 3.3.3, where healing values are fitted through a regression line, first SHS test exhibited $\beta = 0.01228$, while for second SHS test was a negative value of $\beta = -9.6963 * 10^{-4}$. Second SHS series showed decreasing healing ($\Delta\mu$) with increasing $\log(t_{hold})$. In addition, negative healing value $\Delta\mu = -0.0073$ for $\log(t_{hold}) = 4$ was measured during the second SHS test. Negative healing values were also measured during second SHS test performed in experiment R 366 (23 °C): $\Delta\mu = -0.0008$ for $\log(t_{hold}) = 3.477$ and $\Delta\mu = 0.0012$ for $\log(t_{hold}) = 4$.

These data are indicating that for relatively high shear strain values the gouge is no longer strengthening with increasing hold time, thus not responding to the classical time-dependent “*Dieterich-type*” healing mechanism (*Dieterich, 1972; Marone, 1998*).

There are several possible interpretations of the mechanism to explain a “reduced healing” at high strains, which is remarkably unusual and not documented in the literature. Some possibilities are of technical nature: 1) the sampling rate could have been insufficient to record the re-shear peaks (assuming that peak static friction was attained and then evolved into dynamic friction faster than 1/10 s, given the 10 Hz sampling rate) or 2) the peak strength was masked by the deformation of the machine, which is very compliant with respect to other experimental apparatuses. However, both these technical explanations are rather unlikely, since they do not explain successful measurements of SHS peaks during earlier stages of the same experiments.

Most likely a physical mechanism exists to justify low healing at high strains. Since $\Delta\mu$ is a relative measurement of strength gain during interseismic periods, it only takes into account local changes in strength and not the whole history of deformation experienced by the gouge. With the exception of few tests, strain hardening and high healing are observed in the majority of tests (see figures in section 3.1 and Table 3 in section 3.3.3). Both strain hardening and healing increase the frictional strength of the experimental fault gouges. If this strength, caused by comminution to fine grain size, compaction and cementation (described above), is significantly higher than the current strength of the gouge during the second SHS sequence, the relative increase in strength measured as $\Delta\mu$ may be small. It is possible that the microstructures attained during previous slip history (e.g. the long holds of the first SHS sequence) were not completely destroyed by subsequent slip. Therefore the gouges were already partially compacted and cemented, leading to only a small incremental healing during subsequent hold times.

4.6 Comparison with previous studies

The comparison of the data reported above with those from previous reference papers on frictional healing of quartz gouge under dry and hydrothermal conditions (such as *Chester & Higgs (1992)*, *Marone (1998)*, *Nakatani & Scholz (2004)*, *Yasuhara et al. (2005)*, *Carpenter et al. (2016)*) is an important tool for relating the hypotheses proposed on which deformation mechanisms have operated at the different P-T conditions. These comparisons (from Figure 4.16 to Figure 4.19) show the consistency of results obtained in this thesis, since except for experiments performed at 100 °C, other data are quasi-superimposable to data coming from seminal papers such as those mentioned before, despite some differences in experimental apparatuses used to perform the experiments and experimental conditions (σ_n' , P_p).

Earlier studies from *Chester & Higgs (1992)* illustrated the temperature dependence of frictional healing ($\Delta\mu$). *Nakatani & Scholz (2004)* performed hydrothermal experiments on quartz gouges at temperatures up to 200 °C. They performed experiments both under dry and wet (liquid and vapor water) conditions, finding out that the enhanced healing measured in the presence of liquid water was not found in experiments performed under dry conditions or in the presence of vapor water. The only deformation mechanism that could provide such healing phenomena was a solution transfer mechanism. They performed an experiment with a preparatory hold time of 24 hours and measured the silica concentration in the pore fluid collected throughout the experiment (Figure 4.20). The data showed that the silica concentration reached levels up to 125 ppm, near the saturation concentration of quartz at 200 °C, and remained constant throughout the test. This suggested that silica saturation was achieved in the 24 hours preparatory hold. Therefore the healing occurred without net dissolution, constraining the healing mechanism to be a local solution transfer process, which locally redistributes solid mass within the grain aggregate (*Nakatani & Scholz, 2004*).

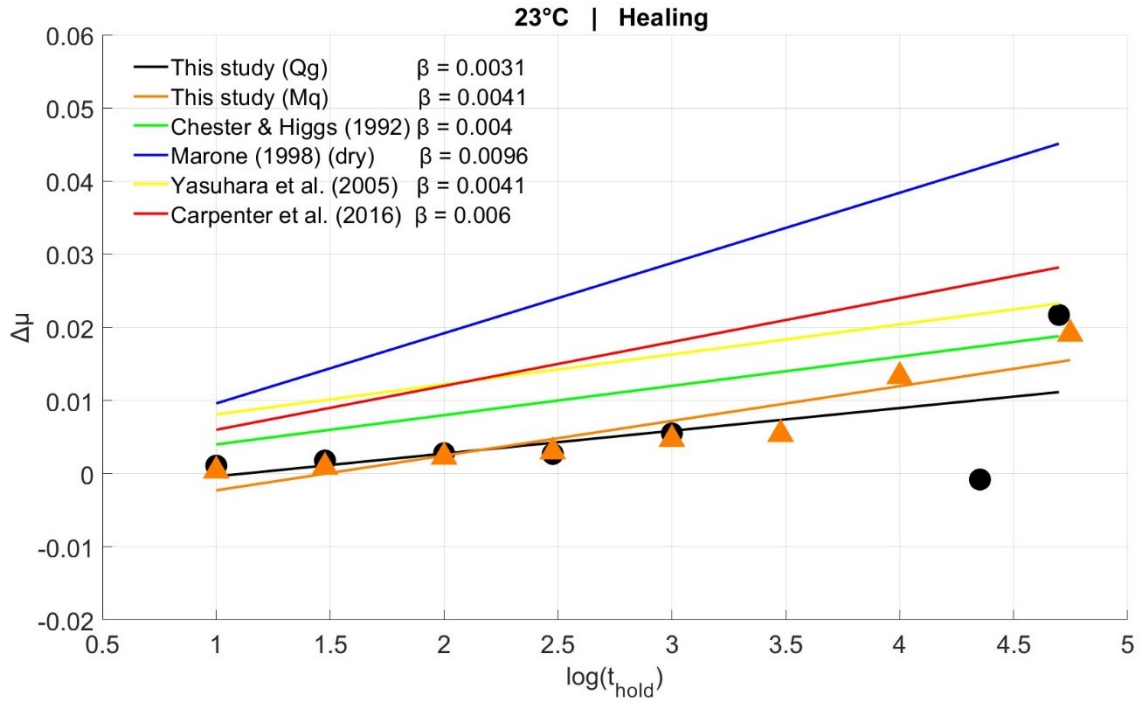


Figure 4.16. Comparison between healing rate parameters from several seminal studies and those of this thesis, at room temperature. All the papers cited refer to hydrothermal frictional experiments, except for Marone (1998).

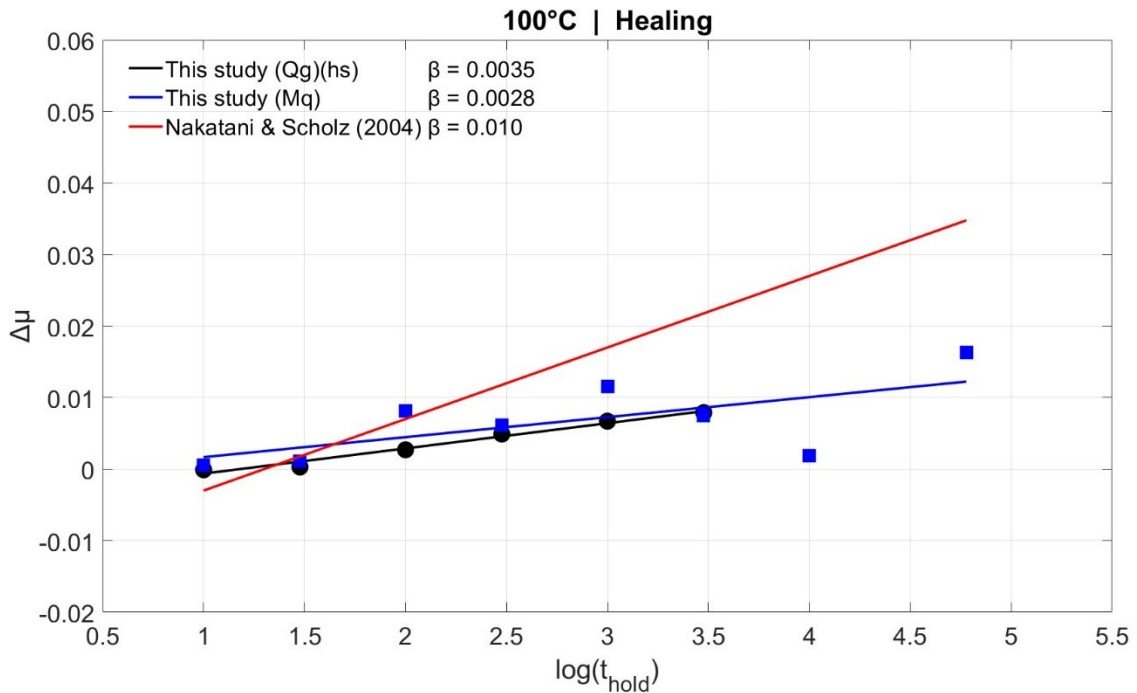


Figure 4.17. Comparison between healing rate parameter from Nakatani & Scholz (2004) and those of this thesis, for experiments performed at 100 °C.

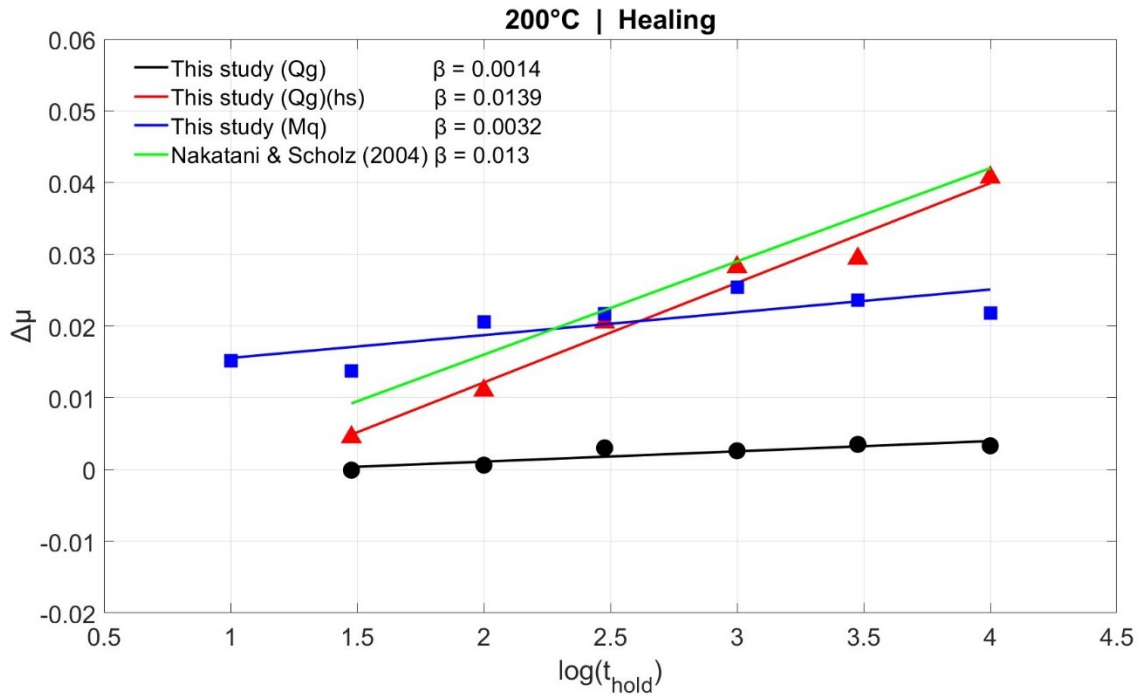


Figure 4.18. Comparison between healing rate parameter from Nakatani & Scholz (2004) and those of this thesis, for experiments performed at 200 °C.

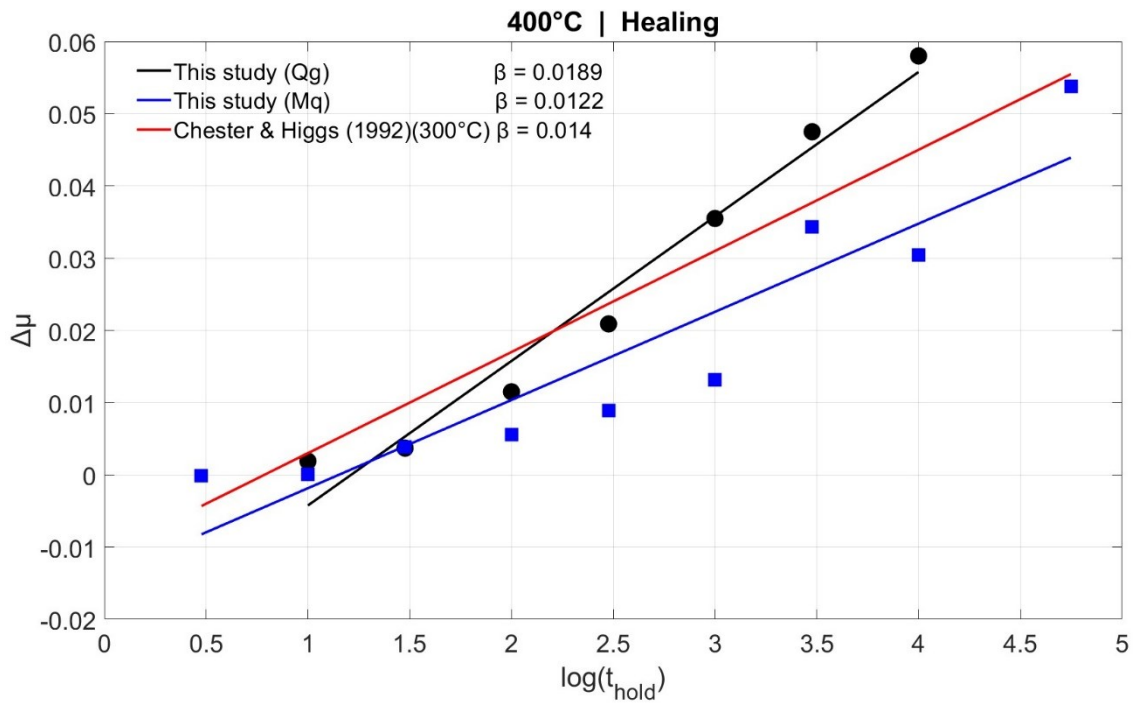


Figure 4.19. Comparison between healing rate parameter from Chester & Higgs (1992) and those of this thesis. The experiment of Chester & Higgs was performed at 300 °C.

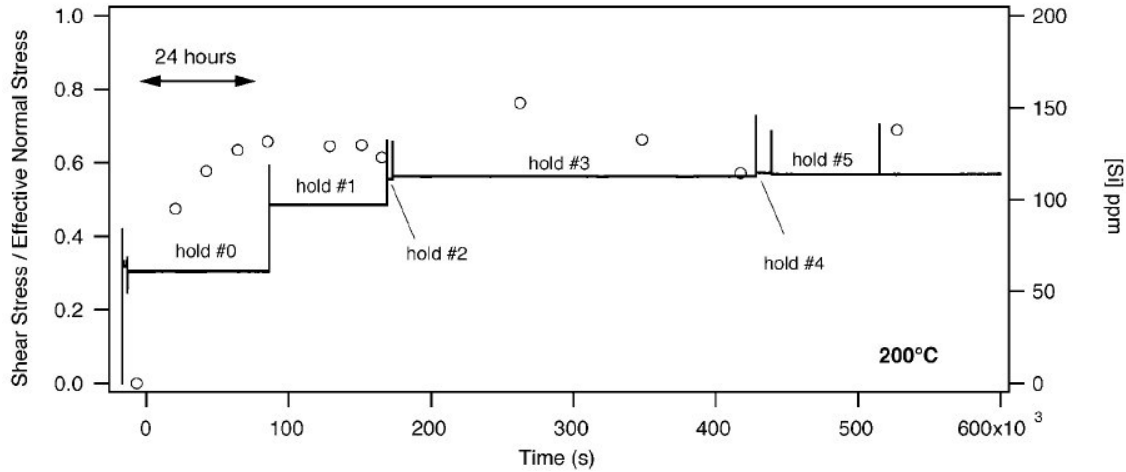


Figure 4.20. Diagram from Nakatani & Scholz (2004) showing the evolution of the silica concentration throughout the experiment. First, 24 hours preparatory hold raised the silica concentration up to ~ 125 ppm, near its saturation concentration. This was diagnostic to exclude solution transfer processes which don't involve redistribution of mass.

The main implication of results from Nakatani & Scholz (2004) is that a major role in controlling the healing mechanism could be played by the concentration of silica. Concentration of silica, as discussed in section 4.1.1, is controlled by its solubility, which is in turn controlled by temperature, pressure, grain size and equilibration time.

In the experiments of this thesis, equilibration time was kept constant around 2 hours, indicating that at high temperatures (400 °C) the concentration of silica (which is function of temperature) was likely near its saturation value. This suggests that the deformation mechanism that operated was pressure solution, probably accompanied by cementation. In my experiments, at lower temperatures the concentration of silica was probably below its saturation value, favoring dissolution of silica and pressure solution, but with a very minor role played by cementation. In addition, the compaction associated to hold times, the healing magnitude and healing rate values suggest pressure solution mechanism as the main operating deformation mechanism (Bos & Spiers, 2002; Niemeijer et al., 2002).

Healing ($\Delta\mu$) values measured in this thesis are noticeably lower than those measured in experiments from Nakatani & Scholz (2004). This could be related to the different experimental configuration (rotary-shear in this thesis and triaxial direct-shear for experiments of Nakatani & Scholz (2004)) and overall to the lower effective normal stress applied to the gouges in this thesis (Nakatani & Scholz (2004) used $\sigma_n' \sim 100$ MPa). In fact, making a comparison between experiment R 356 (200 °C, $\sigma_n' = 10$ MPa) and R 359 (200 °C, $\sigma_n' = 20$ MPa) it is clear that the higher the effective normal stress, the higher the magnitude and the rate of healing (Figure 4.21).

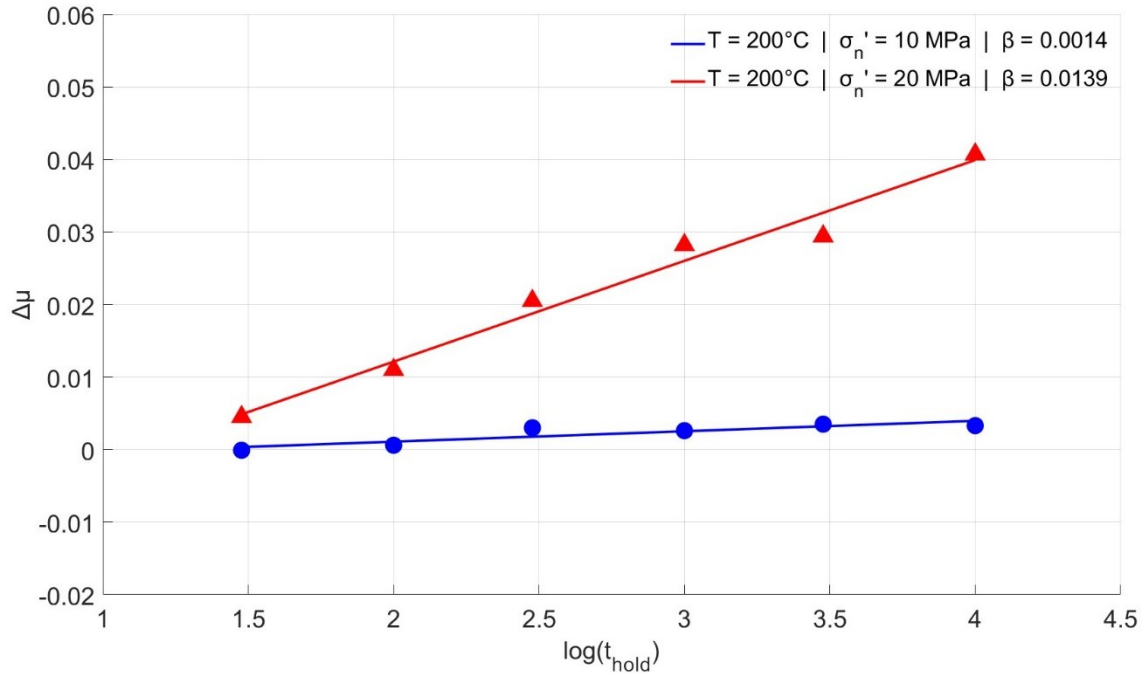


Figure 4.21. Influence of effective normal stress (σ'_n) on the magnitude and the rate of healing.

Another important feature of frictional experiments is the length of the initial run-in phase. Observing Figure 4.5 and 4.6, it is noticeable a long hardening and compacting stage, which in some cases reaches more than 30 mm of slip. The relevance of this initial phase could be connected to the mechanical analysis of the SHS tests: if the sample was still hardening and compacting when test started, the hold-slide events may be altered by earlier cataclastic and fracturing processes.

4.7 SHS anatomy

Chen et al. (2015) and *Carpenter et al. (2016)* defined the classical “*Dieterich-type*” healing mechanism (Figure 4.22) as follow. The sample, which is sheared at friction μ_{ss} , gets hold for a certain period t_{hold} and the shear strength relaxes nonlinearly due to sample creep and elastic relaxation of the testing machine and sample assembly (*Carpenter et al., 2016*). Upon reshear, elastic loading occurs, frictional sliding begins, and the friction coefficient reaches a peak value μ_{peak} before returning to steady state μ_{ss} .

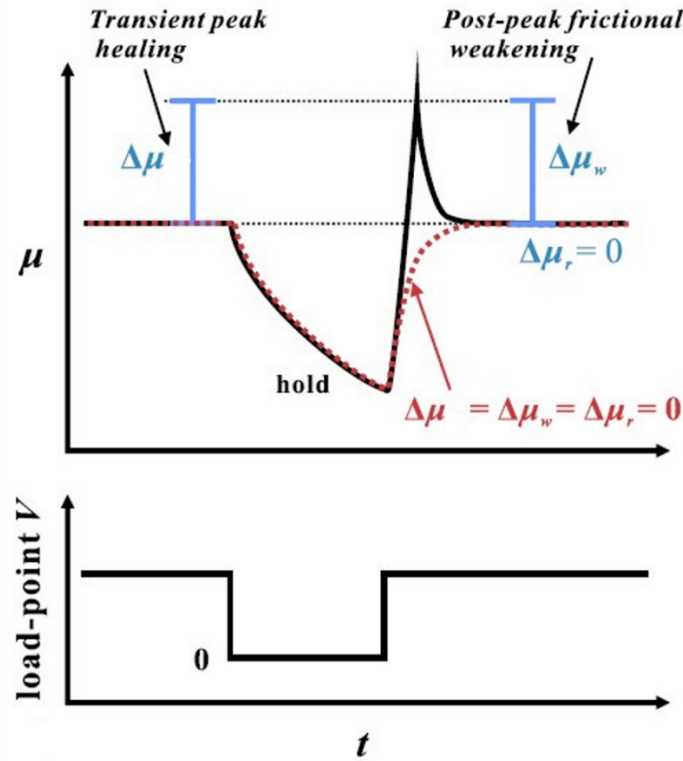


Figure 4.22. “Dieterich-type” healing mechanism. The red dotted line indicates a zero slip-weakening effect ($\Delta\mu_w=0$), previously reported mostly at high temperatures (e.g. Olsen et al., 1998). From Chen et al., 2015.

Classical “Dieterich-type” healing, as mentioned before, can be described by equation (4.12). However, post-peak frictional weakening ($\Delta\mu_w$) is taken into account in this form:

$$\Delta\mu = \Delta\mu_w = \beta \log(t_{hold}), \quad (4.14)$$

where $\Delta\mu$ is transient peak strength increase due to healing, measured in terms of the difference between the peak friction upon reshear and the pre-hold friction μ_{ss} . By contrast, $\Delta\mu_w$ is the post-peak weakening, measured as the difference between the peak and the post-hold steady state friction μ_{ss} . Lastly, $\Delta\mu_r = (\Delta\mu - \Delta\mu_w)$, is the residual, persistent strengthening, measured as the change in quasi steady state friction coefficient values observed after vs. before the hold period (Chen et al., 2015).

As already mentioned, Dieterich-type healing is defined by a linear relationship between $\Delta\mu$ and $\log(t_{hold})$, in addition to exhibiting zero persistent strengthening/weakening of the experimental fault (Dieterich, 1972,1978; Marone, 1998; Richardson & Marone, 1999). As can be seen by looking at Figure 4.23 and at zoomed figures in section 3.1, healing that operates in almost all the experiments performed show a non-zero persistent strengthening/weakening of the gouge, confirming a different underlying mechanism.

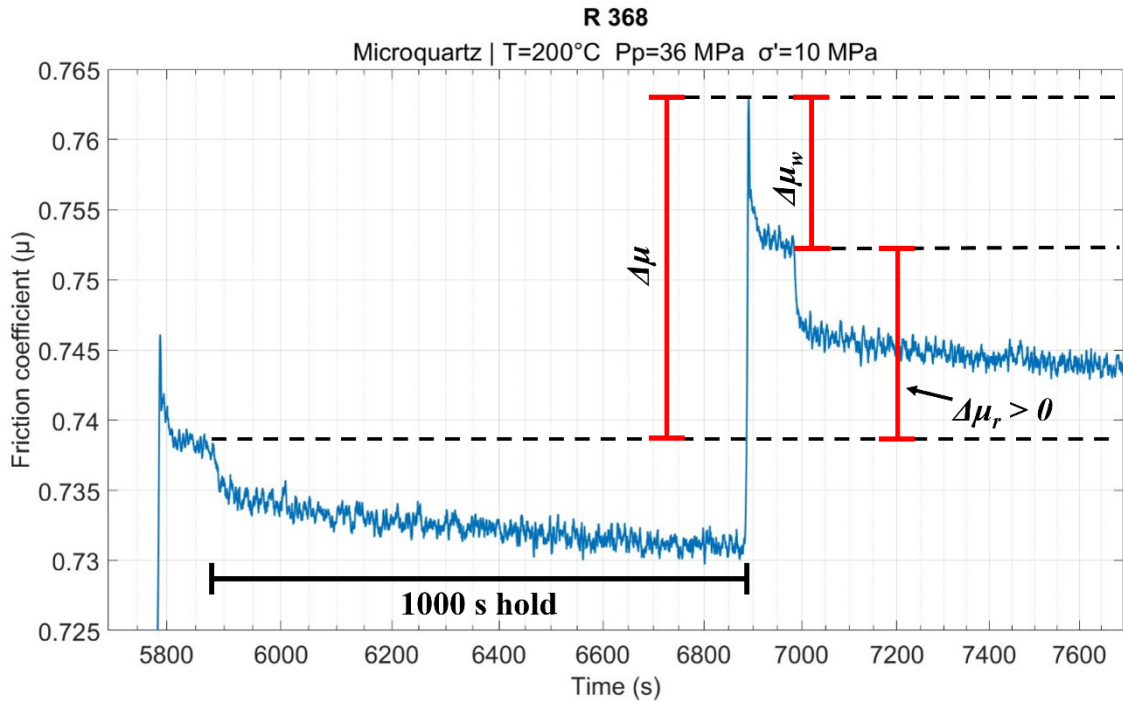


Figure 4.23. Non-Dieterich-type healing. $\Delta\mu_r > 0$ and post-peak $\mu_{ss} >$ pre-hold μ_{ss} .

The healing type reported in the experiment of this thesis is consistent with those reported by *Yasuhara et al. (2005)* and *Chen et al. (2016)* on their experiments under wet conditions and high temperatures. Intergranular pressure solution was inferred to produce enhanced “non-Dieterich-type” healing behavior by *Yasuhara et al. (2005)*, based on microstructural evidence, such as crack sealing and pore cementation. In all the experiments the samples accommodate the majority of compaction during holds. Since compaction rates during stationary contact (as reported in Figure 4.11) increase with increasing temperature and in the presence of fluid, this process is likely related to pressure solution, in accordance with results from *Bos & Spiers (2002)*. Figure 4.25 shows time-dependent compaction during hold period, followed by slight dilation upon reshear. This behavior is found in other hydrothermal frictional experiments performed on quartz as well as carbonates (*Bos & Spiers, 2002; Yasuhara et al., 2005; Chen et al., 2015; Carpenter et al., 2016*).

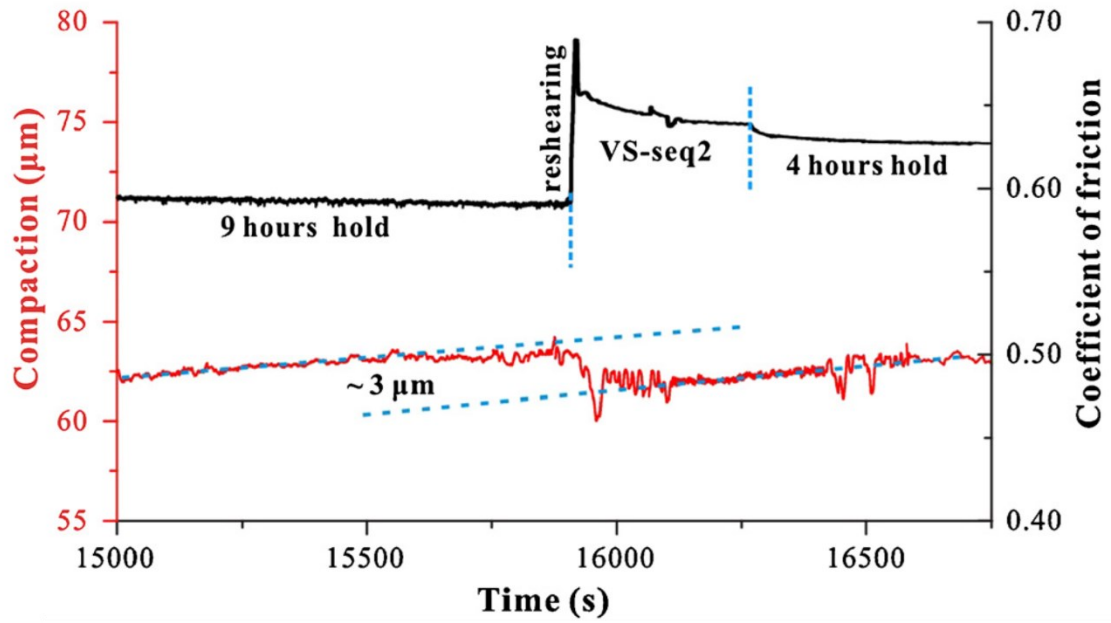


Figure 4.24. Hold-slide event in a hydrothermal experiment from Chen et al. (2015). Compaction increases during hold. While reshearing, the sample dilates recovering part of the compaction achieved.

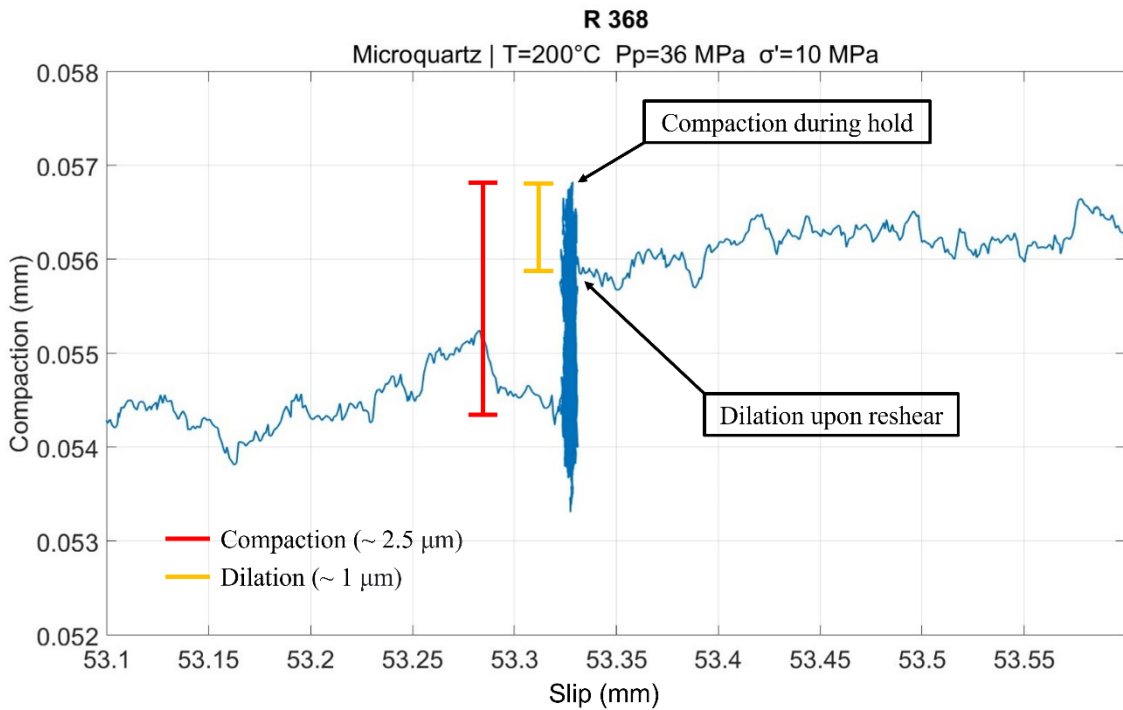


Figure 4.25. The sample exhibits a huge compaction during hold time. Upon reshear, dilation occurs but not all compaction is recovered.

4.8 Implications for crustal faults

The pressure and temperature conditions investigated in this thesis are likely to occur in shallow geothermal fields, considering a typical lithostatic pressure increasing of 25-30 MPa/km. Shallow faults, with quartz or feldspatic gouge between the stressed surfaces, can be percolated by hot fluids if the permeability and porosity are low enough. This could lead to the achievement of critical stress conditions by which failure occurs. Geothermal fields could be affected by extraction-induced earthquakes, triggered by poroelastic stresses associated with reservoir contraction, if the system is in critical stress conditions (*Segall & Fitzgerald, 1998*). Temperature perturbations within geothermal fields therefore can have a large influence of temperature on the shear strength of fault gouges, solution transfer mechanisms could be activated within fault surfaces. Experiments of this thesis indicate that at high temperature (above 200 °C) hot fluids may favor effective inelastic compaction and possibly cementation on timescales of tens to thousands of seconds (days). These processes favor the locking of fault patches and the alteration of the typical loading/unloading cycle. However, for this setting to occur a very low permeability is required, otherwise the system could be able to drain fluids away from overpressurized patches.

Another critical implication for crustal faults regards the lowered healing magnitude and rate for increased shear strain values. Results of this thesis indicate that frictional healing (i.e. increase in strength from dynamic to static conditions) is reduced in fault gouges that experienced high strains (several tens of mm of slow slip).

If a crustal fault exhibits pressure solution-related healing behavior, the effect of this mechanism will decrease with increasing displacement. Despite shear strain values were not quantified in this thesis, the occurrence of the shear strain effect on the mechanical behavior is pointed out in all the experiments, suggesting a shear strain-controlled healing mechanism, although this effect calls for further future investigation.

However, it is possible that these results may indicate that not only strengthening processes are active during interseismic periods but potentially also weakening processes (brittle creep?). Alternatively, this behavior indicates that healing measurements are strongly controlled by the slip history of the fault. High strain faults could reach, by slip hardening, a “maximum” strength (hence small or negligible $\Delta\mu$), or healing processes may migrate deformation into weaker parts of the rock mass away from healed zones. In the experiments of this thesis, gouges healed during the first SHS test may have been only

partially reworked by subsequent slip (i.e. deformation migrated elsewhere, possibly at the gouge-steel interface of the sample holder).

This could lead to strain weakening behavior: the fault progressively stores less elastic strain energy, resulting in an increased frequency of seismic events but a decrease in the elastic energy released with each event.

In nature, fault gouges are likely composed by mixtures of minerals surrounded by fluids of different chemistry, instead of a “simple” binary system, e.g. SiO_2 and H_2O . The presence of other minerals, even if in low weight %, completely alters the mechanical properties of quartz, changing the friction parameters. The widespread occurrence of phyllosilicate-bearing faults in several tectonic settings (*Tesei et al., 2012, Collettini et al., 2019*) plays a key role in controlling the shear strength of the majority of faults. As mentioned in section 1.1, phyllosilicates show a friction coefficient ranging from approximately 0.15 to 0.5, in function of their weight % within the mixture.

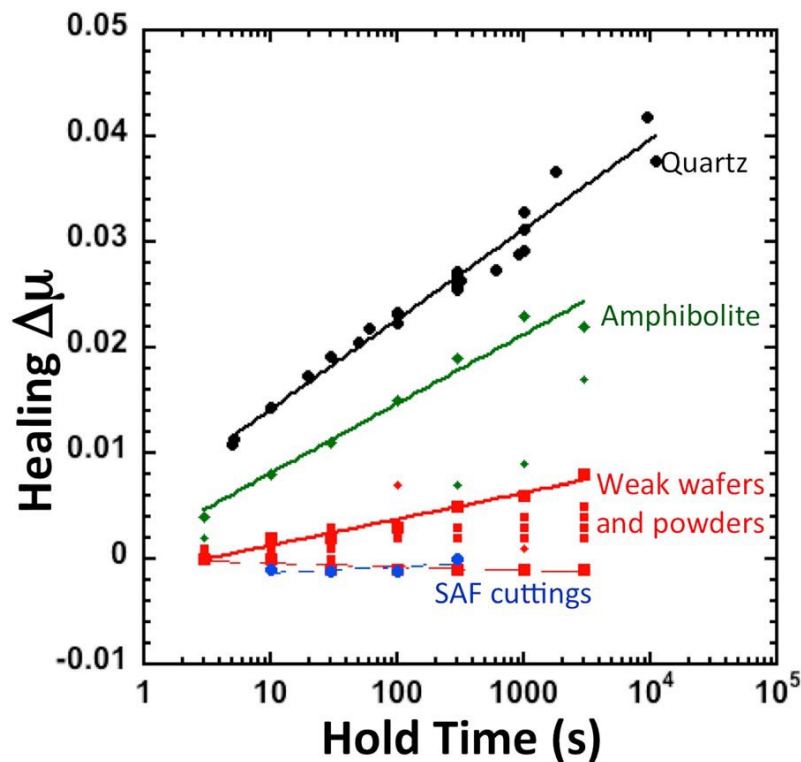


Figure 4.26. Healing ($\Delta\mu$) and healing rates (β) for angular quartz (Marone, 1998), amphibolite and clay-rich cuttings from the San Andreas Fault (Carpenter et al., 2011). Rock wafers and corresponding powders exhibit different mechanical properties, i.e. powdered materials resulted weaker than intact rocks. From Tesei et al. (2012).

Since the frictional strength of foliated fault rocks is determined by the weakest phase in the mixture (*Tesei et al., 2012*), the phyllosilicate content is critical to assess the behavior of the wall fault gouge. Figure 4.26 shows the comparison between healing and healing

rate of different rock types. In addition, looking at the figure it is possible to note the lower shear strength of powdered materials with respect to corresponding intact rocks. Carbonate-bearing faults, another widespread and common case in nature, exhibit healing rates remarkably higher than those measured for quartz in this thesis and available data in the literature. This confirms the heterogeneity of tectonic faults by different perspectives, mechanical one included. Figure 4.27 illustrates the comparison between healing rate values for quartz-feldspatic rocks and carbonates based on experiments from *Marone (1998)* and *Carpenter et al. (2014)* respectively.

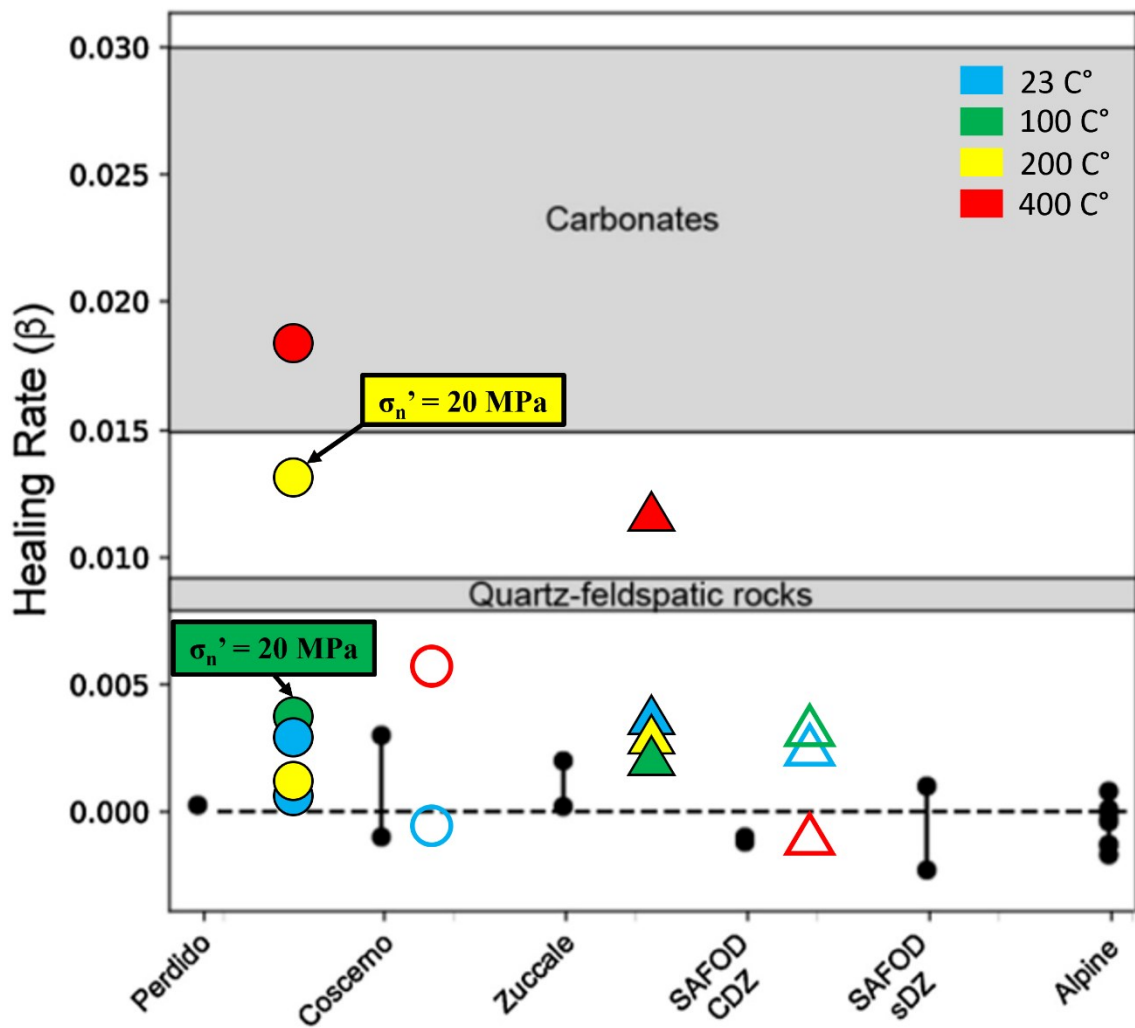


Figure 4.27. Schematic diagram showing healing rate data for quartz-feldspatic rocks (*Marone, 1998*) and carbonates (*Carpenter et al., 2014*), modified from *Collettini et al. (2019)*. Healing rate values relative to the experiments of this thesis are plotted in the diagram. Filled circles and triangles represent data from the first SHS test performed in experiments on F110 heterometric angular quartz and microquartz respectively. Empty markers refer to the second SHS test.

Conclusions

In this thesis the seismic cycle of a quartz gouge under hydrothermal conditions has been investigated from a primarily mechanical perspective. Great attention was given to the healing parameters ($\Delta\mu$, β), which are directly linked to the recurrence of earthquakes in nature and to the elastic strain energy that crustal faults are able to store during interseismic periods. I performed 10 frictional experiments on quartz gouges under hydrothermal conditions, varying temperature (T), effective normal stress (σ_n), pore fluid pressure (P_p) and grain size. For each experiment, one or two Slide-Hold-Slide tests were performed. The collected data and the subsequent analysis suggest that:

- The temperature does not particularly influence the steady state friction μ_{ss} , while it affects more evidently the compaction of the samples during the first 20-30 mm of slip. This could be explained by temperature-dependent inelastic processes that act during slip.

On the other hand, the temperature has a large effect on the healing measured. Fit curves of healing data show that $\Delta\mu$ increases linearly as the t_{hold} increases, for experiments performed up to 200 °C, in the form:

$$\Delta\mu = \beta \log(t_{hold}).$$

For experiments performed at 400 °C, however, a quadratic relationship exists between $\Delta\mu$ and t_{hold} , in the form:

$$\Delta\mu = [\log(t_{hold})]^2.$$

The same quadratic relationship describes the dependence of the friction drop after a transient peak strength increase ($\Delta\mu_{drop}$) on t_{hold} . Therefore, with increasing temperature, healing becomes increasingly non-linear and non-Dieterich-type, consistently with the literature.

- The effective normal stress (σ_n) affects healing measurements: despite further studies are necessary to confirm the reproducibility to what found, the comparison between two experiments at 200 °C, on quartz gouges with the same grain size, but with two different effective normal stresses (20 MPa vs. 10 MPa) highlighted that the healing rate (β) measured for the experiment with higher effective stress is approximately 90% greater than the healing rate of the experiment with lower effective stress.
- The grain size affects the steady state shear strength μ_{ss} , which generally increases as grain size decreases. This is probably due to the higher S/V ratio of smaller particles that makes it more difficult to comminute and grind the grains. Furthermore, the steady state is reached much earlier in experiments performed on microquartz (<5 μm) compared to experiments performed on angular quartz (<125 μm). In addition, a decrease in grain size could favor solution transfer processes, by increasing the solubility of quartz at stressed grain-to-grain contacts. To this phenomenon could be added the closure of cracks due to the decrease in solubility of silica within concave surfaces. Further investigations are necessary.
- The shear strain has a large mechanical impact on the gouges in terms of healing and compaction. An example is the case of experiment R 374, performed on microquartz at 400 °C. 10 mm of slip between the two SHS tests are sufficient to step from a strengthening of 12% during the first test to a strengthening of 0.11% during the second test, compared to the steady state shear strength μ_{ss} before each test. These data are accompanied by a compaction of 58% during the first SHS series and 19% during the second (compared to total compaction).

The comparison between healing and compaction measurements in this thesis and those from several seminal papers suggests that the operating deformation mechanism is pressure solution. The non-linear dependence of healing rate (β) on the logarithm of hold time and the compaction during holds, the change in steady state friction around holds all suggest the hypothesis of pressure solution as the main deformation mechanism.

Probably, secondary deformation mechanisms operate together with pressure solution: cementation of saturated silica within less stressed surfaces could be responsible for further welding of grains, while low temperature plasticity at 400 °C likely enhances

compaction.

Major critical implications for crustal faults regard the temperature effect on the healing rate. Crustal faults within geothermal fields are commonly surrounded by hot fluids. If the permeability is low enough solution transfer processes may occur, altering the seismic cycle.

FUTURE DEVELOPMENTS

Further developments of this thesis are certainly represented by a microstructural /microanalytical analysis of the experimentally deformed samples. This could confirm the hypotheses formulated regarding the deformation mechanisms occurred in quartz gouges. Other frictional experiments under hydrothermal conditions may be necessary to better investigate the control of solubility on the dissolution and subsequent reprecipitation of quartz, the relationship between the healing measured at low and high effective normal stress, and healing behavior depending on the physical state of the water (liquid, vapor and supercritical conditions).

References

- Beeler, N. M., Tullis, T. E., Weeks, J. D. (1994), The roles of time and displacement in the evolution effect in rock friction, *Geophys. Res. Lett.*, 21(18), 1987–1990, doi:10.1029/94GL01599.
- Biegel, R. L., Wang, W., Scholz, C. H., Boitnott, G. N. (1992), Micromechanics of Rock Friction 1. Effects of Surface Roughness on Initial Friction and Slip Hardening in Westerly Granite, *J. Geophys. Res.*, 97(B6), 8951-8964, doi: 10.1029/92JB00042.
- Bos, B., & Spiers, C. J. (2002), Fluid-assisted healing processes in gouge-bearing faults: Insights from experiments on a rock analogue system, *Pure Appl. Geophys.*, 159, 2537–2566, doi:10.1007/s00024-002-8747-2.
- Bowden, F. P., & Tabor, D. (1950). *The friction and lubrication of solids* (Vol. 1). Oxford university press.
- Bowden, F. P., & Tabor, D. (1964). *The friction and lubrication of solids part II*. *Phys. Today*, 17, 72.
- Brace, W. F., & Byerlee, J. D. (1966). Stick-slip as a mechanism for earthquakes. *Science*, 153(3739), 990-992.
- Brace, W. F., & Kohlstedt, D. L. (1980). Limits on lithospheric stress imposed by laboratory experiments. *Journal of Geophysical Research: Solid Earth*, 85(B11), 6248-6252.
- Carpenter, B. M., Ikari, M. J., Marone, C. (2016), Laboratory observations of time-dependent frictional strengthening and stress relaxation in natural and synthetic fault gouges, *J. Geophys. Res., Solid Earth* 121, 1183–1201. <https://doi.org/10.1002/2015JB012136>.
- Chakoumakos, Bryan C., and G. V. Gibbs. "Theoretical molecular orbital study of silanol-water interactions." *The Journal of Physical Chemistry* 90.6 (1986): 996-998.
- Chen, J., Verberne, B. A., Spiers, C. J. (2015), Interseismic re-strengthening and stabilization of carbonate faults by “non-Dieterich” healing under hydrothermal conditions, *Earth and Planet. Science Lett.*, 423(2015), 1-12, <http://dx.doi.org/10.1016/j.epsl.2015.03.044>.
- Chester, F. M., & Higgs, N. G. (1992). Multimechanism friction constitutive model for ultrafine quartz gouge at hypocentral conditions. *Journal of Geophysical Research: Solid Earth*, 97(B2), 1859-1870.
- Collettini, C., Tesei, T., Scuderi, M. M., Carpenter, B. M., Viti, C. (2019), Beyond Byerlee friction, weak faults and implications for slip behavior, *Earth and Planet. Science Lett.*, 519(2019), 245-263, <https://doi.org/10.1016/j.epsl.2019.05.011>.
- Di Toro, G., Han, R., Hirose, T., De Paola, N., Nielsen, S., Mizoguchi, K., Ferri, F.,

- Cocco, M., Shimamoto, T. (2011), Fault lubrication during earthquakes, *Nature*, 471 (7339), 494–498, doi:10.1038/nature09838.
- Dieterich, J. H. (1972), Time-dependent friction in rocks, *J. Geophys. Res.*, 77, 3690–3697, doi:10.1029/JB077i020p03690.
- Dieterich, J. H. (1978). Time-dependent friction and the mechanics of stick-slip. *Rock friction and earthquake prediction*, 790-806.
- Dieterich, J. H., and B. D. Kilgore (1994), Direct observation of frictional contacts: New Insights for state-dependent properties, *Pure Appl. Geophys.*, 143, 283–302, doi:10.1007/BF00874332.
- Dove, P. M., & Rimstidt, J. D. (1994). Silica-water interactions. *Reviews in Mineralogy and Geochemistry*, 29(1), 259-308.
- Fagereng, Å., & Sibson, R. H. (2010). Mélange rheology and seismic style. *Geology*, 38(8), 751-754.
- Fournier, R. O., & Potter II, R. W. (1982). An equation correlating the solubility of quartz in water from 25 to 900 C at pressures up to 10,000 bars. *Geochimica et Cosmochimica Acta*, 46(10), 1969-1973.
- Freiman, S. W. (1984). Effects of chemical environments on slow crack growth in glasses and ceramics. *Journal of Geophysical Research: Solid Earth*, 89(B6), 4072-4076.
- Giger, S. B., Tenthorey, E., Cox, S. F., Fitz Gerald, J. D. (2007), Permeability evolution in quartz fault gouges under hydrothermal conditions, *J. Geophys. Res.*, 112, B07202, doi:10.1029/2006JB004828.
- Grigull, S. (2011), Insights into the Rheology of Rocks under Brittle-Ductile Deformation Conditions from an Exhumed Shear Array in the Southern Alps, New Zealand, PhD Thesis, Victoria University of Wellington.
- Helmons, R. I. J., & Miedema, S. A. (2013). Cutting through hard rock-like materials, a review of the process. *WODCON XX*.
- Hirose, T., Shimamoto, T. (2005), Growth of molten zone as a mechanism of slip weakening of simulated faults in gabbro during frictional melting, *J. Geophys. Res.*, 110, B05202, doi:10.1029/2004JB003207.
- Ikari, M. J., Marone, C., Saffer, D. M. (2009b), Frictional and hydrologic properties of clay-rich fault gouge, *J. Geophys. Res.*, 114, B05409, doi:10.1029/2008JB006089.
- Karner, S. L., Marone, C., Evans, B. (1997), Laboratory study of fault healing and lithification in simulated fault gouge under hydrothermal conditions, *Tectonophysics*, 277, 41–55.
- Kronenberg, A. K. (1994). Silica, Physical Behavior, Geochemistry and Materials Applications. *Rev. Mineralogy*, 29, 123-176.

- Lockner, D. A., Moore, D. E., & Reches, Z. E. (1992, June). Microcrack interaction leading to shear fracture. In ARMA US Rock Mechanics/Geomechanics Symposium (pp. ARMA-92). ARMA.
- Ma, S., Shimamoto, T., Yao, L., Togo, T., Kitajima, H. (2014), A rotary-shear low to high-velocity friction apparatus in Beijing to study rock friction at plate to seismic slip rates, *Earthq. Sci.*, 27(5):469-497, doi: 10.1007/s11589-014-0097-5.
- Marone, C. (1997), On the rate of frictional healing and the constitutive law for time- and slip-dependent friction, *Int. J. Rock Mech. & Min. Sci.*, 34:3-4, Paper No. 187.
- Marone, C. (1998a), Laboratory-derived friction laws and their application to seismic faulting, *Annu. Rev. Earth Planet. Sci.* 26, 643–696, <http://dx.doi.org/10.1146/annurev.-earth.26.1.643>.
- Moore, D. E., & Lockner, D. A. (2004). Crystallographic controls on the frictional behavior of dry and water-saturated sheet structure minerals. *Journal of Geophysical Research: Solid Earth*, 109(B3).
- Naito, K., Tsutsumi, T., Yamada, T., & Yashiro, K. (2016). Processing method utilizing stick-slip phenomenon for forming periodic micro/nano-structure. *Journal of Materials Processing Technology*, 238, 267-273.
- Nakatani, M., Scholz, C. H. (2004), Frictional healing of quartz gouge under hydrothermal conditions: 1. Experimental evidence for solution transfer healing mechanism, *J. Geophys. Res.*, 109, B07201, doi:10.1029/2001JB001522.
- Nakatani, M., Scholz, C. H. (2004), Frictional healing of quartz gouge under hydrothermal conditions: 2. Quantitative interpretation with a physical model, *J. Geophys. Res.*, 109, B07202, doi:10.1029/2003JB002938.
- Niemeijer, A. R., Spiers, C. J., Bos, B. (2002), Compaction creep of quartz sand at 400-600°C: experimental evidence for dissolution-controlled pressure solution, *Earth and Planetary Science Letters*, 195 (2002), 261-275.
- Niemeijer, A. R., Spiers, C. J. (2007), A microphysical model for strong velocity weakening in phyllosilicate-bearing fault gouges, *J. Geophys. Res.*, 112, B10405, <http://dx.doi.org/10.1029/2007JB005008>.
- Niemeijer, A. R., Marone, C., Elsworth, D. (2008), Healing of simulated fault gouges aided by pressure solution: results from rock analogue experiments, *J. Geophys. Res.*, 113, B04204, <http://dx.doi.org/10.1029/2007JB005376>.
- Paterson, M. S., & Wong, T. F. (2005). *Experimental rock deformation: the brittle field* (Vol. 348). Berlin: Springer.
- Ranjith, K., Rice, J. R. (1999), Stability of quasi-static slip in a single degree of freedom elastic system with rate and state dependent friction, *Journal of the Mechanics and Physics of Solids*, 47 (1999), 1207-1218.

- Rice, J. R. (2006), Heating and weakening of faults during earthquake slip, *J. Geophys. Res.*, 111, B05311, doi:10.1029/2005JB004006.
- Richardson, E., Marone, C. (1999), Effects of normal stress vibrations on frictional healing, *J. Geophys. Res.*, 104 (B12), 28859–28878, doi:10.1029/1999JB900320.
- Rudnytskyj, A. (2018). Simulations of contact mechanics and wear of linearly reciprocating block-on-flat sliding test.
- Ruina, A. (1983), Slip instability and state variable friction laws, *J. Geophys. Res.*, 88 (B12), 10359–10370.
- Rutter, E. H. (1976), The kinetics of rock deformation by pressure solution, *Philosophical Transactions of the Royal Society of London*, A 283, 203–219.
- Rutter, E.H. (1983), Pressure solution in nature, theory and experiment, *J. geol. Soc. London*. Vol. 150, 725-740.
- Scholz, C. H. (1988), The brittle-plastic transition and the depth of seismic faulting, *Geologische Rundschau*, 77/1, 319-328.
- Scholz, C. H. (1988), The critical slip distance for seismic faulting, *Nature*, Vol. 336, 22/29.
- Scholz, C. H. (2019). *The mechanics of earthquakes and faulting*. Cambridge university press.
- Scott, D. R., Marone, C. J., Sammis, C. G. (1994), The apparent friction of granular fault gouge in sheared layers, *J. Geophys. Res.*, 99 (B4), 7231-7246.
- Segall, P., Fitzgerald, S. D. (1998), A note on induced stress changes in hydrocarbon and geothermal reservoirs, *Tectonophysics*, 289, 117-128.
- Segall, P., & Rice, J. R. (1995). Dilatancy, compaction, and slip instability of a fluid-infiltrated fault. *Journal of Geophysical Research: Solid Earth*, 100(B11), 22155-22171.
- Shepherd, R. G. (1989). Correlations of permeability and grain size. *Groundwater*, 27(5), 633-638.
- Sibson, R. H. (1977), Fault rocks and fault mechanics, *J. geol. Soc. London*, v. 133, 191-213, doi:10.1144/gsjgs.133.3.0191.
- Sibson, R. H., Scott, J. (1998), Stress/fault controls on the containment and release of overpressured fluids: Examples from gold-quartz vein systems in Juneau, Alaska; Victoria, Australia and Otago, New Zealand, *Ore Geology Reviews*, 13, 293-306.
- Sibson, R. H. (2002), *Geology of the Crustal Earthquake Source*, *International Geophysics Series*, 81(A), 455-474.
- Sibson, R. H. (2003). Thickness of the seismic slip zone. *Bulletin of the Seismological Society of America*, 93(3), 1169-1178.

Tesei, T., C. Collettini, B. M. Carpenter, C. Viti, and C. Marone (2012), Frictional strength and healing behavior of phyllosilicate-rich faults, *J. Geophys. Res.*, 117, B09402, doi:10.1029/2012JB009204.

Tesei, T., Collettini, C., Barchi, M. R., Carpenter, B. M., Di Stefano, G. (2014), Heterogeneous strength and fault zone complexity of carbonate-bearing thrusts with possible implications for seismicity, *Earth and Planetary Science Letters*, 408, 307-318. <http://dx.doi.org/10.1016/j.epsl.2014.10.021>.

Townend, J., & Zoback, M. D. (2000). How faulting keeps the crust strong. *Geology*, 28(5), 399-402.

Walther, J. V., & Helgeson, H. C. (1977). Calculation of the thermodynamic properties of aqueous silica and the solubility of quartz and its polymorphs at high pressures and temperatures. *Am. J. Sci.:(United States)*, 277(10).

Wang, W., & Scholz, C. H. (1995). Micromechanics of rock friction: 3. Quantitative modeling of base friction. *Journal of Geophysical Research: Solid Earth*, 100(B3), 4243-4247.

Williams, R. T., & Fagereng, Å. (2022), The role of quartz cementation in the seismic cycle: A critical review, *Reviews of Geophysics*, 60, e2021RG000768, <https://doi.org/10.1029/2021RG000768>

Yasuhara, H., C. Marone, and D. Elsworth (2005), Fault zone restrengthening and frictional healing: The role of pressure solution, *J. Geophys. Res.*, 110, B06310, doi:10.1029/2004JB003327.

Zhang, S., & Tullis, T. E. (1998). The effect of fault slip on permeability and permeability anisotropy in quartz gouge. *Tectonophysics*, 295(1-2), 41-52.